An Improved Representative Interactive Flamelet Model Accounting for Evaporation Effect in Reaction Space (RIF-ER)

by

SeungHwan Keum

A dissertation submitted in partial fulfillment
of the requirements for the degree of
Doctor of Philosophy
(Mechanical Engineering)
in The University of Michigan
2009

Doctoral Committee:

Professor Dionissios N. Assanis, Co-Chair
Assistant Professor Hong G. Im, Co-Chair
Professor James F. Driscoll
Assistant Research Scientist Aristotelis Babajimopoulos

to my wife Hyejin,

my brother Seungwoo and his family,

and my parents

Acknowledgments

I wish to thank to my advisors, Professor Assanis and Professor Im. Needless to say, this work would have not existed if it were not for their supports and invaluable advices. I have been privileged to do my research with them, and I'd like to express my deepest appreciation.

I would like to thank Professor Driscoll for serving im my committee and providing guidance and encouragement in difficult times.

I would like to thank Dr. Babajimopoulos for serving my committee. Dr. Babajimopoulos has been more than a good mentor to me. I truly appreciate his friendship, guidance and support for the last four years.

I thank Dr. Lavioe and Professor Jung for their support and guidance.

I thank all members of the W. E. Lay Automotive Laboratory for being good friends and great mentors. Dr. Hong, Dr. Chryssakis and Dr. Grover were those who introduced me into the KIVA3v modeling work. I am especially thankful to Jason Martz, Chaitanya Sampara for being very good friends.

I thank my wife Hyejin, and my family back in Korea.

Table of Contents

List of Tables

Table

List of Figures

Figure

List of Appendices

Appendix

Abstract

Recently, applications of spray combustion in internal combustion engines (ICE) are being expanded from conventional to gasoline direct injection engines. Moreover, stratification using spray is further considered as a controlled autoignition (CAI) measure in Homogeneous Charge Compression Ignition (HCCI) engines.

A well validated spray combustion model can provide a good modeling tool which can facilitate understanding of spray combustion physics. In this research, a spray combustion model is proposed to model low temperature combustion in internal combustion engines. The proposed model is based on the Representative Interactive Flamelet (RIF) model of Peters (2000). In addition to the original RIF model, the effect of spray and vaporization of droplets in the reaction space were considered to be included in the governing equations as source terms. The effect of such source terms were examined in the reaction space in idealized control volumes, where the effect of vaporization is assumed as gaseous fuel addition with known rate of addition. It was found that the effect of spray may not be negligible when fuel addition occurs over a reaction space with chemical reaction. The proposed model was validated by comparing pressure and fuel concentration against experimental data from the rapid compression machine experiment of Akiyama *et al.* (1998) and the diesel engine experiment of Hong *et al.* (2008). Predictions showed good agreement with the experimental observations. Comparison between numerical models, one with spray source terms and the other without them has been carried out to examine the effect of spray source terms on spatial fuel distributions and overall pressure histories.

The proposed model has been implemented in KIVA3v. The proposed model is applied

to investigate the effect of stratification under PPCI operating condition using direct injection. An experimental study on the effect of stratification on combustion and emission has been numerically reproduced. The numerical results showed good qualitative agreement with the measured engine performance and emission trend against the experimental data. Detailed analysis of the in–cylinder combustion is also provided.

Chapter 1
Motivation and Objectives

1.1 Introduction

Recent developments in internal combustion engines (ICE) have been driven by two major driving forces. One is the limited fossil fuel reserve, which motivates researchers to develop engines with better fuel economy. The other is health and environmental awareness on emissions. Every year, more stringent emission regulations are legislated to nitrogen oxides, particulate matter, carbon dioxide and unburned hydrocarbons, and in future greenhouse gases.

Research has been carried out to meet both of engine efficiency and emissions requirements. As part of these effects, investigation on different combustion modes has been actively carried out, in order to better meet the demands of future engines. Well-known examples are Premixed Charge Compression Ignition (PCI) combustion mode (Blakeman *et al.* , 2003; Takeda & Keiichi, 1996; Lechner *et al.* , 2005) and the Homogeneous Charge Compression Ignition (HCCI) combustion mode (Najt & Foster, 1983). The PCI combustion mode aims to improve Compression Ignition (CI) combustion to reduce emissions by taking advantage of low temperature combustion by high EGR (Exhaust Gas Recirculation) and less stratification by longer ignition delay.

The HCCI combustion mode is a hybrid combustion mode of CI and Spark Ignition (SI) combustion. Fuel and oxidizer are mixed before entering the engine cylinder (similar to SI engines) to be auto-ignited by compression (similar to CI engines). Both HCCI and

PCI share the same principles of homogeneous mixture and low temperature combustion, while the degree of homogeneity is the major difference. HCCI has shown successful results in reducing NOx and particulate emissions. However, HCCI suffers from combustion instability and misfire at low load conditions where the in-cylinder mixture becomes too lean to autoignite. Various controlled autoignition (CAI) methods have been suggested to obtain combustion stability at low load conditions. The most well-known strategies are Variable Valve Actuation (VVA) and stratification using direct injection. In the VVA, a large amount of residual gas is introduced into the combustion chamber to obtain high enough temperature for the mixture to ignite. On the other hand, the stratification strategy utilizes direct injection to create locally rich enough mixture for autoignition. A combustion mode utilizing the stratification strategy is commonly referred to as Partially Premixed Charge Compression Ignition, or PPCI combustion mode to be distinguished from HCCI.

It can be summarized that novel combustion methods aim to provide more homogeneous charge which will be consumed by low temperature combustion. At the same time, some level of stratification is required to maintain combustion stability, which is accomplished by direct injection and spray combustion. Numerical simulation techniques have the potential to provide valuable information for spray combustion. Even though there has been progress in experimental measurement methods, computational fluid dynamics can still provide valuable insight where experimental measurements are not yet possible.

Computational fluid dynamics simulations for turbulent combustion modeling have been improved over the last few decades. The main problem in turbulent combustion modeling has been how to determine an average reaction rate in fluctuating turbulent flow. This problem is commonly referred as *turbulence-chemistry closure problem*, and development and improvement of turbulent combustion model has been carried out to achieve better model for the turbulence chemistry closure based on physics.

One of the simplest models, a characteristic time combustion model (CTC) was suggested by Patterson *et al.* (1994). In the CTC model, the rate of change in species is

modeled by considering the turbulent time scale. This model has been extensively used in diesel combustion literature due to low computational cost and reasonably accurate result. However, the CTC model utilizes empirical constants to determine the turbulent time scale, which should be calibrated for each case the model is applied. On the other extreme of the CTC model exists the Direct Numerical Simulation (DNS) (Poinsot & Trouve, 1994), which demands very high computational cost for the sake of numerical accuracy. Due to its extremely high computational cost, the DNS model has so far been applied only to fundamental studies.

Among other turbulent combustion models is an Eddy Dissipation Concept (EDC) model suggested by Magnussen & Hjertager (1976), which is based on the Eddy Breakup (EBU) model of Spalding (1976). Both the EBU and EDC models focus on a rate-limiting process for turbulence-chemistry closure modeling. In a non-premixed combustion, reactants are supplied by fuel-air(oxidizer) mixing, and the rate of reaction is expected to be controlled by the deficient species, either being an oxidizer or fuel. The EDC model has been successfully implemented and applied to diesel engine combustion (Hong *et al.* , 2008; Wooldridge *et al.* , 2005).

A conserved scalar variable approach was suggested by Klimenko & Bilger (1999) for turbulent non-premixed combustion modeling. In the conserved scalar variable approach, only transport equations related to the *conserved scalar* are solved in the physical space regardless of the number of participating species. Then, the local value of passive scalar variables such as species mass fraction, temperature, and pressure are determined by a function of conserved scalar variable. Two different models have evolved from the conserved scalar variable approach. One is the flamelet model of Peters (2000), and the other is the Conditional Moment Closure (CMC) model of Klimenko & Bilger (1999). Even though both models are based on the same conserved scalar variable, and the final governing equations share some similarities, the approach taken by each model is quite different.

In the CMC model, a transport equation for reactive scalars $\vec{\Phi}$ conditioned at Z, or

$\langle\vec{\Phi}|Z\rangle$ is derived to be solved, where $\vec{\Phi}$ is not only a function of Z but also as a function of t and $\vec{x}$. Meanwhile, the flamelet model assumes dependency of $\vec{\Phi}$ on only Z. Another difference between the two models is that Φ is treated as an instantaneous fluctuating quantity in the flamelet model. Both models are under active research and have been applied to the internal combustion engine modeling. The CMC model has higher computational cost due to added transport equation of $\vec{\Phi}(Z;\vec{x},t)$. It is a common practice to use separate grids for $\vec{\Phi}$ and Z on the same physical domain in the CMC model to reduce the computational cost. However, such separate meshes in an internal combustion engine may not be feasible considering complex geometries of modern internal combustion engines. Meanwhile, the flamelet model benefit from the usual computation mesh along with one-dimensional reaction space, which leads to significantly reduced computational cost while maintaining good numerical results.

In this study, the flamelet approach of Peters (2000) will be used to investigate spray combustion. As a well-validated turbulent combustion model, the flamelet model has been applied to a wide variety of combustion devices from gas turbines (Riesmeier *et al.* , 2004) to diesel engines (Hasse & Peters, 2005; Hergart *et al.* , 2005; Hergart & Peters, 2002). A major application of the flamelet approach is the DICI engines, where the flamelet model has shown good agreement against experimental results under various engine operating conditions. Most recently, the flamelet model is even applied to model low temperature combustion Weber *et al.* (2007). At the same time, effort has been made to improve the flamelet model by considering the effects of spray in governing equations, which were not considered in the original formulation of the model Pitsch & Peters (1998).

The effects of direct injection on the flamelet approach are twofold. Typically, direct injection is applied by a high-pressure injector to facilitate droplet breakup and mixing of fuel and oxidizer. With a high-pressure common rail system with an injection pressure of 100MPa, the injection velocity may reach up to 500m/sec. Droplets injected by such high velocity interact with ambient air to result in an increase in in-cylinder turbulence, which

will be reflected by an increase in the variance of Z, $\widetilde{Z''^2}$. Such increase in $\widetilde{Z''^2}$ will increase the scalar dissipation rate, which is a key variable controlling turbulent combustion. Also, the shape of local PDF will be changed. The effect of direct injection on the variance variable has been carried out by a number of researchers (Demoulin & Borghi, 2002; Ge & Gutheil, 2008; Hollmann & Gutheil, 1998, 1996). Recently, the modified variance equation has been incorporated into CFD solver to model an internal combustion engine (Kim *et al.* , 2004).

The other effect of direct injection is the increased local fuel mass concentration. In the flamelet approach, the reaction is treated separately in the reaction space from the reaction space. Only the amount of mixing between the fuel and the oxidizer is considered in the physical space. Actual fuel species informations are stored and updated in the reaction space considering turbulent combustion. Previous applications of flamelet approach in spray combustion have considered the increase in fuel mass in the physical space, which is reflected by increase local Z values. However, the effect of vaporization in the reaction space has not been considered in most of previous studies. When reaction progress in the reaction space is yet not significant, consideration of Z increase may be sufficient to consider the increase in fuel in the reaction space. However, when fuel is added over partially reacted mixture, the effect of vaporization should be considered in the reaction space. Otherwise, the species information in the physical space will be updated by a reaction space which solely considers turbulent reaction but not the effect of vaporization.

1.2 Objective

A few of available turbulent combustion models have been discussed in the previous section. Among discussed models, the flamelet approach was found to provide detailed chemistry capability with reasonable amount of computing resource. Other models will require higher computing resource as the number of species is increased. The flamelet approach

also provides a turbulence-chemistry closure model based on solid physics in turbulent non-premixed combustion. At the same time, this approach has room for improvement to be applied to model spray combustion.

The objective of this study is to propose an improved spray combustion model suited for low temperature combustion with direct fuel injection. The improved model should properly address the turbulence closure issue with appropriate consideration on the effect of spray on reaction. For the purpose of turbulence closure, the current model will be based on the flamelet approach of Peters (2000).

A brief description of flamelet model will be given in Chapter 2. The proposed model will be presented in Chapter 3. The model will consider the effect of vaporization on the reaction space. For the purpose, the governing equations will be rederived to identify source terms in the reaction equation reflecting the effect of droplet vaporization. The effect of such terms will be examined by idealized control volumes which represent different location in a spray and different reaction/vaporization history. Implementation of the suggested model and consideration on computational efficiency will be discussed in Chapter 3. Validation studies of the proposed model will be carried out in Chapter 4. Finally, the model will be applied to a low temperature combustion engine to investigate the effect of injection timing on engine performance in Chapter 5.

Chapter 2

Introduction to the Laminar Flamelet Approach

2.1 Introduction

In this chapter, a brief introduction to the laminar flamelet approach will be given following Peters (2000). Peters (1984) suggested a turbulent combustion model based on the flamelet concept. In the flamelet approach, the flow field and species compositions are described by a single variable, which is a conserved scalar (Z) following Bilger's approach. The actual species information is determined by a library, where each species mass fraction information is available as a function of Z, $Y_i(Z)$. This library, which is often referred to as *flamelet Library*, is determined by solving the reaction in one dimensional space in the direction of the largest gradient in species mass fraction.

The most well-known and widely used model in turbulent combustion models using the flamelet approach is the *RIF* model, which stands for the Representative Interactive Flamelet Model. The flamelet approach has a few variations based on the RIF concept. A brief description of a flamelet approach and its variants will be described in this section.

2.1.1 Steady Laminar Flamelet Model: SLFM

In the original formulation of the non-premixed flamelet approach by Peters (1984), a steady non-premixed combustion was investigated . Since it is a steady system, only a

single $Y_i(Z)$ information, or *flamelet library*, was required. The suggested model was referred to as a Steady Laminar Flamelet Model, or SLFM in short. Each flamelet library was determined by different scalar dissipation rate χ. Later, SLFM was expanded to unsteady combustion by providing $Y_i(\chi, Z)$ for χ at given time in unsteady flow. However, in an unsteady flow, the transient value of χ determines the reaction history. As a result, unsteady combustion modeling based on steady flamelet libraries may not be appropriate to provide reasonable results. This model was soon superseded by the well-know *RIF* model which considers transient evolution of the flamelet library. In SLFM, libraries of $Y_i(\chi, Z)$ are prepared for possible range of χ a priori. When applied to unsteady combustion, these libraries are used for corresponding χ value in transient flow field.

2.1.2 Representative Interactive Flamelet Model: RIF

Unlike SLFM, the Representative Interactive Flamelet (RIF) model by Pitsch *et al.* (1998) builds a dynamic library of $Y_i(\chi, Z)$ at each time step during unsteady combustion in the reaction space. At each time step, a nominal scalar dissipation rate for the entire combustion region is determined based on volumetric average over stoichiometry (conditional average). The flamelet equation is solved considering the unsteady scalar dissipation rate to properly consider the effect of turbulence on combustion. Details of the RIF modeling approach will be covered in Section 2.2. The shortcoming of the RIF model is the use of single nominal, or conditionally averaged, scalar dissipation rate for the whole combustion region.

2.1.3 Eulerian Particle Flamelet Model: EPFM

An Eulerian Particle Flamelet Model (EPFM) was suggested by Barths *et al.* (1998, 2000). In EPFM, more than one dynamically updated flamelet libraries are utilized. Each flamelet governs computational cells for a certain range of the scalar dissipation rate. Each flamelet is tracked in the physical space by an Eulerian particle tracker.

2.1.4 Other variants of the RIF model

Variants of the RIF models have been developed to apply the flamelet approach to different configurations than gaseous non-premixed combustion. The enthalpy–based flamelet model (Hergart, 2001; Hergart *et al.* , 2005) was developed specifically consider the HCCI engine where direction of the largest gradient of reactive scalars occur in the direction of a conserved variable based on enthalpy rather than conserved scalar. A two-mixture fraction variable model was suggested by Hasse & Peters (2005) to consider a split injection case in diesel engines.

2.2 Laminar Flamelet Approach

In this chapter, the classic formulation of the RIF model in gaseous non-premixed combustion will be presented following Peters (2000).

The flamelet approach is based on two major principles. One is the use of the conserved scalar, and the other is the separation of turbulent combustion consideration from the physical space. In the flow field, a conserved scalar variable Z is used to account for the turbulent flow field and turbulent mixing between the fuel and the oxidizer streams. Meanwhile, the actual information on reactive species is stored in the reaction space against different levels of mixing, or different values of Z as a function of Z, as $Y_i(Z)$. This functional dependency of Y_i on Z is commonly referred to as *flamelet* or *flamelet library*, which may occasionally arouse unnecessary confusion with the term "*flamelet*" mentioned in usual combustion literature. In this research, *reaction space* will be used to refer the $Y_i(Z)$ relationship since it is essentially a one-dimensional space where such relationship is considered for turbulent combustion.

The three-dimensional physical space is then mapped to the one-dimensional reaction space. A coordinate for the one-dimensional reaction space is chosen as a direction in the physical space where the most significant change, or the largest gradient, in the reaction

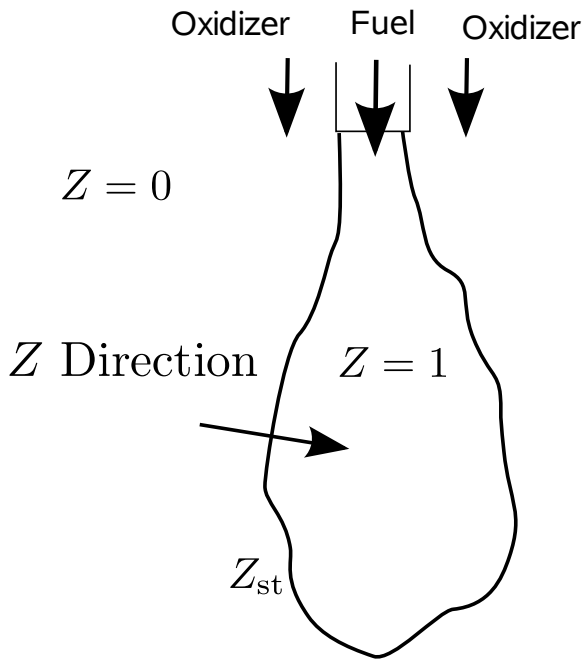

Figure 2.1: Direction of the largest gradient in reactive species in a non-premixed combustion

space is observed.

In this regard, the flamelet model may be considered as an eigenvalue problem (Cheng, 2007). The principal axis, or eigenvector, of the physical space takes a direction where the gradient of Y_i is the largest. This eigenvector is assumed to be the Z direction based on physical reasoning in a non-premixed combustion system. Then, only the change in Y_i against Z is considered for reaction consideration.

By taking such direction, it is possible to create a one-dimensional space for considering reactions. In a non-premixed combustion system, the largest gradient in reactive scalars occurs in the direction across the flame as shown in a schematic diagram, Figure 2.1.

Such treatment results in two spaces to be considered. The first one is the *Physical Space* where temporal and spatial change in the conserved scalar is determined. The other

is a *Reaction Space* where the species information is stored as a function of the conserved scalar, which is again updated at each time step to account for temporal change under turbulent combustion.

In both spaces, the governing equations are derived from species transport equations in the physical space. Derivation of the governing equations in the physical space and the reaction space will be discussed following the approach of Peters (2000) in subsequent sections.

2.2.1 Physical Space: Conserved Scalar Variable

In a non-premixed combustion system, the fuel and the oxidizer are separately introduced into the combustion chamber where they are mixed. The level of mixing between the fuel and the oxidizer can be described by introducing a conserved scalar variable. The conserved scalar variable, as its name implies, does not vary due to chemical reaction. This characteristic enables to use a conserved scalar to track mixing between fuel and oxidizer regardless of reaction.

A few different definitions of the conserved scalar are available. In this study, the conserved scalar variable based on carbon mass fraction will be used.

$$m_j = \sum_{i=1}^{n} \frac{a_{ij} W_j}{W_i} m_j \tag{2.1}$$

W_i represents the molecular weight of an element, while a_{ij} represents the number of elements j in species i. The mass fraction of j^{th} element is then

$$Z_j = \sum_{i=1}^{n} \frac{a_{ij} W_j}{W_i} m_j Y_i \tag{2.2}$$

One may derive a conservation equation for the elemental mass fraction (2.4) from mass

conservation equation (2.3).

$$\rho\frac{\partial Y_i}{\partial t}+\rho\mathbf{u}\cdot\nabla Y_i=-\nabla\cdot\mathbf{j}_i+w_i \tag{2.3}$$

$$\rho\frac{\partial Z_j}{\partial t}+\rho\mathbf{u}\cdot\nabla Z_j=-\nabla\cdot\left(\sum_{i=1}^{n}\frac{a_{ij}W_j}{W_i}m_j\right) \tag{2.4}$$

$$\sum_{i=1}^{n}a_{ij}W_i v_i k=0 \tag{2.5}$$

It can be noticed that the chemistry source term does not appear in (2.4), since the element mass is conserved regardless of reaction. Further generalization based on constant diffusivity for all species leads to the conservation equation (2.6) for conserved scalar variable Z.

$$\rho\frac{\partial Z}{\partial t}+\rho\mathbf{u}\cdot\nabla Z=\nabla\cdot(\rho D_Z\nabla Z) \tag{2.6}$$

In this study, a mass fraction-based scalar variable will be denoted as Z, defined by the normalized carbon element mass fraction.

$$Z=\sum_{i=1}^{N}Y_i\frac{\zeta_i}{\zeta_{\text{Fuel}}} \tag{2.7}$$

$$\zeta_i=\frac{\text{Carbon element mass in species i}}{\text{MW}_i} \tag{2.8}$$

A relationship between Z and the equivalence ratio can be determined as follows.

$$\Phi=\frac{1-Z_{\text{st}}}{Z_{\text{st}}}\frac{Z}{1-Z} \tag{2.9}$$

, where Z_{st} denotes the Z value at stoichiometry. It should be noted that the equivalence

ratio Φ in (2.9) denotes an equivalence ratio based on pure mixing. This is similar to the *big* Φ used in the KIVA-Multi-Zone model of Babajimopoulos *et al.* (2005).

2.2.2 Reaction Space: Flamelet Equation

In a non-premixed combustion systems, reaction is generally confined within the thin reaction zone or the flame near stoichiometric mixture. Also within the flame, the direction of highest gradient is always across the flame, as shown in Figure 2.1. It is being assumed that no significant change occurs in a tangential direction to the flame.

Since the most significant gradient in species occurs across the flame, a coordinate transformation from the Cartesian coordinate system to a coordinate system attached to the flame surface is suggested. The new coordinate system has one axis normal to the flame surface (Z_1), while two other axis (Z_2,Z_3) are tangential to the flame surface. The direction of Z coincides with the flame surface normal direction Z_1. A transformation rule from the three-dimensional space to one-dimensional space with its coordinate direction of Z is suggested as follows, assuming negligible change of species in Z_2 and Z_3 directions.

$$\frac{\partial}{\partial t} = \frac{\partial Z}{\partial t}\frac{\partial}{\partial Z} + \frac{\partial}{\partial \tau} \tag{2.10}$$

$$\frac{\partial}{\partial x_i} = \frac{\partial Z}{\partial x_i}\frac{\partial}{\partial Z} + \frac{\partial}{\partial Z_i} \qquad i = 2,3 \tag{2.11}$$

$$\frac{\partial}{\partial x_1} = \frac{\partial Z}{\partial x_1}\frac{\partial}{\partial Z} \tag{2.12}$$

Applying the above coordinate transformation to (2.3) leads to:

$$\rho\frac{\partial Y_i}{\tau} + \frac{\partial Y_i}{\partial Z}\left[\rho\frac{\partial Z}{\partial t} + \rho\mathbf{u}\cdot\nabla Z - \nabla\cdot(\rho D_i \nabla Z)\right] = \rho\frac{\chi}{2}\frac{Le_Z}{Le_i}\frac{\partial^2 Y_i}{\partial Z^2} + \omega_i \tag{2.13}$$

The terms in the bracket on LHS represent convective terms in the reaction space, which

can be simplified by using Z transport equation (2.6).

$$\rho\frac{\partial Y_i}{\tau}+\frac{\partial Y_i}{\partial Z}\left[\nabla\cdot(\rho D_Z\nabla Z)-\nabla\cdot(\rho D_i\nabla Z)\right]=\rho\frac{\chi}{2}\frac{Le_Z}{Le_i}\frac{\partial^2 Y_i}{\partial Z^2}+\omega_i \tag{2.14}$$

The terms in the bracket represents the effect of differential diffusion. The differential diffusion is transformed by the following relationship.

$$\frac{\partial Z}{\partial x_i}\frac{\partial}{\partial Z}\left(\rho D_i\frac{\partial Z}{\partial x_i}\right)=\frac{1}{4D_Z}\chi\frac{\partial\rho D}{\partial Z}+\frac{1}{4}\frac{\partial}{\partial Z}\left(\frac{D_i}{D_Z}\rho\chi\right) \tag{2.15}$$

In the above equation, the instantaneous scalar dissipation rate defined as

$$\chi=2D|\nabla Z|^2 \tag{2.16}$$

was introduced. The scalar dissipation rate reflects the effect of turbulence on the reaction space.

Using this relationship in (2.13) yields:

$$\rho\frac{\partial Y_i}{\tau}+\frac{\partial Y_i}{\partial Z}\left[\frac{1}{4D_Z}\chi\frac{\partial}{\partial Z}\left(\rho(D_Z-D_i)\right)+\frac{1}{4}\frac{\partial}{\partial Z}\left(\frac{(D_Z-D_i)}{D_Z}\rho\chi\right)\right]=\rho\frac{\chi}{2}\frac{Le_Z}{Le_i}\frac{\partial^2 Y_i}{\partial Z^2}+\omega_i \tag{2.17}$$

This equation is further simplified by assuming $Le_Z=1$ and constant Lewis number for all species to obtain the final flamelet equation.

$$\rho\frac{\partial Y_i}{\partial t}=\frac{\rho}{Le}\frac{\chi}{2}\frac{\partial^2 Y_i}{\partial Z^2}+\omega_i \tag{2.18}$$

In a laminar non-premixed configuration, (2.18) and (2.6) along with the scalar dissipation rate are enough to describe the physical space and the reaction space. In the reaction space, $Y_i(Z)$ information is stored against Z values.

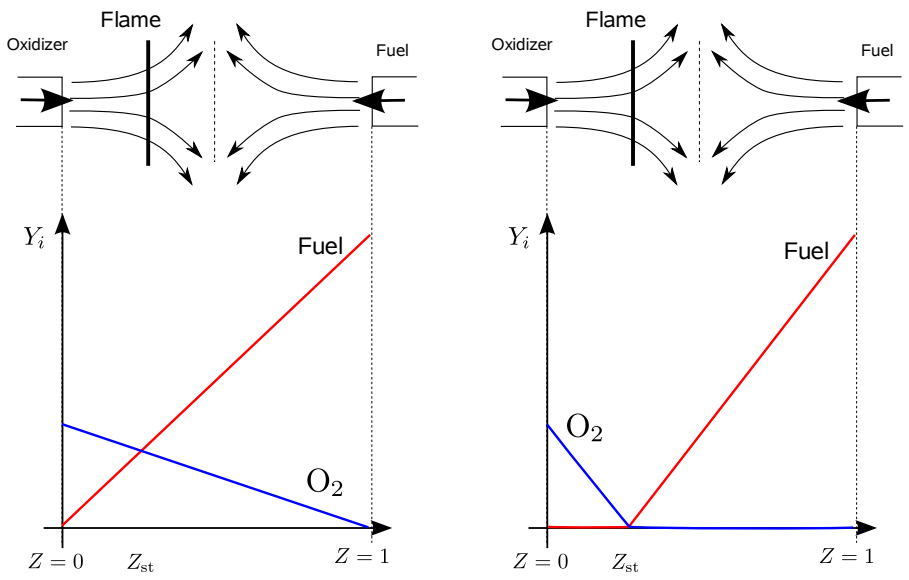

(a) Mixing Limit (b) Equilibrium Limit

Figure 2.2: Reaction space showing Mixing Limit and Equilibrium Limit

2.2.3 Reaction Space: $Y_i(Z)$

It is often convenient to understand if Y_i profiles are plotted in a functional form of Z. Illustrative figures of the reaction space are shown in Figure 2.2. For simplicity, only the fuel species and the oxidizer profiles are shown.

By definition, Z ranges from 0 to 1, and so are Y_f. The oxidizer stream has Z value of zero, while the fuel stream has Z value of unity. This may be better understood if a counterflow flame configuration is assumed, as shown at the top of Figure 2.2. When the oxidizer and the fuel stream are purely mixing without any reaction, $Y_f(Z)$ takes a linear profile, representing pure mixing between two streams. This is shown in blue line in Figure 2.2(a). The mixing limit constitutes an active upper limit for the each species considered in the reaction space. On the other extreme is the equilibrium limit, which resembles the well-known Burke-Schmann limit in a counterflow flame. If fuel and oxidizer are reacting with infinitely fast reaction, Y_i at each Z reaches equilibrium which is plotted in red in Figure 2.2(b). The equilibrium limit constitutes the lower limit of Y_i at each Z value.

Flamelet and Reaction Space

The word *flamelet* has been used to imply different meanings. In general, flamelet refers to the thin reaction zone in a non-premixed combustion system. In other words, it refers to a region in the physical space, where reaction occurs with negligible effect of turbulence.

On the other hand, *flamelet* has also been used to describe the reaction space, or $Y_i(t,Z)$ relationships. During the development of the flamelet approach, SLFM of Peters (1984) used libraries of $Y_i(t,Z)$, where each library was constructed by solving the reaction equation under different configurations (mainly different T and χ). The term *flamelet libraries* was used to describe such libraries, which are essentially $Y_i(t,Z)$ relationships in the reaction space. This was often referred to as simply *flamelet*.

In this study, to avoid unnecessary confusion, the term *flamelet* is used to explicitly describe the *thin reaction zone in the physical space* as mentioned before. Corresponding Z space, as shown in Figure 2.2, will be referred to as *Reaction Space*, or *Reduced Dimensional Space*. The relationship $Y_i(t,Z)$ is defined in the reaction space.

2.3 Laminar Flamelet Model for Non-premixed Turbulent Combustion

2.3.1 Describing the Turbulent Reacting Flow: Favre Averaging

Turbulence is characterized by fluctuating quantities. Stochastic description is used to describe these fluctuating quantities based on statistical description. Mean values of fluctuating quantities, or random variables, are of interest in the turbulent flow modeling.

A density-weighted average, known as Favre average, is used in this research to describe the mean and fluctuation of a random variable.

$$u(t,\vec{x}) = \tilde{u}(t,\vec{x}) + u''(t,\vec{x}) \tag{2.19}$$

$$\overline{\rho u''} = 0 \tag{2.20}$$

The Favre averaging is very useful in modeling a compressible turbulent flow. In this research, the Favre averaging will be used to derive the governing equations with mean quantities. In stochastic description of turbulence, a mean value of a fluctuating quantity is usually described by statistical mean, or expectation, of instantaneous value.

$$\tilde{u} = \int_{-\infty}^{+\infty} P(u)\mathrm{d}u \tag{2.21}$$

Knowledge of the governing PDF is required to determine the statistical mean. In the flamelet model, a presumed PDF function is assumed, which will be discussed in detail in Section 2.3.5.

2.3.2 Conserved Scalar Variable

As mentioned in Section 2.2.1, the turbulent flow field is described by the conserved scalar variable. The conserved scalar variable is split into mean ($\tilde{Z}$) and fluctuation ($\widetilde{Z''^2}$). Governing equations for $\tilde{Z}$ and $\widetilde{Z''^2}$ are derived as follows from the Z transport equation (2.18).

$$\bar{\rho}\frac{\partial \tilde{Z}}{\partial t} + \bar{\rho}\tilde{\vec{u}}\cdot\nabla\tilde{Z} = \nabla\cdot(\bar{\rho}D\nabla\tilde{Z}) \tag{2.22}$$

$$\bar{\rho}\frac{\partial \widetilde{Z''^2}}{t} + \bar{\rho}\tilde{\vec{u}}\cdot\nabla\widetilde{Z''^2} = -\nabla\cdot\left(\bar{\rho}D\widetilde{Z''^2}\right) + 2\bar{\rho}D_t(\nabla\tilde{Z})^2 - \bar{\rho}\tilde{\chi} \tag{2.23}$$

Molecular diffusion terms are assumed to be negligible. A Gradient transport assumption is taken in (2.22) and (2.23). These two equations are used to describe the turbulent flow field.

2.3.3 Turbulent Combustion: Turbulence-Chemistry Closure in the Flamelet Model

One of the major problems in turbulent reacting flow modeling is the evaluation of the mean chemical source term. Favre averaging of a reactive scalar leads to the following equation.

$$\bar{\rho}\frac{\partial Y_i}{\partial t} + \bar{\rho}\tilde{\vec{u}} \cdot \nabla \tilde{Y}_i = \nabla \cdot (\rho D \nabla \tilde{Y}_i) + \bar{\omega}_i \tag{2.24}$$

where $\bar{\omega}_i$ represents a mean chemical reaction source term and $\bar{\dot{\rho}}_i$ represents spray source term. Chemical reaction is a nonlinear function of pressure, temperature and related reactive scalars which may not be determined by simple averaging. Most of turbulent combustion models described in Section 1.1 are aimed to provide a closure model for the mean chemical reaction source term, or turbulence-chemistry closure problem. In the flamelet approach, a closure model for the turbulence-chemistry closure by assuming a very thin reaction zone, or flamelet. A schematic diagram of Flamelet concept in a turbulent flame is shown in Figure 2.3, following Venkatesh & Abraham (2002).

In the flamelet approach for non-premixed combustion systems, the turbulent flame is understood as an ensemble of instantaneous flame fronts, width of which are much smaller than characteristic length scale of turbulent eddies as shown in Figure 2.3(a). These instantaneous flame fronts are wrinkled by the turbulent eddy motion as shown in Figure 2.3(b). The structure of laminar flame is retained in the thin reaction zone, which is usually referred to as *flamelet*. Since the characteristics of laminar flame structure is maintained in these instantaneous flame fronts, it is not required to determine the turbulent mean reaction source term. The mixing between fuel and oxidizer at the instantaneous flame front is modeled by a counterflow flame configuration as shown in Figure 2.3(b). As a result, instantaneous change due to chemistry can be determined by the laminar vaporization-reaction equation (3.4).

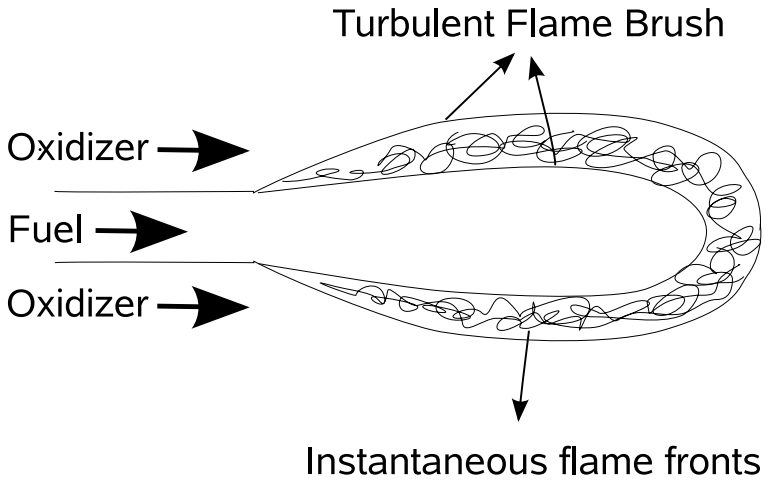

(a) Turbulent Flame

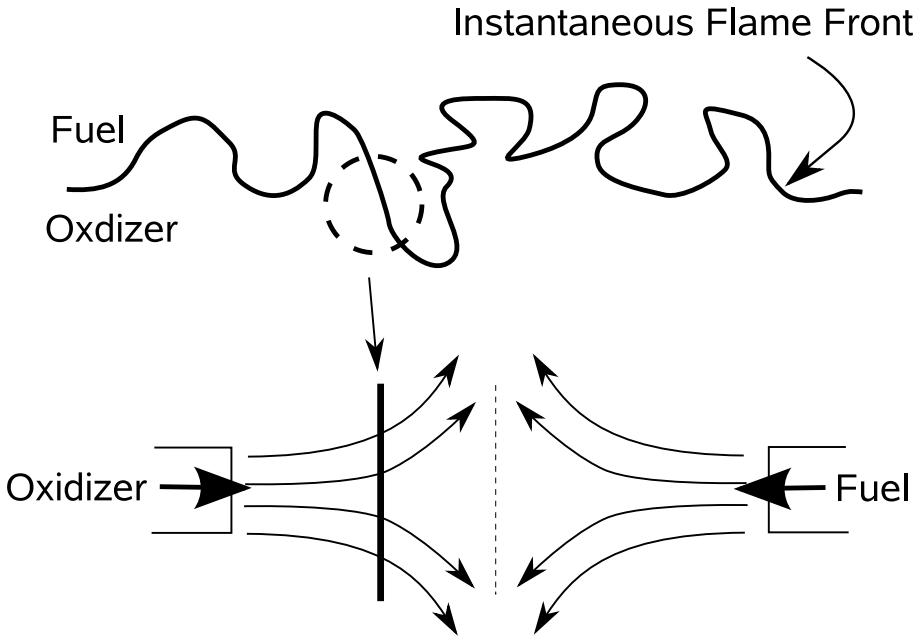

(b) Flamelet Concept

Figure 2.3: Laminar Flamelet Concept in a Turbulent Reacting Flow

2.3.4 Turbulent Reaction Equation

Even though the flame structure in the thin reaction zone, or flamelet, maintains the laminar flame structure, the effect of turbulence should be considered for the scalar dissipation rate χ. The scalar dissipation rate in the flamelet model is the single variable which carries the turbulence information from the flow field to the reaction space. As the scalar dissipation rate should be determined from the physical space considering turbulence, $\tilde{\chi}_Z$ will be used in the reaction equation, instead of instantaneous χ. The turbulent scalar dissipation rate $\tilde{\chi}$ will be discussed in detail in Section 2.3.6.

$$\rho \frac{\partial Y_i}{\partial t} = \frac{\rho}{Le} \frac{\tilde{\chi}_Z}{2} \frac{\partial^2 Y_i}{\partial Z^2} + \omega_i \tag{2.25}$$

2.3.5 Presumed PDF approach

The mean value in the physical field is determined by taking statistical average for instantaneous species information stored in the reaction space. It should be noted that not only Z, but also χ in the laminar vaporization-reaction equation (3.4) are fluctuating quantities in the turbulent field. Therefore, two PDFs, one for Z and the other for χ are required in the presumed PDF approach to describe the turbulent field. The mean turbulent species information is determined by a double integral.

$$\tilde{Y}_i(t,\vec{x}) = \int_o^1 \int_{-\infty}^{\infty} \tilde{P}_\chi(\chi) \tilde{P}_Z(Z) Y_i(Z) \mathrm{d}\chi \mathrm{d}Z \tag{2.26}$$

In the classic flamelet approach, the PDF for χ is usually assumed to be a delta function at the conditional Favre mean value $\tilde{\chi}_Z$. Then the integration can be simplified to:

$$\tilde{Y}_i = \int_0^1 Y_i(Z) \tilde{P}(Z) \mathrm{d}Z \tag{2.27}$$

To perform the integration (2.27), the information on the probability distribution func-

tion, or PDF $\tilde{P}(Z)$, is required. One way to determine the PDF is to analytically formulate and solve a transport equation for PDF's, like in PDF methods (Pope, 1985). Another commonly used method is to assume a predefined shape of PDF based on physical observation. This method is commonly referred as a presumed PDF approach (Peters, 2000). A beta function PDF (2.28) is widely used in non-premixed turbulent combustion, and will be used in this research.

$$\tilde{P}(Z;t,\mathbf{x}) = \frac{Z^{\alpha-1}(1-Z)^{\beta-1}}{\Gamma(\alpha)\Gamma(\beta)}\Gamma(\alpha+\beta) \tag{2.28}$$

where
$$\alpha = \tilde{Z}\gamma \tag{2.29a}$$
$$\beta = (1-\tilde{Z})\gamma \tag{2.29b}$$
$$\gamma = \frac{\tilde{Z}(1-\tilde{Z})}{\widetilde{Z''^2}} - 1 \geq 0 \tag{2.29c}$$

2.3.6 Scalar Dissipation Rate

The scalar dissipation rate is the most important parameter in the flamelet approach. It conveys the effect of turbulence in the physical space to the reaction space. Also it is the single variable by which the physical space and reaction space communicate with each other.

The instantaneous scalar dissipation rate is defined by a square of gradient of conserved scalar.

$$\chi = 2D|\nabla Z|^2 \tag{2.30}$$

Note that χ is a function of Z. In a simple configuration such as infinite mixing layer or counterflow flame, $\chi(Z)$ can be determined analytically. Analytical solutions of $\chi(Z)$ from different flow configurations have been determined by different researchers as listed below.

- One-D mixing layer (Pitsch & Peters, 1998)

$$\chi(Z) = \frac{1}{2\pi t} \exp\left(-2\left[erfc^{-1}(2Z)\right]^2\right) \tag{2.31}$$

- Infinite one-D mixing layer (Pitsch *et al.* , 1998)

$$\chi(Z) = \chi_{\mathrm{st}}(\frac{Z}{Z_{\mathrm{st}}})^2 \frac{ln(Z/Z_{\mathrm{max}})}{ln(Z_{\mathrm{st}}/Z_{\mathrm{max}})} \tag{2.32}$$

- Counterflow (Peters, 1984)

$$\chi(Z) = \frac{a}{\pi} \exp\left(-2\left[erfc^{-1}(2Z)^2\right]\right) \tag{2.33}$$

It should be noted that $\chi(Z)$ formula listed above are based on one dimensional flow field, where χ can be determined analytically using one-to-one mapping of Z and x. However, the same strategy may not be applied to a full three dimensional flow. Peters (2000) suggested to use a presumed shape of χ from analytical solutions to represent χ as a function of Z.

In the physical space, a mean value of χ, or $\tilde{\chi}$ evaluated at each $(t,\vec{x})$ is the only scalar dissipation rate related variable. It is required to determine the scalar dissipation rate as a function of Z to be solved in the reaction space.

First, the mean scalar dissipation rate can be determined by splitting Z into mean and variance, then taking an average in the physical space.

$$\tilde{\chi} = 2D\widetilde{|\nabla Z''|^2} \tag{2.34}$$

and is modeled by turbulence variables, with $c_\chi = 2.0$ as follows.

$$\tilde{\chi} = c_\chi \frac{\tilde{\varepsilon}}{\tilde{k}} \widetilde{Z''^2} \tag{2.35}$$

The mean scalar dissipation rate determined by (2.35) is evaluated at each $(t,\vec{x})$, and is not yet a function of Z. A mean scalar dissipation rate should be determined as a function of Z to be used in solving turbulent flamelet equation (3.42). To determine the mean scalar

dissipation rate as a function of Z, a functional dependency of χ on Z over a known function is assumed at a fixed value such as Z_{st}.

$$\chi_Z = \chi_{st} \frac{f(Z)}{f(Z_{st})} \tag{2.36}$$

The function $f(Z)$ is one of the analytical solutions listed above which best describes the mixing field, which in this case is (2.32). The value of $\tilde{Z}_{st}$ is to be determined from the turbulent flow field. A relationship between $\tilde{\chi}$ and $\tilde{\chi}_{st}$ can be determined from known PDF.

$$\tilde{\chi} = \int_0^1 \tilde{\chi}_Z \tilde{P}(Z) \mathrm{d}Z = \tilde{\chi}_{st} \int_0^1 \frac{f(Z)}{f(Z_{st})} \tilde{P}(Z) \mathrm{d}Z \tag{2.37}$$

which leads to an equation to evaluate $\tilde{\chi}_{st}$ at $(t, \vec{x})$.

$$\tilde{\chi}_{st}(t, \vec{x}) = \tilde{\chi}(t, \vec{x}) \frac{f(Z_{st})}{\int_0^1 f(Z) \tilde{P}(Z) \mathrm{d}Z} \tag{2.38}$$

where $\tilde{\chi}(t, \vec{x})$ is modeled by turbulence variables as (2.35). A volumetric average of local scalar dissipation rate was suggested (Pitsch *et al.* , 1998) to determine a nominal value of $\tilde{\chi}_{st}$.

$$\tilde{\chi}_{st} = \frac{\int_V \tilde{\chi}_{st}(t, \vec{x})^{3/2} \bar{\rho} \tilde{P}(Z_{st}) \mathrm{d}V}{\int_V \tilde{\chi}_{st}(t, \vec{x})^{1/2} \bar{\rho} \tilde{P}(Z_{st}) \mathrm{d}V} \tag{2.39}$$

Once $\tilde{\chi}_{st}$ for whole combustion chamber is determined by (2.39), $\tilde{\chi}_Z(Z)$ can be determined by (2.36) with known function $f(Z)$, such as the one shown in (2.32).

Chapter 3

Extensions of RIF model to Account for the Effect of Vaporization in the Reaction Space

3.1 Flamelet Approach Applied to Direct Injection

The flamelet approach, or more specifically the RIF model has been widely used in non-premixed combustion systems including spray combustion devices such as direct injection compression ignition engines. However, the RIF framework was developed based on a pure gaseous non-premixed combustion, while DICI is basically a two-phase reacting flow where droplet vaporization occurs to provide gaseous fuel for combustion.

Efforts have been made to improve the RIF model for DICI modeling , or more generally, spray combustion systems. One of the most common approaches is to consider only the change in local $\tilde{Z}(t,\vec{x})$ by droplet vaporization, while model constants for spray models are calibrated, as Weber & Peters (2006) suggested. Otherwise, the classic flamelet approach was kept in its original form. This implies that the reaction space will be kept the same as for non-vaporizing case, regardless of droplet vaporization in the physical space.

Other approaches have been investigated by researchers to properly account for the effect of direct injection in the context of flamelet approach. Different formulation of governing equations in the context of the flamelet approach applied to spray combustion are summarized in Table B.1 for comparison. In this section, the effect of direct injection on the flamelet modeling and related modeling efforts will be described.

3.2 Effects of Direct Injection

The effect of direct injection may be categorized into two major categories:

3.2.1 Increased Turbulence

To facilitate mixing between the fuel and the oxidizer, typically the fuel is injected at high pressure resulting in high injection velocity. The injection velocity may reach up to 50000 cm/sec with injection pressure close to 100 MPa with diesel engines utilizing a common rail injection system. Droplets injected at such high velocity increase turbulence in the flow field by interacting with the in-cylinder gas mixture. Modeling of increased turbulence in the context of flamelet models will be discussed in detail in Section 3.5.2 after description of turbulence treatment. As the current study aims to properly capture the effect of fuel addition on the reaction space, the effect of increased turbulence will be covered briefly with current modeling issues.

3.2.2 Addition of Fresh, Unreacted Fuel

When direct injection is applied, injected fuel droplets vaporize by heat transfer from high temperature ambient gas. Droplet vaporization provides unreacted fuel for subsequent mixing and combustion. In the flamelet approach, this would affect the reaction space itself by changing both Z and $Y_i(Z)$ values at the same time.

For example, in conventional flamelet models, each point Z_a and Z_b in the reaction space carries their own reaction history by solving the reaction equation (3.42). This is shown schematically in Figure 3.1.

Two different locations or computational cells $\vec{x}_a$ and $\vec{x}_b$ are marked on the LHS, which represents the physical space. On the RHS, a fuel species reaction space governing the physical space is shown, assuming some degree of reaction. Two locations having different Z values will have different amount of fuels from the reaction space, reflecting different

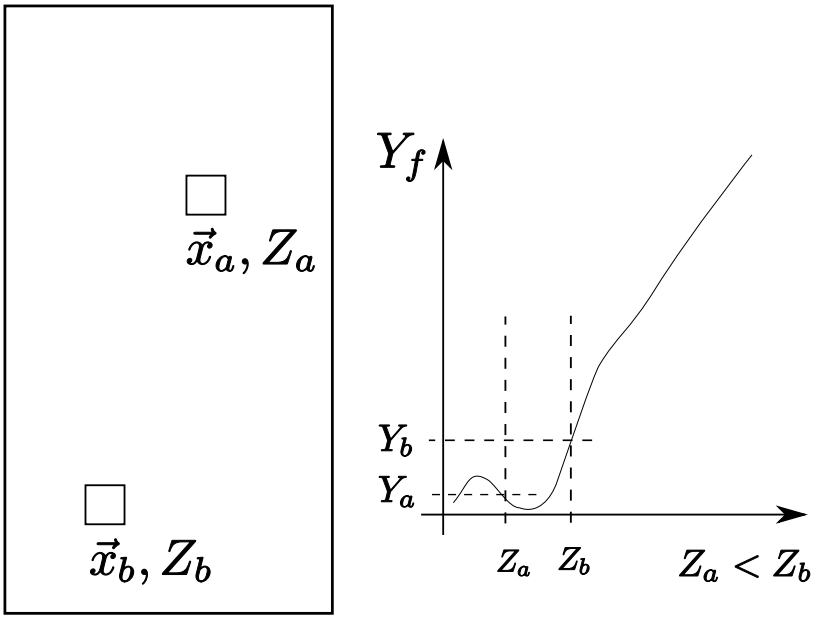

Figure 3.1: Schematic Diagram Comparing Reaction Space Without Vaporization

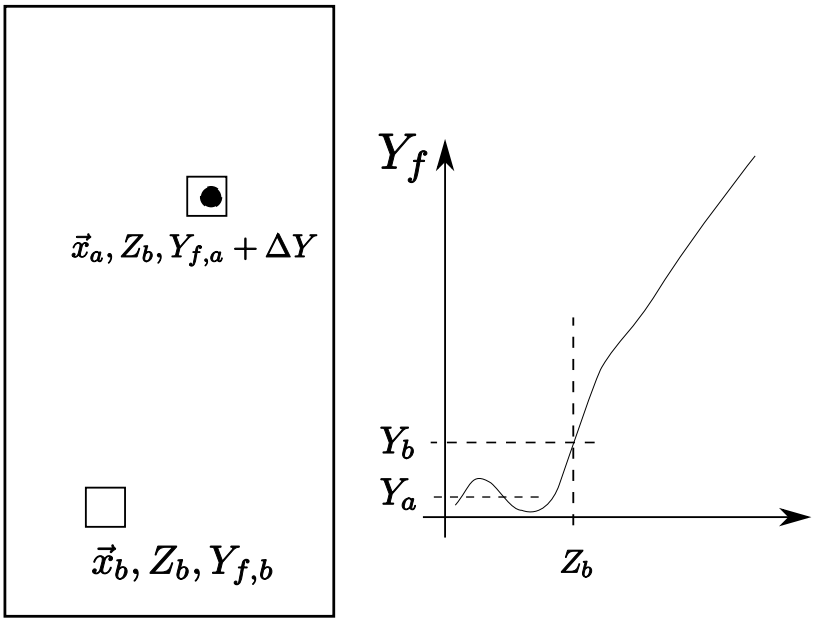

Figure 3.2: Schematic Diagram Comparing Reaction Space With Vaporization

reaction histories.

Let us assume a case where vaporization occurs at location $\vec{x}_a$, such that Z value at this location is increased from Z_a to Z_b. In such case, species mass fractions at these values in the reaction space should communicate with each other, such that the mass fraction at $\vec{x}_a$ may be informed of vaporization history. Otherwise, both locations $\vec{x}_a$ and $\vec{x}_b$ will have the same amount of fuel even though vaporization and reaction histories at these locations are different. This is shown in Figure 3.2. Locations $\vec{x}_a$ and $\vec{x}_b$ have undergone different vaporization history. However, after the vaporization, both locations have the same Z value at $Z = Z_b$. In the conventional flamelet approach, these two computational cells will have the same amount of fuel from the reaction space. The current study aims to suggest a methodology to account for such vaporization history under spray combustion for better combustion modeling.

3.3 Representative Interactive Flamelet Model for Evaporation Effect in Reaction Space: RIF-ER

In this research, effort has been made to properly account for the effect of droplet vaporization in the reaction space. We will begin by re-driving the governing equations in both the physical space and the reaction space to identify terms regarding the effect of vaporization.

3.3.1 Governing Equations

A species transport equation with droplet vaporization and chemistry is shown in (3.1).

$$\rho\frac{\partial Y_i}{\partial t} + \rho\vec{u}\cdot\nabla Y_i = \rho D\nabla^2 Y_i + \dot{\rho}_i + \omega_i \tag{3.1}$$

In (3.1), $\dot{\rho}_i$ represents the addition of species mass due to vaporization of injected droplets, and ω_i represents the chemical source term from reaction. The vaporized mass $\dot{\rho}_i$ is determined by CFD solver, considering related droplet physics. In most cases, vapor-

ization is considered for one single fuel species in computational modeling of spray, where $\dot{\rho}_i = 0$ except $\dot{\rho}_{\text{fuel}}$.

Physical Space: Conserved Scalar Transport Equation

A conservation equation for the conserved scalar under spray combustion can be derived from the mass conservation equation (3.1).

$$\rho \frac{\partial Z}{\partial t} + \rho \vec{u} \cdot \nabla Z = \rho D \nabla^2 Z + \dot{\rho}_Z \tag{3.2}$$

$\dot{\rho}_Z$ represents the vaporization source term. It should be noted that $\dot{\rho}_Z$ has the same value with $\dot{\rho}_{\text{fuel}}$ for single species fuel vaporization. Details of this relationship can be found in Appendix A.

Reaction Space: Vaporization-Reaction Equation

A coordinate transformation (2.10) is carried out on (3.1) to determine the governing equation in the reaction space.

$$\rho \frac{\partial Y_i}{\tau} + \frac{\partial Y_i}{\partial Z}\left[\rho \frac{\partial Z}{\partial t} + \rho \mathbf{u} \cdot \nabla Z - \nabla \cdot (\rho D_i \nabla Z)\right] = \rho \frac{\chi}{2} \frac{Le_Z}{Le_i} \frac{\partial^2 Y_i}{\partial Z^2} + \omega_i + \dot{\rho}_i \tag{3.3}$$

The same assumptions of constant unity Lewis number for each species are applied to (3.3) as (2.18). In the flamelet approach with gaseous medium, the terms in brackets in LHS would have been canceled out by the Z transport equation (2.6). However, the Z transport equation (3.2) does not match the terms in brackets in (3.3) like its gaseous counterpart. Rather, the terms in the brackets will have a value equal to $\dot{\rho}_Z$ from the Z transport equation. As a result, the final equation governing reaction space becomes:

$$\rho \frac{\partial Y_i}{\partial t} + \dot{\rho}_Z \frac{\partial Y_i}{\partial Z} = \rho \frac{\chi}{2} \frac{Le_Z}{Le_i} \frac{\partial^2 Y_i}{\partial Z^2} + \omega_i + \dot{\rho}_i \tag{3.4}$$

Equations (3.2) and (3.4) are the final equations in direct injection case, each governing the physical space and the reaction space. These equations enables proper consideration of vaporization effect in the reaction space, which will be referred to as Representative Interactive Flamelet Model accounting for Evaporation effect in the Reaction space (RIF-ER).

3.3.2 Vaporization History Effect

In this section, the effect of two additional terms in (3.4) will be described. Two source terms were identified in (3.4) from the consideration of vaporization in the reaction space. The effect of these source terms will be examined over the reaction space as shown in Figure 3.3.

In Figure 3.3, $m_i(Z)$ relationship for the fuel species in the reaction space is shown. First, the vaporization effect is realized in the physical space by solving the Z transport equation (3.30), which is to be reflected by an increase in Z, as shown in Figure 3.3(a). Previous applications of the RIF model in spray combustion has considered this effect as the governing equations listed in Table B.1. However, previous research did not consider the effect of vaporization in the reaction space. As a result, the fuel species after vaporization would have been determined as shown in Figure 3.3(b) by looking up m_i value corresponding to $Z(t+\Delta t)$. As shown in Figure 3.3(b), this would result in fuel mass m^*, which is less than the fuel mass before vaporization. Such prediction is due to the fact that the $Y_i(Z)$ or $m_i(Z)$ is determined by solely considering the effect of turbulence, but not by the effect of vaporization. The current $m_i(Z)$ profile is chosen to present a case where such approach should fail. The effect of vaporization should be considered to properly determine the fuel mass after the vaporization, rather than using $Y_i(Z)$ or in this case, the $m_i(Z)$ relationship.

The actual amount of fuel species after vaporization at $Z(t+\Delta t)$ should be the sum of *the original fuel amount before vaporization* and *the fuel amount added by vaporization*.

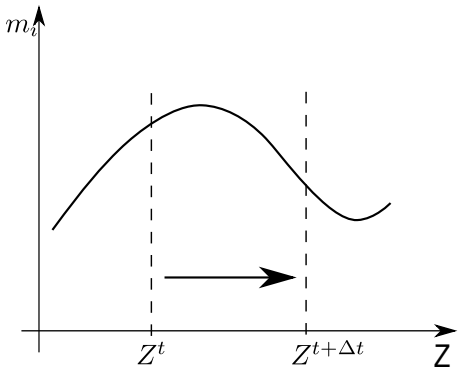

(a) Increase in Z by Z transport equation

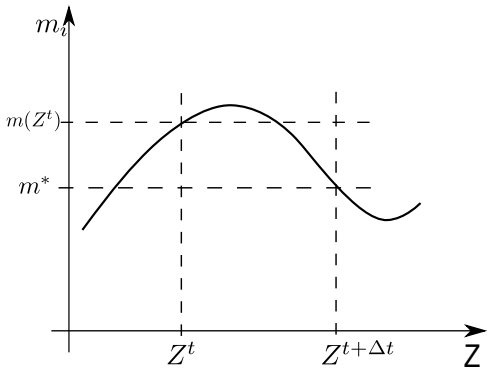

(b) Fuel mass determined by $Y_i(Z)$: Conventional Approach Without Vaporization Consideration

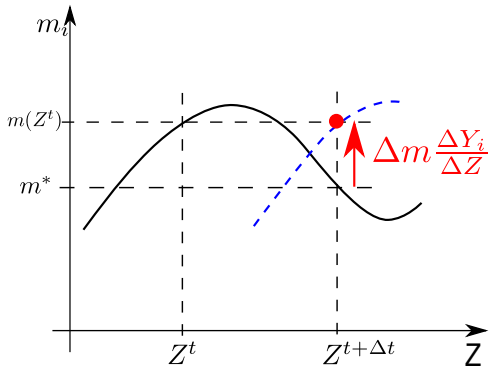

(c) Determination of fuel mass before vaporization

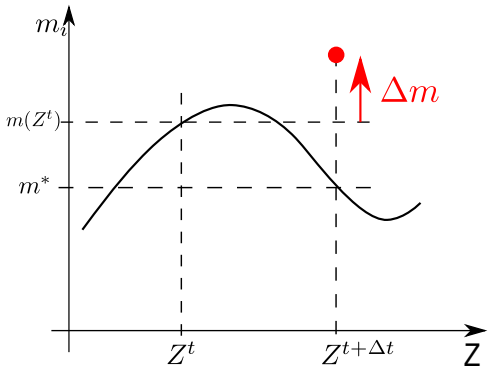

(d) Addition of vaporized fuel mass

Figure 3.3: Effect of additional terms in flamelet equation

$$m_i(t+\Delta t, Z(t+\Delta t)) = m_i(t+\Delta t, Z(t)) \quad \textit{fuel amount before vaporization}$$
$$+\Delta m_i \qquad\qquad \textit{added fuel by vaporization} \tag{3.5}$$

Two additional terms in (3.4) account for this effect. For simplicity of discussion, a time-splitting scheme between vaporization terms and diffusion-reaction terms in (3.4) is assumed. The vaporization equation is shown below.

$$\rho \frac{\partial Y_i}{\partial t} = -\dot{\rho}_Z \frac{\partial Y_i}{\partial Z} + \dot{\rho}_i \tag{3.6}$$

Note that (3.6) is being evaluated after vaporization. The convection-like term has been moved to the RHS. The role of this term is to determine *the original fuel amount before vaporization* by subtracting $\Delta Y(\Delta Z)$, as shown in Figure 3.3(c). This convection-like term can also be interpreted as translation of the original curve by the amount of ΔZ in the direction of negative $\partial Y_i/\partial Z$ at $Z(t+\Delta t)$ as plotted in a dashed line in the same plot. This can be better understood if (3.6) is rewritten in a discretized form.

$$m_i^{t+\Delta t}(Z^{t+\Delta t}) = \underbrace{\left[m^t(Z^{t+\Delta t}) - \Delta m \left.\frac{\Delta Y_i}{\Delta Z}\right|_{Z^{t+\Delta t}} \right]}_{\text{Species amount before vaporization at } Z(t+\Delta t)} + \underbrace{\Delta m}_{\text{amount of added species}} \tag{3.7}$$

Then, $\dot{\rho}_i$ is added to represent *fuel amount added by vaporization* as shown in Figure 3.3(d). In other words, the convection-like term determines the fuel amount before vaporization by linear approximation, then the actual amount of fuel added by vaporization is added to get the correct value of fuel amount after vaporization.

These two additional terms account for the vaporization history. Without these terms, each m_i value in the reaction space carries its own reaction history, completely unaware of vaporization. These additional terms convey the vaporization history into the reaction space by properly accounting for the addition of fresh fuel from vaporization.

3.3.3 Droplet Vaporization Treatment

The vaporization equation (3.4) has been properly derived from relative governing equations. The effect of vaporization terms in (3.4) has been analyzed in Section 3.5.3. This section will discussed how to evaluate these vaporization terms to properly reflect the effect of vaporization into the reaction space. The reaction equation with vaporization terms is rewritten for convenience of discussion.

$$\rho \frac{\partial Y_i}{\partial t} + \dot{\rho}_Z \frac{\partial Y_i}{\partial Z} = \rho \frac{\chi}{2} \frac{Le_Z}{Le_i} \frac{\partial^2 Y_i}{\partial Z^2} + \omega_i + \dot{\rho}_i \tag{3.8}$$

Let us consider only the effect of vaporization by neglecting the diffusion and chemistry source terms.

$$\rho \frac{\partial Y_i}{\partial t} = -\dot{\rho}_Z \frac{\partial Y_i}{\partial Z} + \dot{\rho}_i \tag{3.9}$$

The linear, convection-like term in (3.9) does subtract some amount of mass to find *the amount of fuel before vaporization*, while the source term is added to properly account for the addition of fuel. In other words, the information required in solving (3.9) are:

- Z value before vaporization
- mass fraction at Z value before vaporization
- increase in Z value due to vaporization

,which are evaluated deterministically in the physical space by a CFD solver. As a result, instead of solving (3.9), it is possible to use an algebraic relationship to update the reaction space to reflect the effect of vaporization.

First, Z values before and after vaporization are determined from the CFD solver KIVA3v

by vaporization subroutine `evap`, where the following equation is solved.

$$\frac{\partial\left(\bar{\rho}\tilde{Z}\right)}{\partial t}=\dot{\bar{\rho}}_Z \tag{3.10}$$

This equation is solved in the Phase A in KIVA3v[1], where no cell boundary transport is assumed. Recall that $\dot{\rho}_f=\dot{\rho}_Z$ as discussed in Appendix A, since a single species of liquid vaporization is assumed. After discretization, (3.10) becomes:

$$\frac{\sum_i m_i^*-\sum_i m_i}{V\Delta t}=\frac{\Delta m_f}{V\Delta t} \tag{3.11}$$

where an asterisk is used to denote properties at $t+\Delta t$. Since $\dot{\rho}_f=\dot{\rho}_Z$, it follows that $\Delta m=\Delta Z$. Then Δm can be found as:

$$\Delta m=\sum_i m_i\frac{\Delta Z}{1-Z^*} \tag{3.12}$$

$$=\sum_i m_i\frac{Z^*-Z}{1-Z^*} \tag{3.13}$$

Then, it is possible to determine the mass after vaporization by simply adding Δm from (3.12) to the known mass value at Z before vaporization, instead of solving (3.8) in the reaction space. Now the following equations are solved to evaluate mass fractions after vaporization in the reaction space.

$$m_i^*=m_i+\Delta m_i \tag{3.14}$$

$$=\begin{cases} m_i+\sum_i m_i\dfrac{Z^*-Z}{1-Z} & \text{for fuel species} \\ m_i & \text{for all other species} \end{cases} \tag{3.15}$$

[1]Refer to Section 3.6.1 for details on KIVA3v.

Then information on Y_i^* at $t+\Delta t$ can be determined by normalizing m_i^*'s as follows. First, for the fuel species,

$$Y_f^* = \frac{m_f^*}{\sum_i m_i^*} \tag{3.16}$$

$$= \frac{m_f + \sum_i m_i \frac{Z^* - Z}{1 - Z^*}}{\sum_i m_i + \sum_i m_i \frac{Z^* - Z}{1 - Z^*}} \tag{3.17}$$

$$= \frac{Y_f + \frac{Z^* - Z}{1 - Z^*}}{1 + \frac{Z^* - Z}{1 - Z^*}} \tag{3.18}$$

$$Y_f^* = \frac{Y_f + \alpha}{1 + \alpha} \tag{3.19}$$

$$\text{where} \quad \alpha = \frac{Z^* - Z}{1 - Z^*} \tag{3.20}$$

Then for all other species,

$$Y_i^* = \frac{Y_i}{1 + \alpha} \tag{3.21}$$

$$\text{where} \quad \alpha = \frac{Z^* - Z}{1 - Z^*} \tag{3.22}$$

By (3.19) and (3.21), it is possible to determine Y_i^* after vaporization from known $Z, \Delta Z$ and Y_i values. Now let us examine what these equations represent in the reaction space.

Equation (3.18) can be rewritten into:

$$Y_f^* = \frac{Y_f + \frac{Z^* - Z}{1 - Z^*}}{1 + \frac{Z^* - Z}{1 - Z^*}} \tag{3.23}$$

$$= \frac{(1 - Z^*)Y_f + Z^* - Z}{1 - Z} \tag{3.24}$$

$$= \frac{1 - Z^*}{1 - Z} Y_f + \frac{Z^* - Z}{1 - Z} \tag{3.25}$$

$$= Y_f + (Z^* - Z)\frac{1 - Y_f}{1 - Z} \tag{3.26}$$

Equation (3.26) can be visualized in the reaction space, as shown in Figure 3.4.

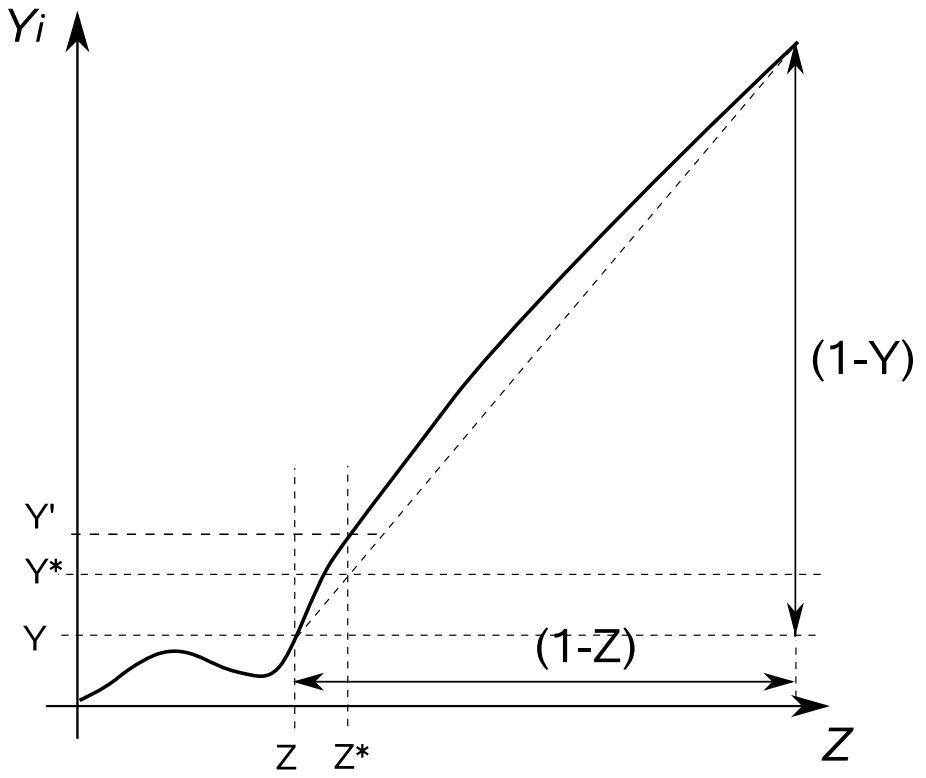

Figure 3.4: Equation (3.26) in the Reaction Space

A fuel mass fraction profile in the reaction space is given in Figure 3.4 for illustrative purpose. Z values before and after vaporization (Z and Z^*) are shown on Z axis. What needs to be determined after vaporization is the true fuel mass fraction Y^* after the vaporization. The new mass fraction Y^* determined from (3.26) is simply a linear approximation of Y_f^* using Y_f value before vaporization to the pure fuel Y_f value, which in this case is located at $Z = 1$.

As the line connecting Y_f and $Y_f(Z = 1)$ represents a pure mixing line, the physical meaning of 3.26 can be interpreted from Figure 3.4. The fuel mass fraction after vaporization is determined by a pure mixing between Y_f before vaporization and pure fuel, evaluated at Z^*.

From the above discussion, it can be concluded that the vaporization effect can be treated without iteration from known Z and Y_i values. As a result, it is not necessary to solve the re-derived reaction equation (3.10) as a whole. A first order operating splitting scheme is applied such that the vaporization effect can be updated in a single step without any iteration.

$$\frac{\partial(\rho Y^*)_i}{\partial t} = -\dot{\rho}_Z \frac{\partial Y_i^n}{\partial Z} + \dot{\rho}_i \tag{3.27}$$

$$\rho \frac{\partial Y_i^{**}}{\partial t} = \frac{\tilde{\chi}_Z}{2} \frac{\partial^2 Y_i^*}{\partial t^2} + \omega_i \tag{3.28}$$

$$Y^{n+1}(t+\Delta t, Z) = Y^{**}(t+\Delta t, Z) \tag{3.29}$$

3.3.4 Effect of Droplet Vaporization Terms

One very interesting observation can be made from Figure 3.4. If no fuel addition was modeled by the vaporization terms, the predicted fuel mass fraction at Z^* is determined by the fuel mass fraction evaluated at Z^*. This value is presented as Y' in Figure 3.4. It is worth to notice that the fuel mass fraction predicted by vaporization terms Y^* is smaller than the fuel amount Y' determined without vaporization consideration. A more general explanation on the fuel mass prediction can be summarized as follows based on relative amount of fuel species gradient versus $(1-Y_f)/(1-Z)$ and reaction progress in the reaction space.

1. $\left.\frac{\partial Y_f}{\partial Z}\right|_{Z^*} = \frac{1-Y_f}{1-Z}$

   Consideration of vaporization terms will predict the same amount of fuel species as the classic RIF model without vaporization consideration. This is observed when the progress in reaction is yet not significant.

2. $\left.\frac{\partial Y_f}{\partial Z}\right|_{Z^*} < \frac{1-Y_f}{1-Z}$

   This is a case with local species gradient in the reaction space is smaller than $(1-Y_f)/(1-Z)$. As a result, consideration of vaporization terms result in increase in

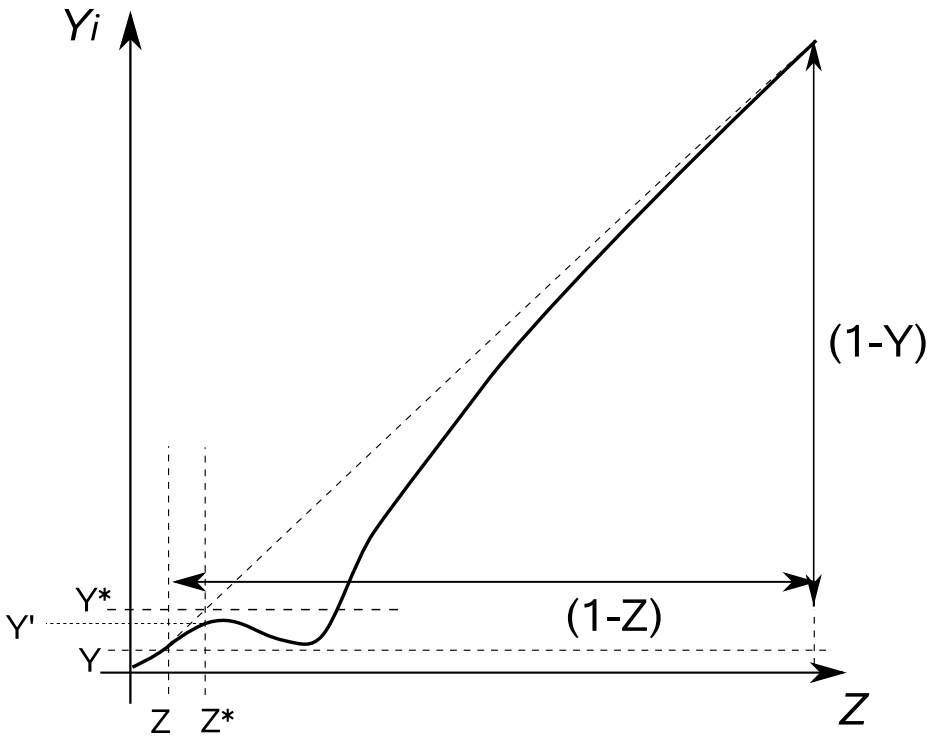

(a) Effect of Vaporization Terms: Increasing Fuel Content

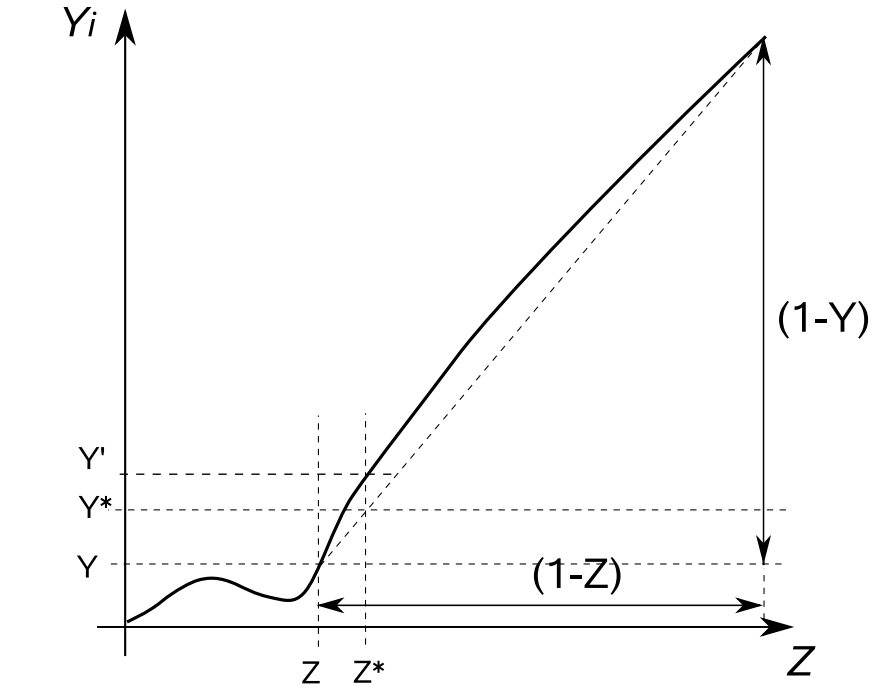

(b) Effect of Vaporization Terms: Decreasing Fuel Content

Figure 3.5: Effect of Vaporization Terms in the Reaction Space: Comparison of Fuel Species Amount Prediction with RIF model

fuel amount compared to the no vaporization consideration case. This is shown in Figure 3.5(a), with mass fraction after vaporization with the vaporization source term is shown as Y^*, while without vaporization source term is shown as Y'. In this case, $Y^* > Y'$. This occurs mostly on the lean side.

3. $\left.\frac{\partial Y_f}{\partial Z}\right|_{Z^*} > \frac{1-Y_f}{1-Z}$

   In this case, $(\mathrm{d}Y_f/\mathrm{d}Z)$ is larger than $(1-Y_f)/(1-Z)$. This occurs where significant reaction is occurring. As a result, consideration of vaporization terms result in decrease in fuel amount compared to the no vaporization consideration case. In this case, $Y^* < Y'$. This occurs mostly on the rich side.

It should be noted that the increase or decrease in fuel amount by droplet vaporization consideration, as depicted in Figure 3.5, may be interpreted as an indicator for the progress in reaction. More fuel species may be interpreted as less reaction progress and vice versa. In general, the RIF model predicts lower fuel content than the RIF-ER model within lean range, where the RIF results can be interpreted as predicting faster reaction. As a result, higher pressure and temperature than the RIF-ER model will be predicted in the physical space.

3.4 Effect of Droplet Vaporization Terms

3.4.1 Introduction

The droplet vaporization source terms in the reaction equations were examined and interpreted in the previous section. In this section, a quantification study of these terms will be attempted over a spray combustion case within an idealized control volume.

The RIF-ER model is focusing on capturing the effect of fresh fuel addition by fuel injection and following vaporization. However, fuel injection and droplet physics requires highly complicated models and empirical constants as mentioned by Weber & Peters

(2006). Moreover, local vaporization rate is determined by local temperature, pressure and droplet conditions, which are affected by conditions at the previous time step. Most importantly, due to the cumulative nature of vaporization and combustion, the local vaporization rate will differ from the RIF model and the RIF-ER model, which will affect results in subsequent time steps. As a result, it becomes not an easy task to separately examine the effect of vaporization source terms in (3.4).

An idealized setup is suggested to consider the effect of fresh fuel addition separated from direct injection. In this setup, vaporized fuel mass in the gas phase is assumed to be added to a computation cell, which is governed by a reaction space. By assuming fixed amount of vaporized mass addition, the spray-related effects can be isolated to solely consider the effect of fuel addition.

In a spray combustion system, the effect of vaporization is realized at different time steps based on the relative distance from the nozzle. This is schematically shown in Figure 3.6. For example, a location near the nozzle exit would experience the effect of vaporization at an early stage of reaction space evolution. This corresponds to $\vec{x}_1$ in Figure 3.6. In this case, the effect of vaporization may not affect the reaction space, since the reaction space has not undergone significant reaction to remain close to its mixing limit.

On the other hand, a location far downstream from the exit nozzle will experience vaporization after certain amount of time. The reaction space would have evolved to some degree as shown in the bottom right in Figure 3.6 when the vaporization is realized at this location of $\vec{x}_3$. In this case, the effect of vaporization will affect the reaction space.

In this section, three different locations in a hypothetical spray combustion will be examined to investigate the effect of vaporization terms. These locations will be chosen to represent a near nozzle exit location, downstream and far downstream of the nozzle exit condition. The effect of vaporization at these locations will be analyzed by considering an idealized control volume to investigate the effect of vaporization terms at different stages of the reaction space evolution.

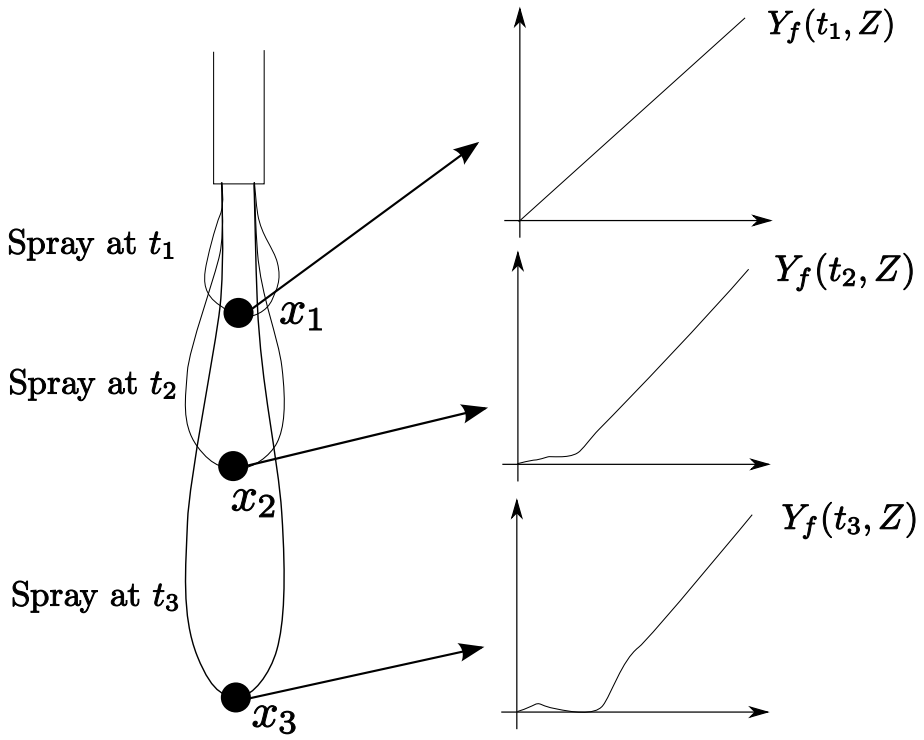

Figure 3.6: Schematic diagram showing different stage of flamelet evolution at fuel addition in a spray

3.4.2 Simulation Setup

Each of these locations, x_1, x_2 and x_3 will be modeled as an idealized control volume, which is assumed to have prescribed $\tilde{Z}$ and $\widetilde{Z''^2}$ values. For simplicity, the cell is assumed to have negligible diffusion or convection mass transfer through its boundaries. The only mass transfer will occur by fuel addition which will be added at a prescribed rate in the gas phase. A scalar dissipation rate $\tilde{\chi}_{\text{st}}$ is also prescribed for the cell, such that there exists subgrid level turbulence mixing. It is further assumed that $\tilde{\chi}_{\text{st}}$ is fixed and does not change. It is being assumed that fuel droplet introduced into this cell is vaporized as soon as it is injected. A schematic diagram is shown in Figure 3.7. Fuel species used in the numerical experiment is n-heptane, and a reaction mechanism suggested by Liu *et al.* (2004) was used to model the chemical kinetics.

To maintain similar rate of vaporization, a constant increase in $\tilde{Z}$ value over fuel addition duration was assumed. It is possible to compare the effect of fuel addition separately

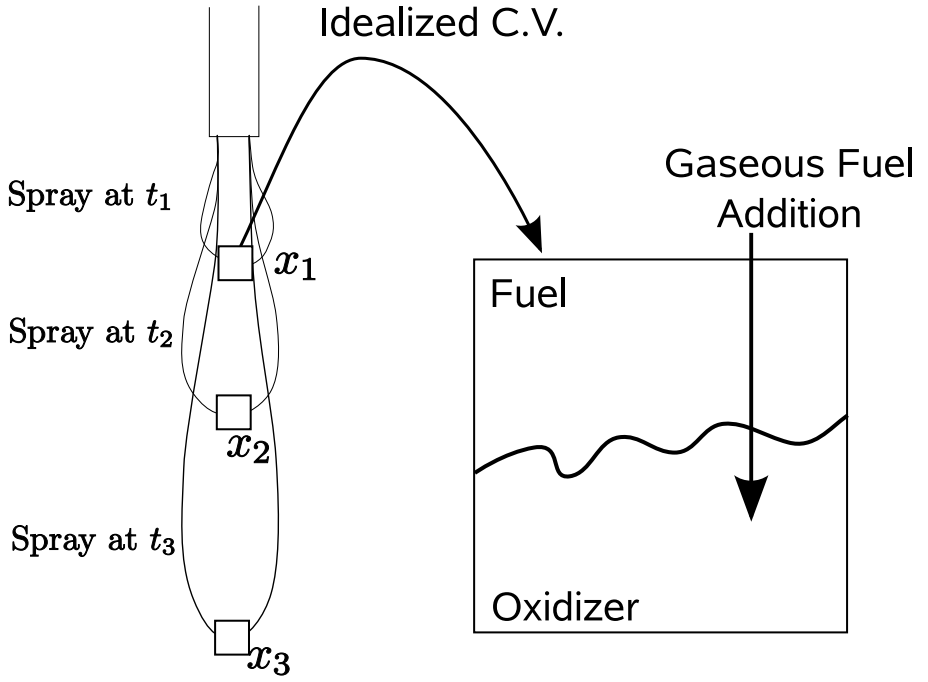

Figure 3.7: Schematic Diagram of Idealized Control Volume and Fuel Addition

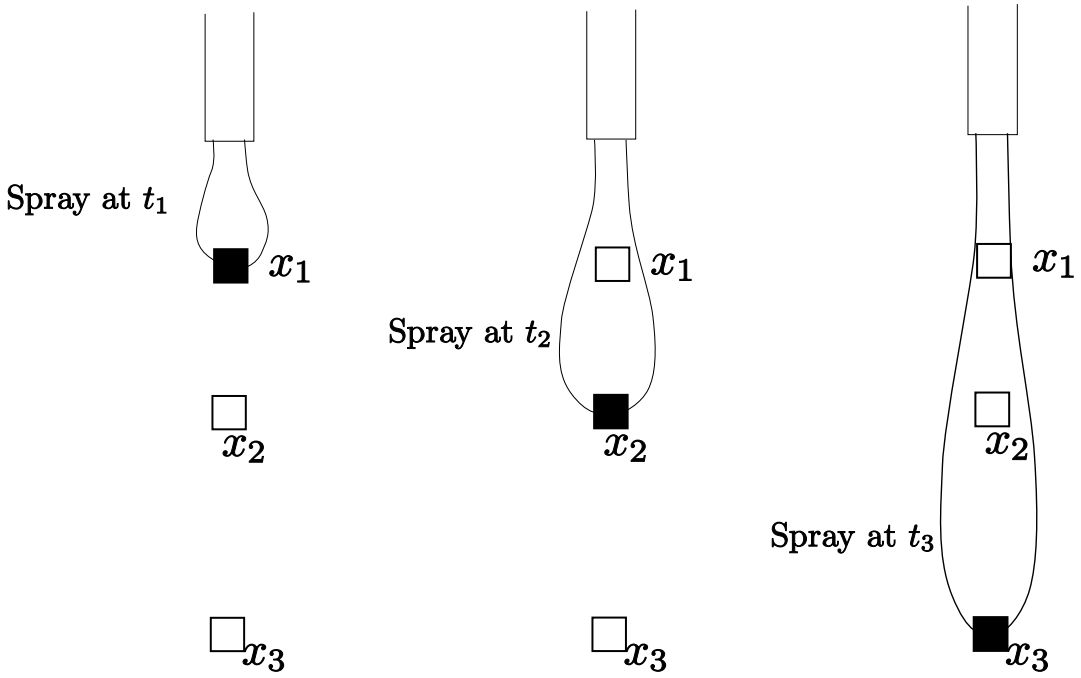

(a) Case A (b) Case B (c) Case C

Figure 3.8: Schematics of Different Cases

Table 3.1: Control Volume Configuration

Initial $\tilde{Z}$	$0.5 \times Z_{st}$
$\Delta\tilde{Z}$ by fuel addition	$\Delta Z = Z_{st}$
Final $\tilde{Z}$ after fuel addition	$1.5 \times Z_{st}$
Initial $\widetilde{Z''^2}$	0.08
$\tilde{\chi}$	30 sec^{-1}
$T(Z=1)$, fuel stream temperature	572 K
$T(Z=0)$, oxidizer stream temperature	920 K
Pressure	40 bar

Table 3.2: Vaporization Configuration

	Case A	Case B	Case C
Fuel addition begins at	0.1 ms	0.3 ms	0.5 ms
Fuel addition duration		0.1 ms	

from other effects regarding fuel droplet and vaporization history by applying a specified rate of fuel addition.

Three sets of fuel addition cases were examined using the RIF-ER code as shown in Table 3.2. These three cases were chosen such that each case A, B and C may be interpreted as near nozzle exit condition, downstream location and further downstream from nozzle exit, as shown in Figure 3.8. It is being assumed that the reaction space is activated at the same time for all three cases, such that the same reaction history is maintained for all cases before vaporization or effective fuel addition occurs. In all cases, the initial Z values are set to $0.5 \times Z_{st}$, or equivalence ratio of 0.48. Fuel addition occurs at constant rate over 0.1ms for the initial mixture to reach $Z = 1.5 \times Z_{st}$, or equivalence ratio of 1.59. Constant fuel stream temperature was assumed for the temperature of added fuel.

It should be noted that the aim of the current simulation is not to solve the entire spray combustion structure, but to examine the effect of fuel addition at different stages of the reaction space evolution within a spray. Figure 3.8 is provided to facilitate understanding of the control volumes. Only the reaction space is being solved for these three cases with initial conditions prescribed in Table 3.1 and Table 3.2.

3.4.3 Results of Numerical Experiments Using Idealized Control Volume

Results: Case A

Temperature and pressure histories from Case A are shown in Figure 3.9. The RIF results are shown in dashed lines, while the RIF-ER results are plotted in solid lines. The fuel addition begins at 0.1ms with 0.1ms duration of fuel addition as shown in Figure 3.9(a). The fuel addition occurs very early like in cells near the nozzle exit as depicted in Figure 3.8(a). As a result, both the RIF and the RIF-ER predict similar results. This is mainly due to the fact that the reaction space has not evolved significantly at this time step, and the reaction space is still at its mixing limit, close to the initial condition[2]. The fuel mass fractions in the reaction spaces are shown in Figure 3.10, at the beginning of fuel addition in Figure 3.10(a) and at the end of fuel addition in Figure 3.10(b).

Again, the RIF results are shown in dashed lines and the RIF-ER results are shown in solid lines. From Figure 3.10, it is observed that the reaction space has not undergone significant reaction. The additional source terms in (3.4) are pushing the fuel mass fractions to the mixing limit as vaporization occurs. However, in this case, the fuel mass fractions are still at the mixing limit even at the end of fuel addition. As a result, the RIF-ER model result does not differ significantly from the RIF results, as shown in Figure 3.9 and Figure 3.10.

It should be noticed that the vaporization terms in (3.4) do not affect the reaction space after the end of vaporization or fuel addition. If there is no significant difference at the end of fuel addition, the reaction spaces from the RIF and RIF-ER models become quite similar in the time period after the end of fuel addition. Hence, under such circumstances, the RIF-ER model results are identical to the RIF model.

[2] see Figure 2.2 for the species profile at the mixing limit

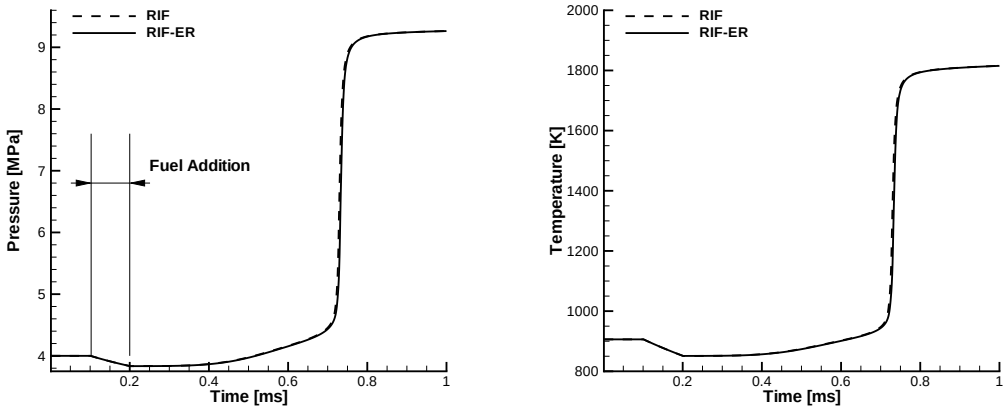

(a) Pressure Comparison (b) Temperature Comparison

Figure 3.9: Pressure and Temperature History of Case A

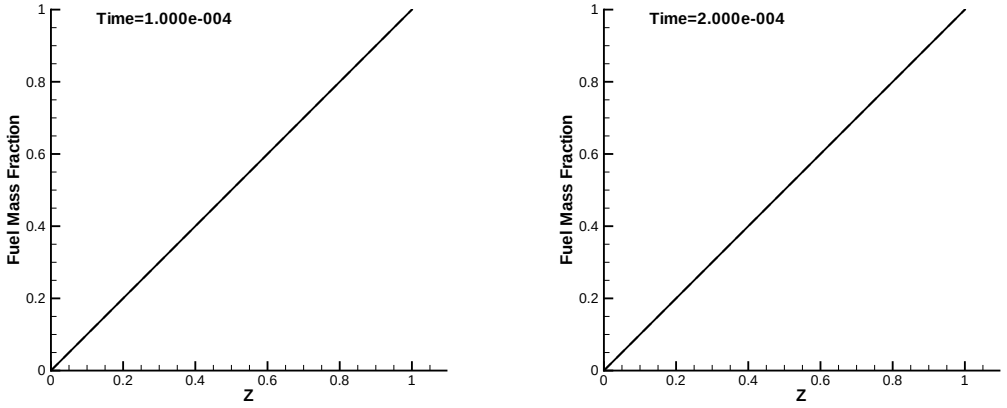

(a) Fuel species at the beginning of Fuel Addition: Case A (b) Fuel species at the end of Fuel Addition: Case A

Figure 3.10: Fuel Species Mass Fraction in the Reaction Space: Case A

Results: Case B

Case B represents a case where fuel addition effect is realized later than in Case A. Pressure and temperature history plots for Case B are shown in Figure 3.11. This case corresponds to a mixture at a downstream spray location, as shown in Figure 3.8(b) and the second row in Table 3.2. Again, the RIF results are plotted in dashed lines, and the RIF-ER results are plotted in solid lines.

The results are similar to Case A. The pressure and temperature histories do not differ much between the RIF and the RIF-ER models. The fuel species mass fraction in the reaction space at the beginning and the end of fuel addition timing are shown in Figure 3.12, when the Z axis has been scaled to better examine differences in the results.

First, at the beginning of fuel addition as shown in Figure 3.12(a), there are no significant difference between the RIF and the RIF-ER results. However, at the end of fuel addition, difference between the RIF result and the RIF-ER result is observed. The RIF result, which is shown in a dashed line, shows faster fuel consumption than the RIF-ER result. While the RIF-ER result shown in the solid line is still very close to the mixing limit, implying that the fuel addition effect is considered. This difference is still not significant and does not significantly affect actual pressure and temperature in the control volume as shown in Figure 3.11.

Results: Case C

The pressure and temperature plots for Case C with the RIF and the RIF-ER model are shown in Figure 3.13. One significant difference from the previous two cases is that the RIF-ER model predicts longer ignition delay than that of the RIF model. The increased ignition delay is due to the increased fuel amount by fuel addition and following endothermic reaction to fuel breakdown to smaller radicals.

The fuel mass fraction in the reaction space for Case C at the beginning and the end of fuel addition are shown in Figure 3.14. There are a few noticeable differences at the begin-

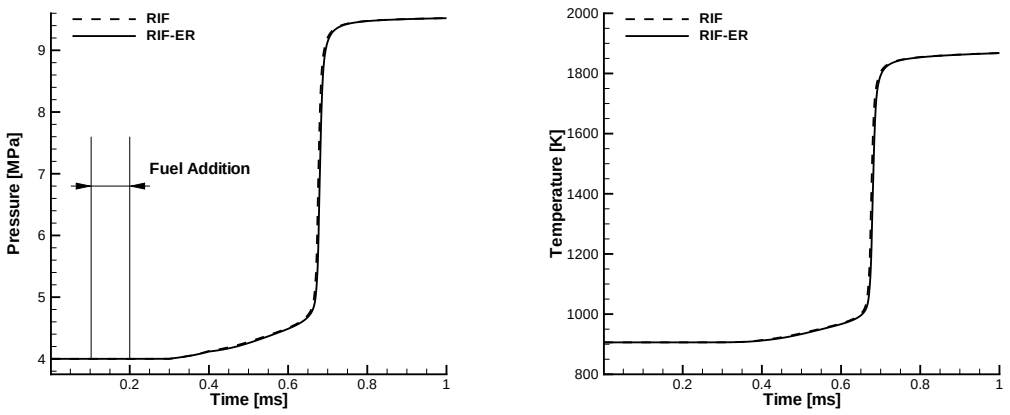

(a) Pressure Comparison (b) Temperature Comparison

Figure 3.11: Pressure and Temperature History of Case B

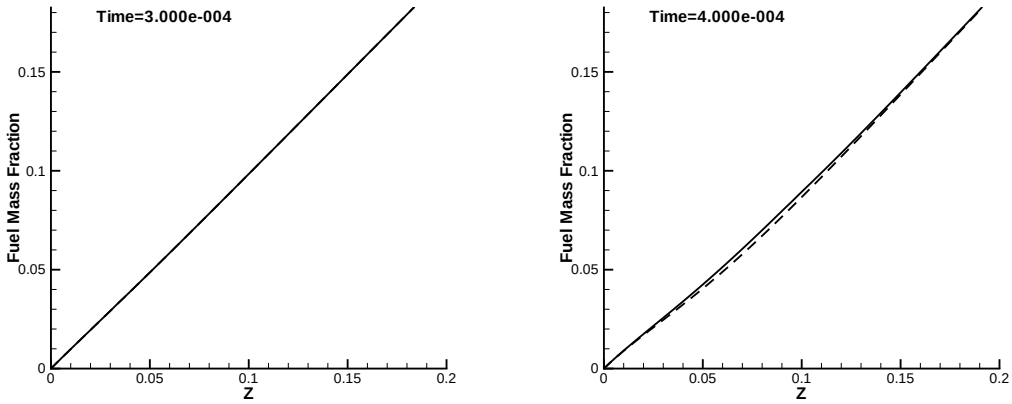

(a) Fuel species at the beginning of Fuel Addition: Case B (b) Fuel species at the end of Fuel Addition: Case B

Figure 3.12: Fuel Species Mass Fraction in the Reaction Space: Case B

ning of fuel addition from previous cases. First, some partial reaction has occurred in the reaction space as shown in Figure 3.14(a), while the fuel species mass fractions in previous two cases were still at their mixing limit, as shown in Figure 3.10(a) and Figure 3.12(a). The other difference is a tiny peak shown in Figure 3.14(a), which represents the amount of fuel being added near $Z = 0.03$ where the fuel addition was assumed to occur. During the fuel addition period, not only the reaction but also the fuel addition is modeled in the RIF-ER model, such that at the end of fuel addition, as shown in Figure 3.14(b), there exists significant difference in the fuel mass fraction in the reaction space between the RIF model and the RIF-ER model. As a result, longer ignition delay is being predicted from the RIF-ER model in the physical space as shown in Figure 3.13.

3.5 Consideration of Turbulence in Turbulent Spray Combustion Modeling with the RIF-ER Model

The vaporization-reaction equation (3.4) was derived in the context of a laminar flame. In this section, the suggested model will be extended to turbulent spray combustion. Details of turbulent non-premixed combustion modeling using the laminar flamelet approach was presented in Section 2.3 following Peters (2000). In this section, only additional consideration regarding spray combustion will be described.

3.5.1 $\tilde{Z}$ Transport Equation in Turbulent Spray Combustion

The governing equations for $\tilde{Z}$ is modified to consider the spray source terms.

$$\bar{\rho}\frac{\partial \tilde{Z}}{\partial t} + \bar{\rho}\tilde{\vec{u}} \cdot \nabla \tilde{Z} = \nabla \cdot (\bar{\rho} D \nabla \tilde{Z}) + \tilde{\dot{\rho}}_Z \tag{3.30}$$

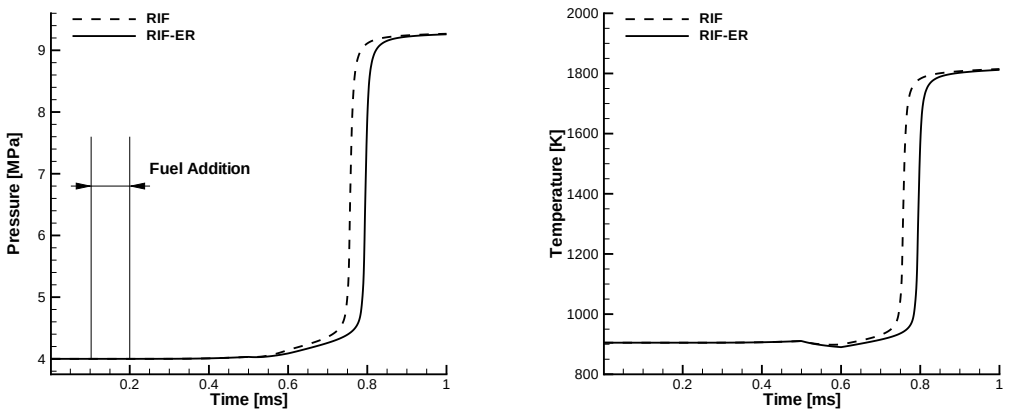

(a) Pressure Comparison (b) Temperature Comparison

Figure 3.13: Pressure and Temperature History of Case C

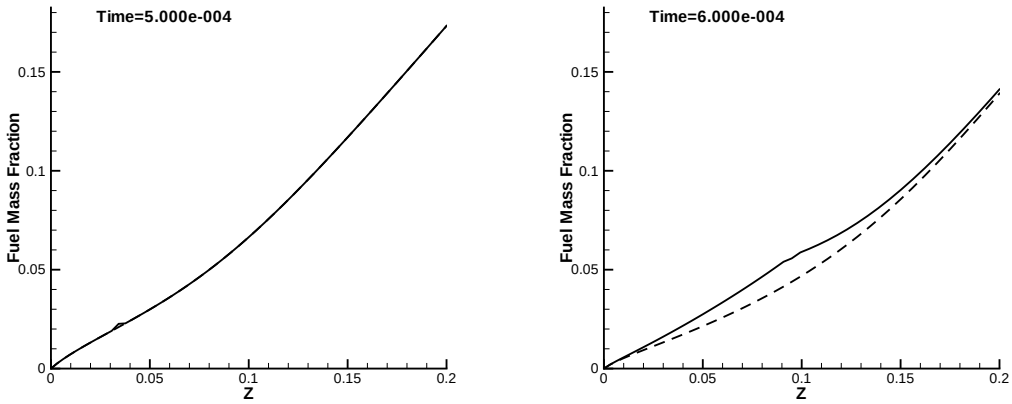

(a) Fuel species at the beginning of Fuel Addition: Case C (b) Fuel species at the end of Fuel Addition: Case C

Figure 3.14: Fuel Species Mass Fraction in the Reaction Space: Case C

3.5.2 $\widetilde{Z''^2}$ Equation in Turbulent Spray Combustion: Effect of Increased Turbulence

Spray injection increases turbulence through the interaction between the fast-moving droplets and the ambient gas. For illustrative purpose, change in turbulent kinetic energy after injection in a diesel engine is shown in Figure 3.15. Clearly, the turbulent kinetic energy increases by almost an order of magnitude by direct injection. In this specific case, the droplet injection velocity was 340 m/s with a fuel injection amount of 3mg.

The increase in turbulent kinetic energy results in an increase in the scalar dissipation rate. In a conserved-scalar based modeling, $\widetilde{Z''^2}$ represents the fluctuation due to turbulence. At the same time, increase in turbulence would result in a different PDF which governs the flow field. Demoulin & Borghi (2002) concentrated their effort to model the effect of increased turbulence to suggest a modified variance equation and a different PDF for the spray.

$$\bar{\rho}\frac{\partial \widetilde{Z''^2}}{t} + \bar{\rho}\tilde{\vec{u}}\cdot\nabla\widetilde{Z''^2} = -\nabla\cdot\left(\bar{\rho}\widetilde{\vec{u}''Z''^2}\right) + 2\bar{\rho}D_t(\nabla\tilde{Z})^2 - \bar{\rho}\tilde{\chi} + 2\bar{\rho}\widetilde{Z\omega_v} - 2\bar{\rho}\tilde{Z}\tilde{\omega}_v + \bar{\rho}\tilde{Z}^2\tilde{\omega}_v - \bar{\rho}\widetilde{Z^2\omega_v} \tag{3.31}$$

$$\text{where} \qquad \dot{\rho}_i = \bar{\rho}\tilde{\omega}_v \tag{3.32}$$

The last four terms on the RHS of (3.31) are additional source terms in the variance equation suggested by Demoulin & Borghi (2002). There exist unclosed terms, which can be further modeled by:

$$\bar{\rho}\widetilde{Z\omega_v} = \sum Z_s^p\frac{\dot{m}_p}{V} \tag{3.33}$$

$$\bar{\rho}\widetilde{Z^2\omega_v} = \sum (Z_s^p)^2\frac{\dot{m}}{V} \tag{3.34}$$

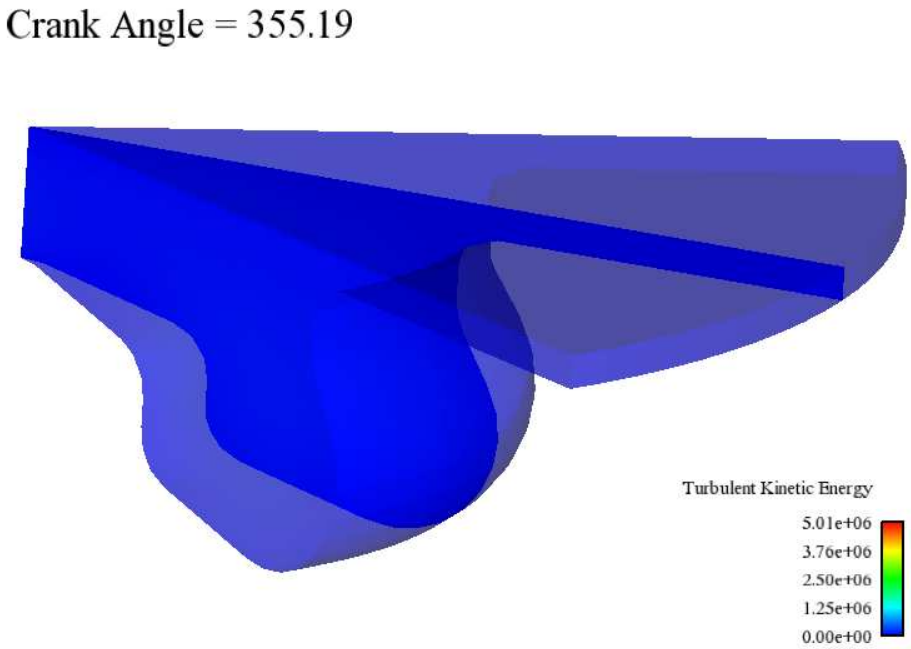

(a) Turbulent Kinetic Energy Before Injection

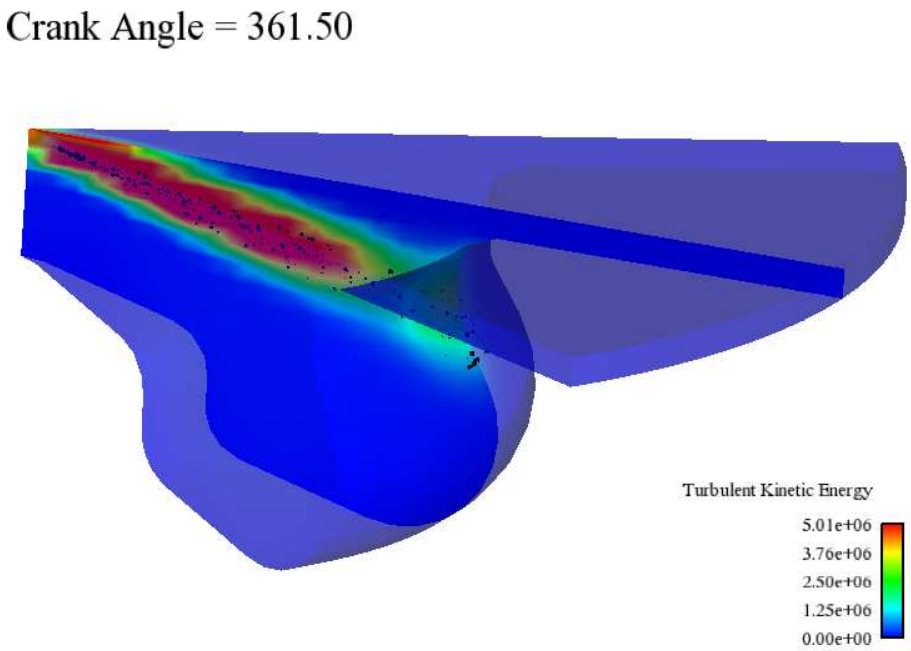

(b) Turbulent Kinetic Energy After Injection

Figure 3.15: Change in Turbulent Kinetic Energy by Direct Injection

where Z_s^p represents Z value on the droplet surface, or Z value at saturation as suggested by Reveillon & Vervisch (2000). However, Ge & Gutheil (2008) reported that such assumption on Z_s value would not be sufficient.

It is worth to notice that if Z_s value is chosen at pure fuel stream with the value of unity, these additional source terms will vanish. In that case, the variance equation becomes identical to the classic flamelet approach as (2.23).

Any value of Z_s less than unity will result in increased $\widetilde{Z''}^2$. Such increase in $\widetilde{Z''}^2$ will first increase the turbulent scalar dissipation rate. In general, increased scalar dissipation rate results in longer ignition delay, since it would require more time for the scalar dissipation rate to become lower than χ_{ig}. Also, it affects the shape of PDF, which is determined as a function of local $\tilde{Z}$ and $\widetilde{Z''}^2$. As a result, proper determination of Z_s becomes of high importance. However, there is not yet a standard model for Z_s.

Kim *et al.* (2004) applied Demoulin's model to a direct injection compression ignition diesel engine to report increased scalar dissipation rate during injection using (3.31) and following increase in ignition delay under late injection cases. Hollmann & Gutheil (1996, 1998) investigated the structure of turbulent spray non-premixed flame based on the flamelet model. In their paper, it was recognized that the structure of the laminar spray flame is considerably different from that of the gaseous flame. The transport equations for the mixture fraction and its variance were modified to include the effect of droplet vaporization (Hollmann & Gutheil, 1996). These models have been emphasizing the effect of spray on the turbulence field.

Even though it has been reported that the increase in turbulence should be accounted for to properly consider spray combustion, there exist uncertainties regarding how to model unclosed terms in the variance equation as described in the above. As a result, in the current study, the conventional variance equation was utilized. Investigating the effect of increased turbulence from the spray will be left for the future work.

3.5.3 Droplet Vaporization Term in the Turbulent Flow Field

In the reaction space, an instantaneous value of $\dot{\rho}_i$ is used to solve the reaction-vaporization equation (3.4). However, the vaporization is considered in CFD solver which solves Favre mean quantities at each computational cell. As a result, the only information regarding the vaporization available is a mean value, $\overline{\dot{\rho}_i}$.

In this research, it is being assumed that the fluctuation in the vaporized mass is negligible, such that a delta function PDF is assumed for the PDF of the vaporized mass.

$$\overline{\dot{\rho}_i} = \bar{\rho}\tilde{\omega}_v \tag{3.35}$$

$$\tilde{w}_v = \int_0^1 \tilde{P}_v(Z)\omega_v \mathrm{d}Z \tag{3.36}$$

$$\tilde{P}_v(Z;t,\vec{x}) = \delta(Z-\zeta(t,\vec{x})) \tag{3.37}$$

In above equations, ζ is used to represent the random variable. The delta function PDF assumption enables the mean value and instantaneous value of the vaporization source term to be directly related to each other.

3.5.4 Droplet Vaporization Term in the Reaction Space

The droplet vaporization term is evaluated at each computational cell in the physical space by the CFD solver. As a result, the vaporization term is defined as a function of $(t,\vec{x})$. This should be determined as a function of Z to be solved in the reaction space (3.4).

A conditional averaging approach was used to determine the vaporization source term as a function of Z.

$$\dot{\rho}(Z) = \langle \dot{\rho}_Z | Z = \zeta \rangle \tag{3.38}$$

$$= \langle \dot{\rho}_Z | \zeta \rangle \tag{3.39}$$

$$= \int_V \dot{\rho}_Z(t,\vec{x}) P_c(Z|\zeta) \mathrm{d}V \tag{3.40}$$

$P_c(Z)$ in (3.40) denotes a conditional probability density function, which is the probability of finding cells with vaporization with $Z = \zeta$ in the whole volume. P_c can be defined as following.

$$P_c(Z|\zeta;t,\vec{x}) = \frac{\int_V \dot{\rho}_Z \delta(Z-\zeta)\mathrm{d}V}{\int_V \dot{\rho}_Z \mathrm{d}V} \tag{3.41}$$

The conditional PDF in (3.41) is normalized mass fraction of vaporized mass for a given Z value.

3.5.5 Turbulent Reaction-Vaporization Equation

The reaction-vaporization in the reaction space is determined as:

$$\rho\frac{\partial Y_i}{\partial t} + \dot{\rho}_Z\frac{\partial Y_i}{\partial Z} = \frac{\rho}{Le}\frac{\tilde{\chi}_Z}{2}\frac{\partial^2 Y_i}{\partial Z^2} + \omega_i + \dot{\rho}_i \tag{3.42}$$

where the turbulent scalar dissipation rate $\tilde{\chi}_Z$ is determined by a log-normal function (2.32) conditioned by χ_{st} as described in Section 2.3.2.

3.6 Implementation into KIVA3v

The suggested model was implemented into the multi-dimensional CFD solver KIVA3v (Amsden, 1997). In this section, a brief description of KIVA3v code structure and necessary modification to the original KIVA3v code will be discussed.

3.6.1 KIVA3v

Significant progress in numerical modeling of internal combustion engines has been made since the late 1970s (Haworth, 2005). The KIVA family of CFD codes was developed by the Los Alamos National Laboratory.

Adaptive Lagrangian-Eulerian Method

KIVA3v was developed based on the Adaptive Lagrangian-Eulerian method (Hirt *et al.* , 1974; Pracht, 1975). Each cycle (one iteration step) is divided into a Lagrangian phase and a rezone phase. Within the Lagrangian phase, each cell is treated as a Lagrangian particle flowing in the flow field without any convection nor diffusion across cell boundaries. Droplet vaporization and chemical reaction are two major subprocesses modeled in the Lagrangian phase. The Lagrangian phase is commonly referred to as *Phase A* in KIVA literature.

In the next phase, *Phase B*, flow related properties, specifically velocities and pressure are solved implicitly using SIMPLE algorithm by Patankar (1980). Diffusion processes of species, turbulence parameters k and ε are solved in this phase.

The Eulerian phase is called *Phase C*. In Phase C, the cell vertices are moved to specified location, and convection and diffusion through cell boundaries are determined by moving the mesh relative to the fluid.

Spray related submodels

A droplet governing equation based on a discrete-particle technique by Dukowicz (1980) is solved in KIVA3v. The initial KIVA code featured a Taylor-Analogy Breakup (TAB) model to model droplet breakup (O'Rouke & Amsden, 1987). The current version of KIVA3v has a breakup model based on Kelvin-Helmholtz theory as suggested by Reitz (1978, 1987), commonly referred to as the *Wave* breakup model.

3.6.2 KIVA3v Integration

A code integration diagram is shown in Figure 3.16. In the CFD code, transport equations for the mean (3.30) and the variance (2.23) of Z are solved instead of species transport equations.

In the CFD solver, total internal energy is chosen as a thermodynamic variable and solved instead of sensible enthalpy in conventional KIVA3v. Turbulence parameter k and ε are solved as well. The turbulent scalar dissipation rate $\tilde{\chi}_{st}$ is determined from a volumetric averaging (2.39). The vaporization source term $\dot{\rho}_Z$ is also determined from the CFD solver.

In the reaction solver, the reaction equation (3.4) is solved. A time-splitting scheme is applied such that the effect of vaporization and diffusion-reaction are treated at separate step within the single time step.

$$Y_i^n(t,Z) = Y(t,Z) \tag{3.43}$$

$$\frac{\partial(\rho Y^*)_i}{\partial t} = -\dot{\rho}_Z \frac{\partial Y_i^n}{\partial Z} + \dot{\rho}_i \tag{3.44}$$

$$\rho \frac{\partial Y_i^{**}}{\partial t} = \frac{\tilde{\chi}_Z}{2} \frac{\partial^2 Y_i^*}{\partial t^2} + \omega_i \tag{3.45}$$

$$Y(t+\Delta t,Z) = Y^{**}(t+\Delta t,Z) \tag{3.46}$$

Chemkin (Kee *et al.* , 1989b,a) is used in the chemistry solver to evaluate thermodynamic properties and reaction rates. An ODE SOLVER (Hindmarsh, 1983; Radhakrishnan

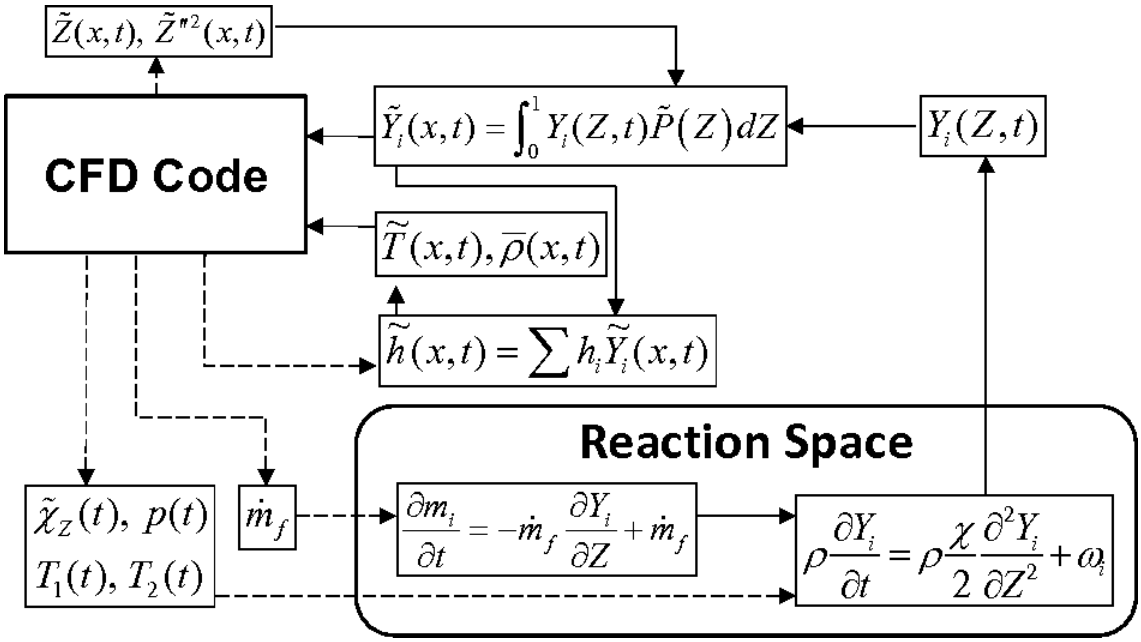

Figure 3.16: Code integration

& Hindmarsh, 1993) is used to solve the system of ordinary differential equations.

3.6.3 Modifications in KIVA3v

As mentioned in Section 3.6.1, KIVA3v relies on Adaptive Lagrangian-Eulerian method, where droplet vaporization and chemistry are solved in the first part of Lagrangian phase. The reaction space solver was implemented at the end of Phase A to match the code flow in the original KIVA3v. A separate subroutine, `spupdate` was implemented for numerical integration (2.27) using `QUADPACK` by Piessens *et al.* (1983). The numerical integration (eqrefeq:6) is called *twice* in a single outer iteration. The first call to `spdupdate` is made at the end of Phase A after the reaction space solvers are called. This updates species information to be used in subsequent energy transport equations. Then, a second call is made at the end of outer iteration to determine actual species value at the end of time step.

Major modifications on the transport equation solvers in KIVA3v were implemented by Hamosfakidis (2006). Species transport equations were replaced by $\tilde{Z}$ and $\widetilde{Z''^2}$ transport equations. The original KIVA3v uses a sensible internal energy with reference temperature of 0 K. However, in the current case, the reaction solver solely treats chemistry. As a result, it is not possible to reflect the change in sensible internal energy from the reaction solver. As a remedy, *total internal energy* is used as the thermodynamic variable instead of the sensible internal energy. The total internal energy is conserved during reaction, which enables the CFD solver to determine local temperature from known species information from the reaction solver and the total internal energy.

3.7 Parallel Implementation

3.7.1 Computational Bottlenecks in General Reacting Flow Modeling

Typically, there exist two computational bottlenecks in computational reacting flow modeling. One is related to the total number of species. With the advent of more strict emissions standards, consideration of detailed chemistry has become necessary to accurately model the emissions species. In general, the number of species considered in a detailed reaction mechanism can be quite large, which implies that species transport equations as many as the total number of species are to be solved in the CFD solver. For example, a reduced mechanism for iso-octane (Chen *et al.* , 2008) used as part of this research has total of 258 species. In this case, at least 258 transport equations for the participating species will be solved in the CFD solver, which creates a huge computational overhead.

In the flamelet model, the number of total transport equations is limited to two regardless of the total number of species participating in the reaction. This is mainly due to the fact that the conserved scalar was chosen to represent the flow field. Therefore, the computational overhead in the flow field is significantly reduced even though a detailed reaction mechanism is applied.

The other bottleneck occurs in the chemistry solver. Again, when detailed chemistry is applied, a system of ordinary differential equations with as many as the number of reactive scalars (species and temperature) is to be solved. If such evaluation is to be considered at each computational cell level, the dimension of the problem leads to *the number of cells* multiplied by *the number of reactive scalars*, which makes the use of detailed chemistry hardly justifiable. In the flamelet approach, the effect of chemistry and reaction is considered in a one-dimensional reaction space which usually has much less grid points than the three-dimensional flow field. However, even with a smaller number of grid points, the computational cost is still considerably high.

In this research, a parallel processing of the chemistry reaction is applied in the reaction

space. The chemistry at each grid point in Z space is distributed to different processors where the reaction is solved. Then updated temperature and species information is returned to the main node, where all related information in Z space is gathered into a single array.

3.7.2 Computational Bottleneck in Reacting Flow Modeling with Flamelet Models

The flamelet approach has one additional computational bottleneck, which is the numerical integration (2.27). Usually, numerical integration with a known function can be carried out quite simply by well known algorithms, such as simple quadrature rules or Simpson's rule (Press *et al.* , 2007). However, the numerical integration in (2.27) has a constraint as it is related to a probability density function, which is:

$$\int_0^1 \tilde{P}(Z)\mathrm{d}Z = 1 \tag{3.47}$$

Equation (3.47) must be satisfied at each computational cell. As a result, more computationally expensive numerical integration algorithms are required, such as adaptive quadrature (McKeeman, 1962). In this research, the adaptive quadrature with step size control was used for the numerical integration using QUADPACK (Piessens *et al.* , 1983).

Not all computational cells undergo the numerical integration at each time step. Especially soon after the start of injection, most of computational cells are still at pure oxidizer state where no integration is required. However, even with a handful of cells being integrated, it was found that the computational time was significantly increased. To reduce computational cost related to the numerical integration, the numerical integration subroutine was parallelized as well, such that the numerical integration of each computational cell is distributed to different processors.

A schematic parallelization flowchart is presented in Figure 3.17. Most of the CFD code is ran in serial, such that the main node solely considers the CFD solver until it reaches reaction subroutines. When the code reaches the chemistry solver subroutine, the main

node (node 0) distributes reactive species at each grid point to each node along with the temperature and pressure information. Each node updates the reactive species information considering chemical kinetics to be returned to the main node. Similar bifurcation occurs at the numerical integration subroutine, where numerical integration at each grid point is carried out by each node.

3.7.3 Parallelization Scaling Study

Two sets of parallelization scaling studies were carried out to examine the performance of the parallel code. In the first case, a three dimensional non-moving mesh of a rapid compression machine was used. While in the second case, a three dimensional moving mesh of a diesel engine was used. In both cases, the maximum number of active computational cells were similar to each other was approximately 15000. However, in the latter case, the total number of active computational cells are changing to reflect the change in cylinder volume during compression and expansion stroke. The number of active cells at TDC is less than 4000.

These two sets of meshes will be used for validation study in Chapter 4. Detailed information on mesh setup and operating conditions can also be found in Chapter 4.

Case 1: Non-moving mesh

The scaling result is shown in Figure 3.18(a) for the non-moving mesh case . The computational mesh is shown in Figure 4.3. From Figure 3.18(a), it can be found that the computational time shows nonlinear decrease with increasing number of processors. This can be attributed to the fact that most part of the CFD code is left at its original serial version. As a result, an absolute amount of computing time is consumed at the main node where the CFD solution is determined. The decrease in the relative time is due to the parallelized part of the code.

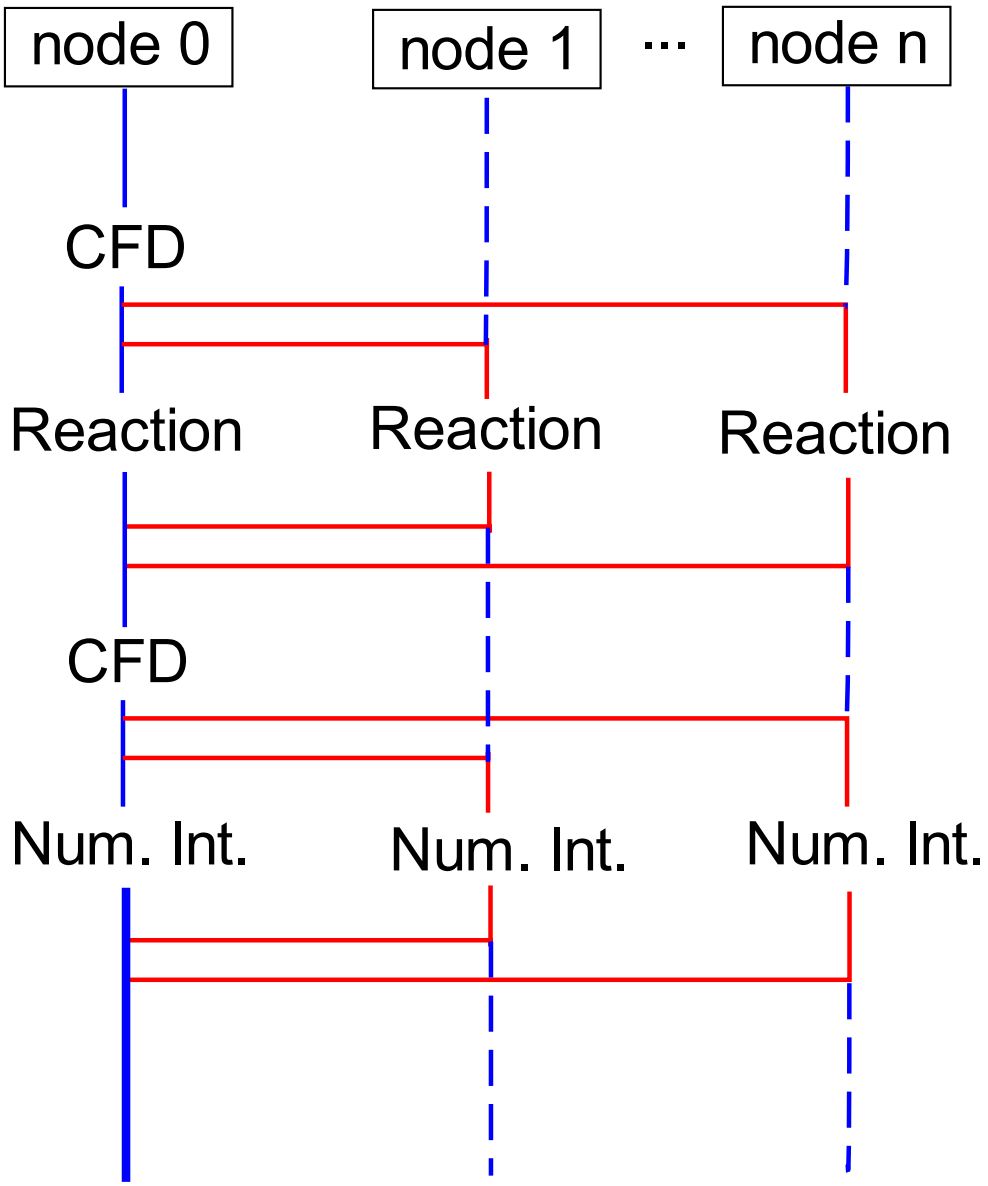

Figure 3.17: Parallel Implementation Flow Chart

Case 2: Moving mesh

The scaling result of a moving mesh is shown in Figure 3.18(b), with the computational mesh shown in Figure 4.17. In this case, the total number of computational cells is not constant. As the simulation runs into the compression stroke, the total number of cells will be decreased while at expansion stroke it will be increased. Overall, the number of computational cells will be less than that of Case 1. Therefore, it could be assumed that the scaling study will exhibit better result than that of Case 1.

However, it was found that the computational time does not scale as well as in Case 1. As shown in Figure 3.18(b), the computational time is almost constant as the number of processors is increased over four. Even the scaling result with two processors shows less than 30% decrease in computing time, which is worse than the scaling for Case 1. It was found that the computational overhead in CFD solver regarding moving boundary treatment is quite large, such that the absolute time required by the serial CFD solver is larger than that of the first case. As a result, the scaling study does not exhibit better result than the first case.

3.8 Summary

A spray combustion model accounting for the effect of vaporization in the reaction space has been suggested based on the flamelet approach of Peters (2000). The proposed model is titled as *RIF-ER* to distinguish itself from the classic RIF model. A brief introduction to the flamelet concept in non-premixed combustion was given in Chapter 2. A governing equation in the reaction space has been successfully derived in Section 3.3.

The governing equations in the RIF model and the RIF-ER model are listed in Table B.1 along with variants of the RIF model such as EPFM. As listed in Table B.1, most of the flamelet approach in spray combustion considers only the $\dot{\rho}_Z$ increase in the physical space by the $\tilde{Z}$ conservation equation. Kim *et al.* (2004) considered the effect of spray on

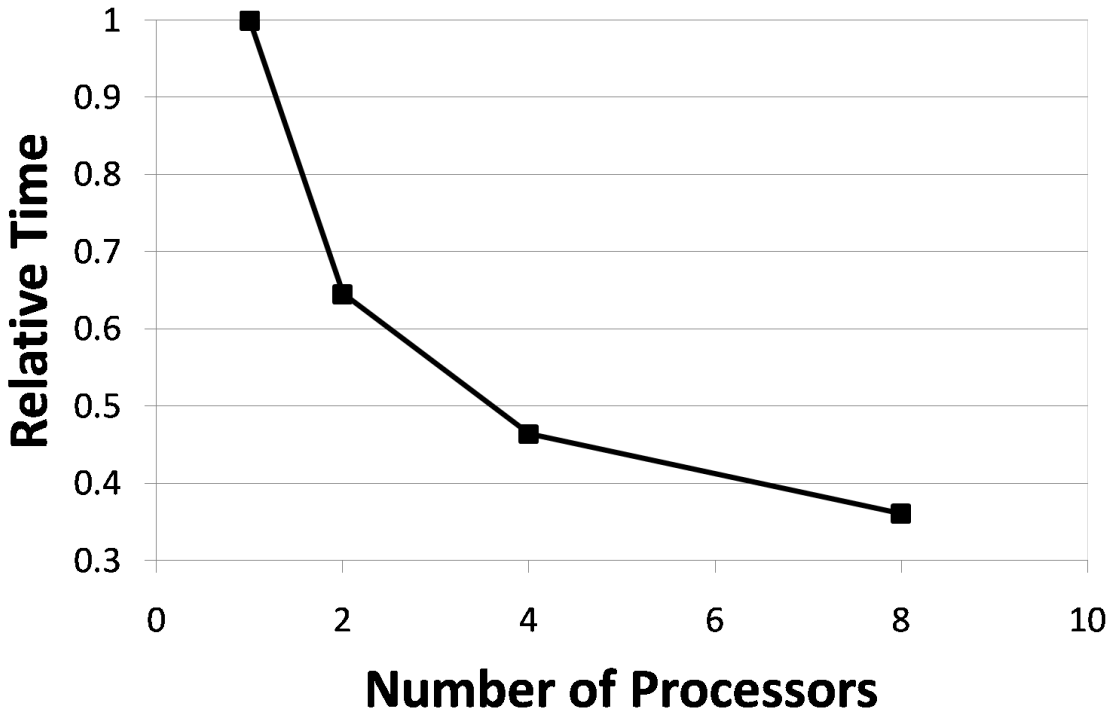

(a) Case 1: Non-moving mesh using RCM

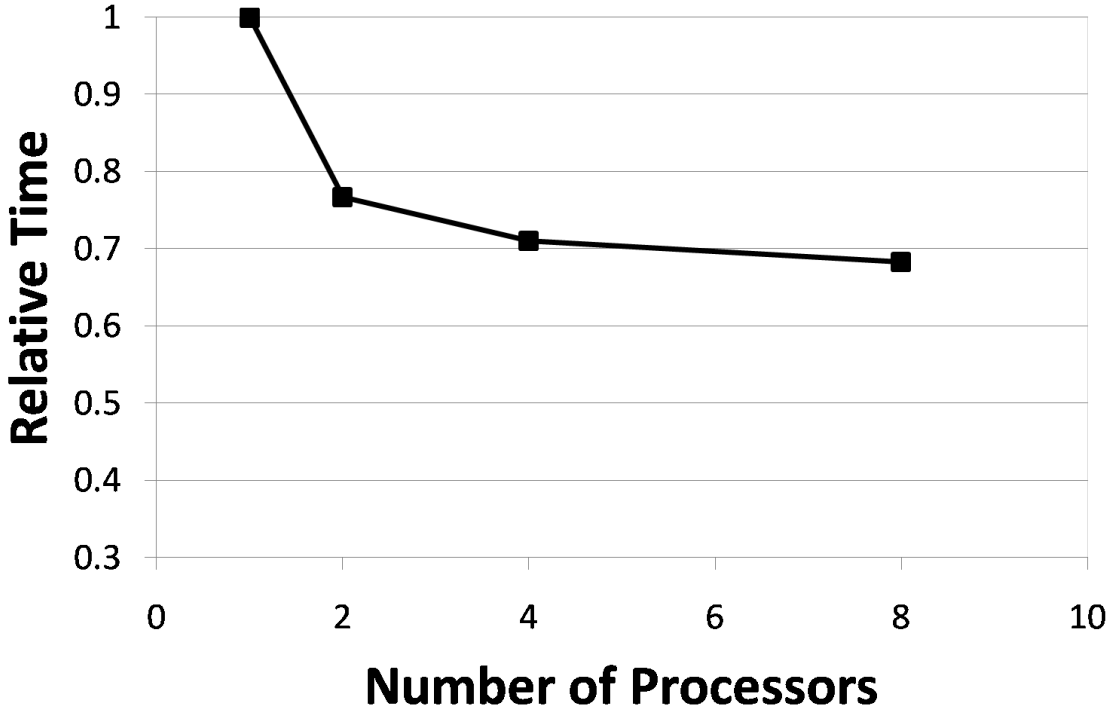

(b) Case 2: Non-moving mesh using diesel engine

Figure 3.18: Scaling Study on Parallelization Performance

turbulence by considering the effect of increased turbulence as listed in the fourth row in Table B.1. None of previous approaches have considered the effect of vaporization as the currently suggested model.

A simple comparison of the RIF and the RIF-ER model has been carried out in a 1-D reaction space to examine the effect of vaporization source terms in (3.4) on the reaction space. A simplified setup has been suggested to separately consider the effect of vaporization from injection and droplet related phenomena.

Three different fuel addition timings were investigated to examine the effect of fuel addition on the reaction space and thermodynamic properties in the physical space. This setup was intended to mimic different conditions in the spray where fuel addition effect is experienced at different time steps.

It was found that fuel addition does not significantly affect combustion in cells where vaporization effect is realized early, since the reaction space is still at its mixing limit. Source terms in (3.4) effectively push the reaction space to the mixing limit. However, if fuel addition occurs early enough, the reaction space has not deviated much from the mixing limit. As a result, the effect of these source terms is small enough to be negligible as shown in Figure 3.9 and Figure 3.11.

The effect of vaporization source terms becomes significant when the fuel addition occurs over a partially reacted mixture, as shown in Figure 3.13 for Case C. Vaporization source terms effectively increase the fuel content in the reaction space, thus increasing the ignition delay.

In spray combustion, the reaction space is initialized as soon as fuel is introduced into the combustion chamber. The reaction space governing the combustion chamber is updated by the reaction equation, maintaining its own time history with $\tilde{\chi}$ provided from the physical space. If vaporization history is not considered properly, at a cell downstream from the nozzle exit will be at partially reacted stage regardless of the amount of fuel introduced into the computational cell. This may result in infinitely fast reaction or *instantaneous* conver-

sion of introduced fresh fuel to combustion product, which will lead to higher temperature and/or pressure than reality for the cell of interest.

These simulations using idealized control volumes revealed that the effect of vaporization source term should be included in the reaction space modeling.

Governing equations for turbulent combustion and turbulence-chemistry closure was discussed in Section 3.5. The spray source term treatment for the turbulence was also discussed. A conditional average was suggested to determine the spray source term $\dot{\rho}_i$ as a function of Z in Section 3.5.3.

Implementation of the suggested model into KIVA3v has been accomplished. Details of the implementation can be found in Section 3.6. The code was parallelized for efficient simulation by taking advantage of multiple processors. The scaling study on the parallel performance can be found in Section 3.7.3.

Chapter 4
Validation of the RIF-ER Model

4.1 Introduction: Validation of a Spray Combustion Model

Turbulent spray combustion is a complex phenomenon including high-speed liquid fuel injection, droplet breakup, droplet vaporization and combustion (Steisch, 2003). Each of these processes requires state-of-the-art submodels, which usually employ empirical constants and correlations. Typically, a spray combustion model consists of two major submodels, a spray injection model and a turbulent non-premixed combustion model. In general, the spray model and the combustion model are validated separately. The spray model is typically validated against non-reacting, purely vaporizing spray experiments, where empirical relationships and constants are determined based on experimental observations. Consequently, the spray model is applied to the reacting case with a turbulent combustion model, where these constants may require further calibrations. Since spray combustion is a cumulative process over time, it makes comparison of different models not an easy task. Typically, validation of the spray combustion model includes comparison of pressure and/or heat release data with experiments along with comparison of combustion images taken from such experiments to numerical results.

4.1.1 Validation Candidates: Spray Combustion Experiments

In this chapter, the suggested model implemented in KIVA3v is applied to actual spray combustion cases. A number of different experimental setups have been considered for

validation in a three dimensional spray combustion case, including the aforementioned experiments by Vogel *et al.* (2005). However, details of the experimental high-pressure vessel were not available in the literature.

Most of the spray combustion experiments were carried out in a co-flow configuration (Goix *et al.* , 1994), which resembles most of spray combustion applications. However, the flamelet approach is based on a counterflow configuration. Hence, a counterflow configuration would suit better for the purpose of validating the current model, which is based on the flamelet approach.

A spray combustion over a counterflow configuration was examined experimentally by Chen & Gomez (1992). In their work, a spray of n-heptane was injected over a counterflow configuration against different strain rates. This would make a a good candidate for validating the suggested model, since the experiment is based on the counterflow flame which the flamelet model is based upon. Numerical simulation results could be compared against Z values within the counterflow flame, which would provide solid comparison between models with and without spray consideration in the reaction space. However, the current computational framework of KIVA3v (Amsden, 1997) is mainly intended to simulate combustion in an internal combustion engine. As a result, the computational framework cannot model such counterflow configuration.

As a result, a spray combustion experiment using a rapid compression machine by Akiyama *et al.* (1998) was chosen as a reference case for model comparison along with the diesel engine experimental data referred in Hong *et al.* (2008). The fuel droplet physics are considered within the multi-dimensional CFD solver KIVA3v (Amsden, 1997). As time progresses, the amount of vaporized fuel may differ between models, which will affect the subsequent reaction into the next time step. Since this study concentrates on the effect of fuel addition in the reaction space and resulting fuel amount in the physical space, comparison of spatial fuel distribution against experimental measurements in a spray combustion system would be an ideal case. However, to the author's knowledge, measurement of fuel

vapor in a reacting flow is still an active research topic. A pioneering work in fuel concentration measurement has been carried out by Vogel *et al.* (2005), where fuel concentration in spray combustion was measured under a diesel-like environment. Some of the interesting findings from Vogel *et al.* (2005) are shown in Figure 4.1.

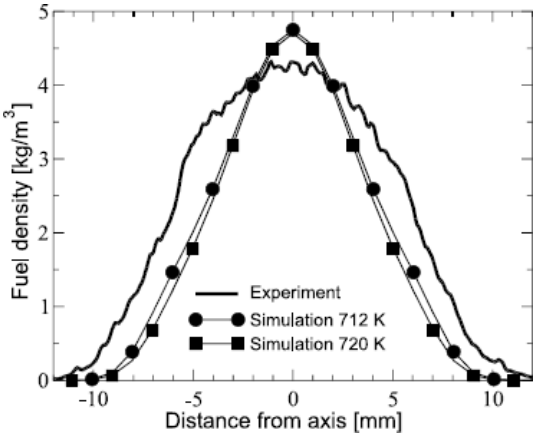

(a) Radial profiles of fuel density at an axial location of 33 mm at 1.0 ms. Comparison between experiment and simulations. Simulations are shown for 712 and 720 K gas temperatures.

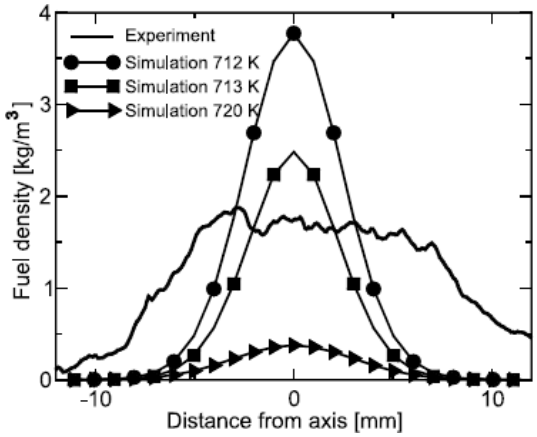

(b) Radial profiles of fuel density at an axial location of 33 mm at 1.5 ms. Comparison between experiment and simulations. Simulations are shown for 712 and 720 K gas temperatures.

Figure 4.1: Spray Combustion Comparison between Measurement and Experiment by Vogel *et al.* (2005)

Radial fuel distribution across the spray is examined at 33mm downstream of the fuel injector for two different time steps, 1.0ms (Figure 4.1(a)) and 1.5ms(Figure 4.1(b)). The lines with markers are numerical results from the RIF model, with different markers representing different initial temperatures. A few different initial temperatures were examined as shown in Figure 4.1. Not surprisingly, macroscopic thermodynamic properties such as overall pressure and temperature traces did not vary much with variations in the initial temperature, while the actual spatial fuel concentration does come out differently with a slight change in the initial temperature, as shown in Figure 4.1(b). Moreover, the fuel concentration profiles for all temperature variation are different from the experimental result. It is being expected that the RIF-ER model should provide better results than the RIF model under similar conditions to Vogel *et al.* (2005).

4.2 Validation Against Spray Combustion Experiment Using a Rapid Compression Machine

Different experimental spray combustion studies were examined to determine suitable data for comparison against numerical results, including experimental works of Chen & Gomez (1992); Goix *et al.* (1994); McDonell & Samuelsen (1995); Akiyama *et al.* (1998) and Vogel *et al.* (2005). The experimental data base of both reacting and non-reacting sprays of McDonell & Samuelsen (1995) have been used as a reference in many papers including Hollmann & Gutheil (1996, 1998). However, the fuel species considered in their experiments was limited to methanol, while we are interested in cases similar to direct injection in an internal combustion engine. Vogel *et al.* (2005) carried out both experimental and numerical studies of spray combustion. This work has been the strongest candidate for validation study of the proposed model. However, details on the combustion facility setup were sparse in the literature. Also, the spray combustion setup utilized a spray injected over a co-flow configuration, which is different from a typical engine environment.

Akiyama *et al.* (1998) conducted a spray combustion experiment using a Rapid Compression Machine (RCM), which resembles the direct injection of an internal combustion engine. The rapid compression machine had a quartz window for visual observation, and some optical measurement data were also available in the aforementioned literature. The experimental setup was found to have enough similarities to direct injection combustion in an internal combustion engines. As a result, the experimental study carried out by Akiyama *et al.* (1998) was chosen as to provide reference experimental data for this validation study.

4.2.1 RCM Experiment

Akiyama *et al.* (1998) investigated spray combustion characteristics using RCM with an injector. The purpose of the study is to examine possibility of reaching more homogeneous combustion by different injection strategies and different fuel blends. A schematic diagram

Initial Condition	
Initial Pressure	2.7 MPa
Initial Temperature	830K

Fuel Information	
Injection Amount	0.028 g
Fuel cetane number	55
Fuel	JIS 2 oil
Injection Duration	3.8ms

Injection Parameter	
Nozzle hole diameter	0.18 mm
Nozzle hole area	$0.025mm^2$
Nozzle opening pressure	20 MPa
Fuel injection pressure	80 MPa

Table 4.1: RCM and Injector Specification

of the RCM is shown in Figure 4.2. The RCM has compression stoke of 692mm with a compression ratio of 15.5. Quartz windows are installed in the cylinder head and piston such that visual observation and optical measurement of combustion event is possible.

In the original experimental work, a test matrix composed of different injectors and different fuel blends was used to study the effect of injector and fuel blends on the ignition delay and the combustion characteristics. Two injectors with regular nozzle hole size and fine hole size were used of different fuel blends with different cetane numbers. A baseline case utilized an injector with 0.18 mm nozzle hole diameter with JIS 2 gas oil, which has a cetane number of 55.

Shown in Figure 4.2 is a schematic diagram of the RCM at the end of the compression stroke. At this stage, the combustion chamber has a diameter of 145 mm and 48mm depth. An injector is located on the side wall of the chamber to inject fuel into the combustion chamber once the piston has reached the piston stop. It should be noted that the injection direction may appear different from a typical engine case where injection occurs from the center of the piston head. This setup was chosen such that the interaction between the wall and the spray can be minimized.

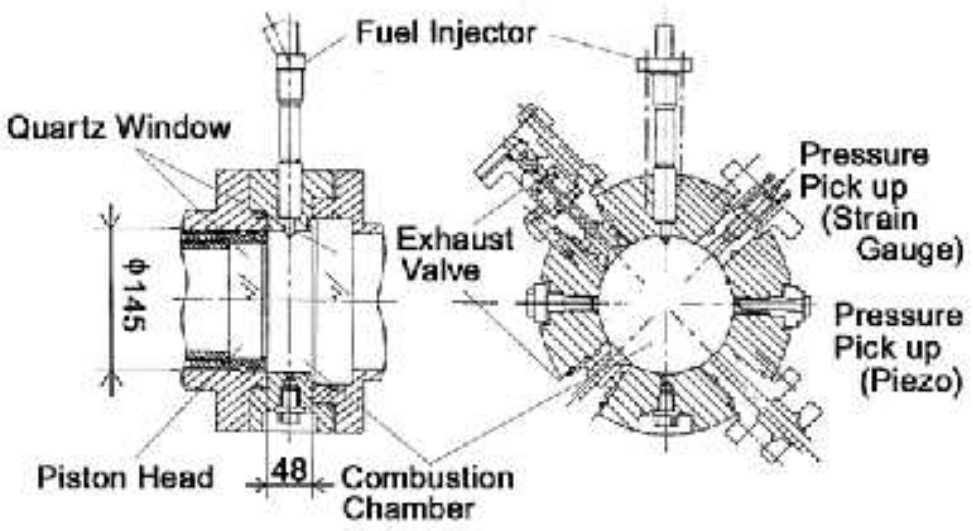

Figure 4.2: RCM: Experimental Setup from Akiyama *et al.* (1998)

4.2.2 Numerical Experiment

In the numerical experiment, only the compressed part with the piston positioned at the end position was simulated. Therefore, the pressure and the temperature in Table 4.1 are the initial pressure and temperature for the numerical simulation. Like the experiment, the chamber was assumed to be well insulated, such that there is no heat loss to the wall. A 3-D computational mesh was prepared as shown in Figure 4.3. The computational mesh has been refined such that it has more cells near the injector and along the spray.

In the experiment, the effect of fuel cetane number on ignition delay was examined by changing the fuel cetane number by mixing two different fuels, which are JIS 2 gas oil with cetane number 55 and α-methyl naphthalene with cetane number 0. In the baseline case, only JIS 2 gas oil was used. Due to lack of JIS 2 gas oil reaction chemistry, n-heptane was used as primary fuel in the numerical experiment with the reaction mechanism by Liu *et al.* (2004).

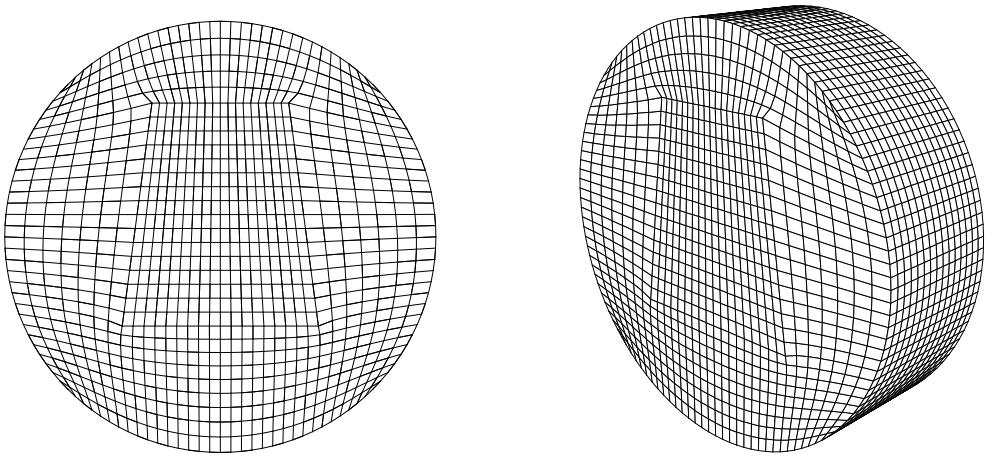

(a) Top View (b) Side View

Figure 4.3: A Computational Mesh for the RCM

4.2.3 Numerical Results

Pressure and temperature histories from the experiment and numerical simulations using both the RIF and the RIF-ER models are plotted in Figure 4.4. In Figure 4.4(a), three different pressure histories are shown including the experimental result of Akiyama *et al.* (1998) using a fuel with cetane number 55 along with two numerical results.

In this case the RIF model prediction is in good agreement with the experiment as shown in Figure 4.4(a). The ignition occurs around 2.4ms, where total injection duration is 3.8ms. The injection duration is also marked in Figure 4.4(a) and Figure 4.4(b).

The RIF-ER result also shows good agreement with the experimental data. Up to the end of the ignition delay, both the RIF and RIF-ER models predict similar results. However, pressure traces begin to deviate from each other as they reach the later part of the injection duration, as shown in Figure 4.4(a). After ignition, the RIF model predicts higher pressure and temperature than that of the RIF-ER model throughout injection and also following combustion.

Such difference in the pressure trace can be understood by considering the fuel addition effect. In the simulation, fuel is being added shortly after the simulation start to 3.8 ms. At its initial stage, the reaction space is at its mixing limit. Thus, addition of fuel does not

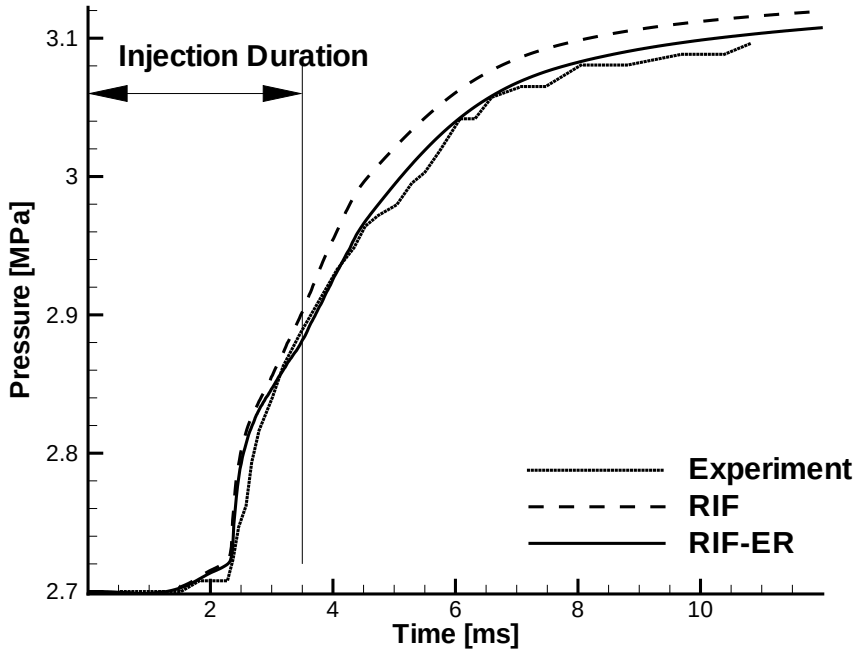

(a) RCM Pressure History

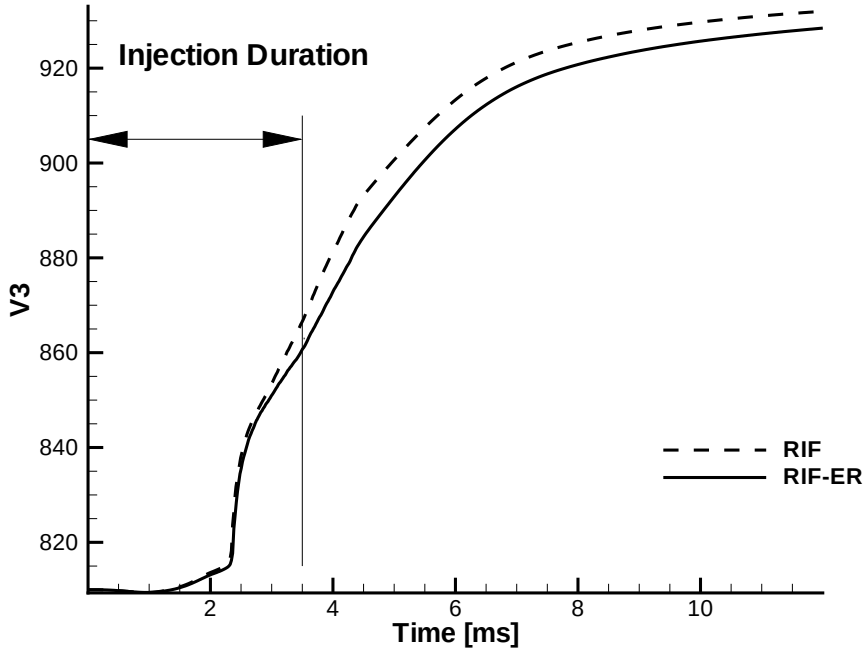

(b) RCM Temperature History

Figure 4.4: RCM Pressure and Temperature

significantly affect the reaction space during the first phase of fuel injection before ignition. After the ignition, the reaction space significantly deviates from its mixing limit, reflecting the reaction occurred during ignition.

As a result, fuel addition occurs over the partially reacted mixture in the later part of the injection duration. At this phase, the RIF and the RIF-ER models begins to deviate from each other, since the RIF-ER model updates the reaction space by considering fuel addition into the reaction space. Fuel added during the later part of the injection period is required to be broken down to smaller radicals by endothermic reactions. As a result, when fuel addition is updated as in the RIF-ER model, the pressure and temperature prediction become lower than that of the RIF model. From Figure 4.4 that RIF-ER model provides a better prediction of measured experimental data than the RIF model. Details of the reaction space at different time steps will be analyzed in Section 4.2.4.

In-cylinder luminosity images are compared in Figure 4.5 and Figure 4.6 for two time steps, 2.4 ms and 6.8 ms. These time steps were chosen to represent a time step of first observable luminosity and a time step for later combustion, respectively. An image taken in the experiment of Akiyama *et al.* (1998) is shown in Figure 4.5(a), and simulation results at similar time steps is shown in Figure 4.5(b), which shows reasonable agreement to the experimental data. In Figure 4.5(b), the RIF-ER may seem to predict higher temperature. However, this is due to the fact that RIF-ER predicts slightly faster ignition by a fraction of a millisecond.

Spatial temperature distribution at the later time step of 6.4 ms is shown in Figure 4.6. It can be observed from Figure 4.6(b) that the RIF-ER result shown on the far right side, predicts a larger width of the combustion region, which is in better agreement to the experimental data shown in Figure 4.6(a).

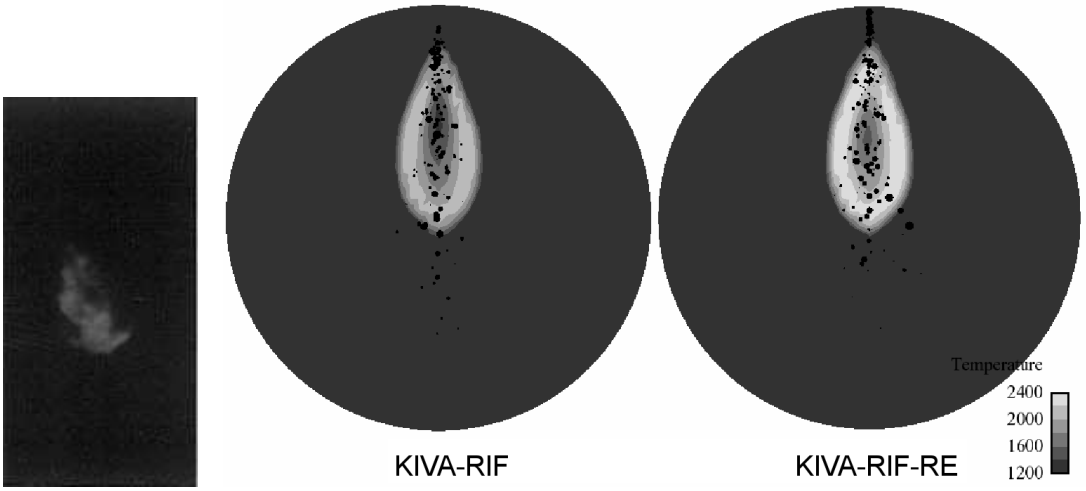

(a) Experimental Result (b) Numerical Result

Figure 4.5: In cylinder luminosity at t $\sim$ 2.4ms

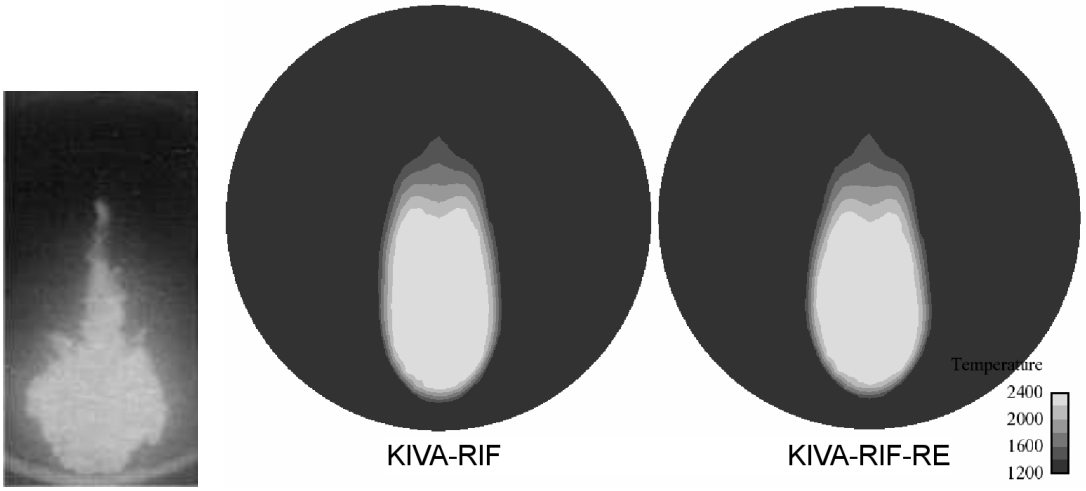

(a) Experimental Result (b) Numerical Result

Figure 4.6: In cylinder luminosity at t $\sim$ 6.4ms

4.2.4 Fuel Distribution in Physical and Reaction Spaces

Fuel distribution in the physical space and the reaction spaces at different time step will be examined. The fuel distribution in the space will be examined by fuel distributions along the spray and across the spray, as shown in Figure 4.7(b). For simplicity, fuel distribution across the spray was examined at a constant distance of 7.4 cm from the spray tip regardless of spray penetration depth. Fuel distribution along the spray was examined over a line shown in Figure 4.7(a).

Spatial fuel distributions and fuel species mass fraction profiles in the reaction space will be compared between the RIF model and the RIF-ER model for three different time steps. These three time steps will be chosen to be before ignition, during combustion following ignition, and at the end of significant pressure rise. Three different time steps of 1.643ms, 2.443ms and 4.676ms are chosen for comparison. These time steps are shown in Figure 4.8 over a pressure history plot.

Fuel Distribution Before Ignition: t=1.643ms

First, spatial fuel distributions and fuel in the reaction space at t=1.634ms will be examined. This time step is chosen to represent a case before ignition. The spatial fuel distributions are shown in Figure 4.9. The RIF results are shown in dashed lines, while the RIF-ER results are shown in solid lines. From the overall pressure trace shown in Figure 4.4, it is clearly shown that the pressure has not risen by a significant amount at this time step of t=1.634ms. However, the spatial fuel distribution shown in Figure 4.9 shows deviation between the RIF and RIF-ER results. The fuel species distribution along the spray axial distance shown in Figure 4.9(a) shows that the RIF-ER predicts lower amount of fuel distribution than the RIF model near the spray nozzle. This trend is reversed near the spray tip, where the RIF model predicts lower amount of fuel than the RIF-ER model.

The location where the radial distribution shown in Figure 4.9(b) is evaluated is marked by an arrow in Figure 4.9(a), which is closer to the spray tip. The radial fuel distribution

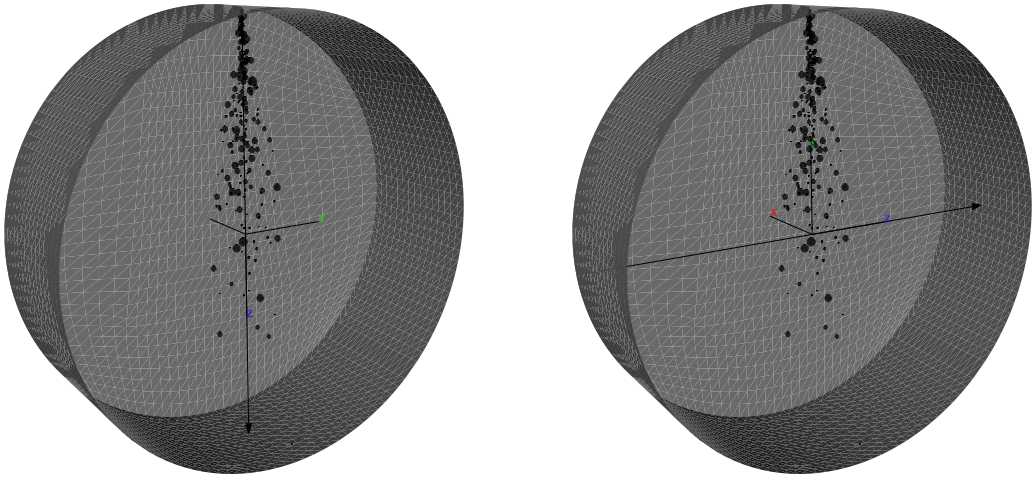

(a) One-D line along the spray: Radial distance (b) One-D line across the spray: Spray axial distance

Figure 4.7: One-D lines for Fuel Distribution Comparison in Rapid Compression Machine Numerical Experiments

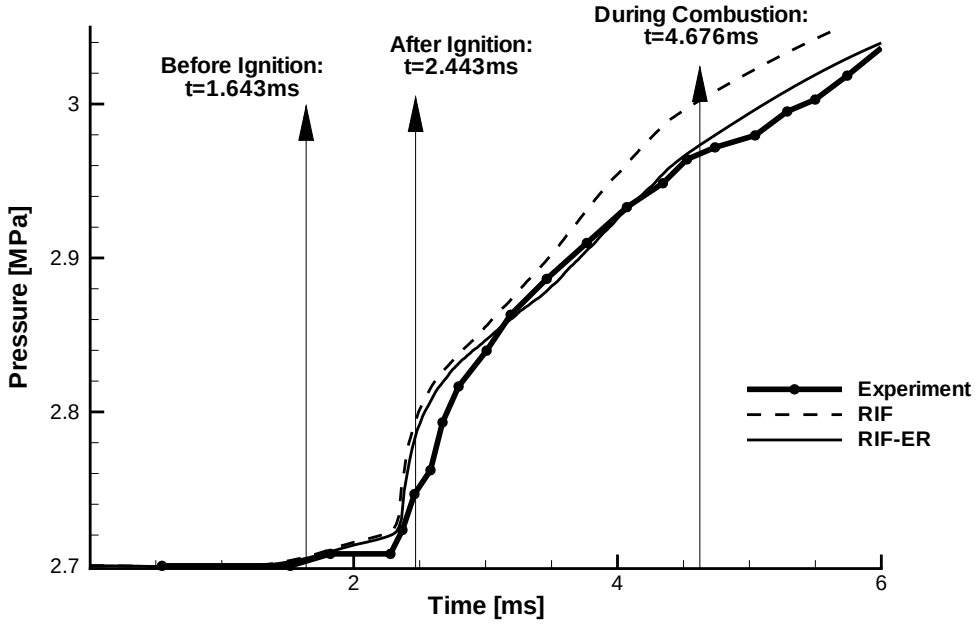

Figure 4.8: Time steps Examined to Compare Spatial Fuel Distributions in RCM Numerical Experiments

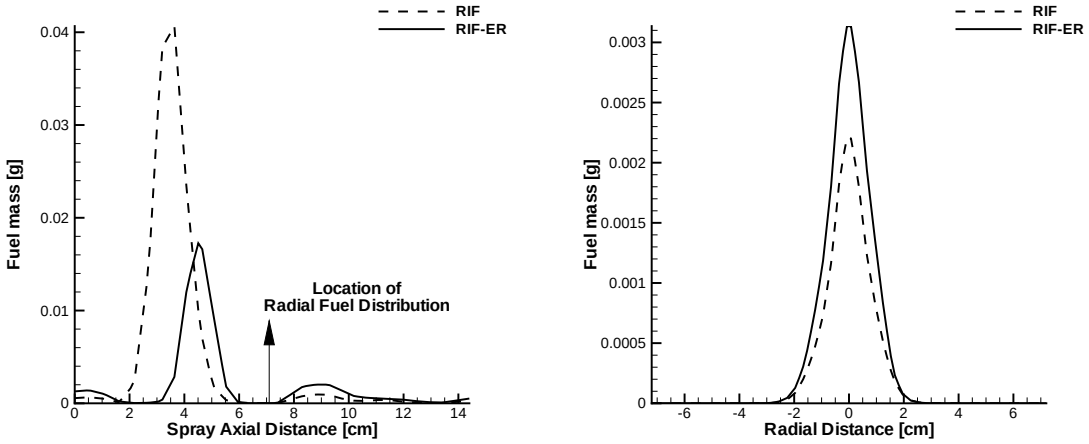

(a) Fuel distribution along the spray (b) Fuel distribution across the spray

Figure 4.9: Spatial Fuel Distribution at t=1.643ms

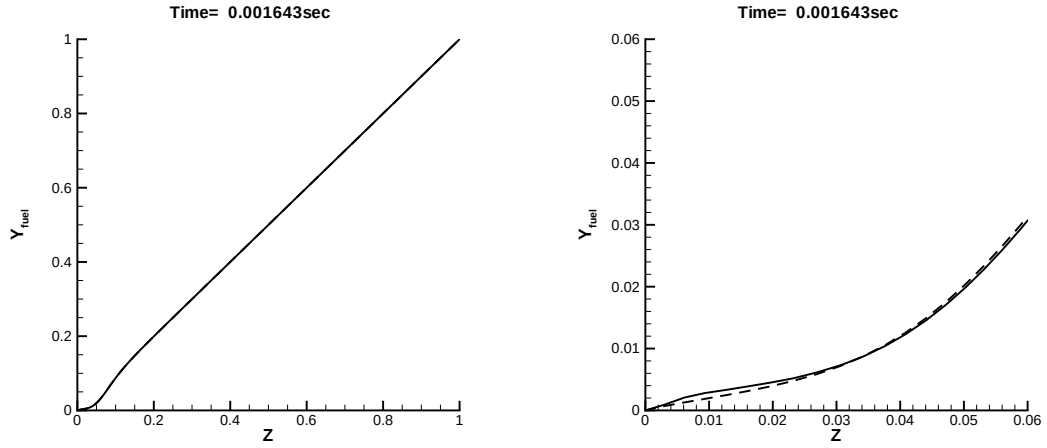

(a) Fuel species profile: entire Z range (b) Fuel species profile: lean Z range

Figure 4.10: Fuel species profile in the Reaction Space at t=1.643ms

shown in Figure 4.9(b) shows that the RIF-ER model predicts more fuel near the tip of the spray.

The fuel distribution at the given time step is shown in Figure 4.10, with the RIF model in dashed lines and the RIF-ER model in solid lines. The fuel mass fraction distribution for the entire Z range is shown in Figure 4.10(a). From the fuel mass distribution, it is clear that both reaction and vaporization are occurring at the given time step. There are small amounts of fuel reduction in the lean side. Overall, the fuel mass fraction distribution from the RIF and the RIF-ER models seems to be similar in macroscopic view. An enlarged figure for the lean Z range is presented in Figure 4.10(b).

From Figure 4.10(b), it is found that the change in fuel amount predicted by the RIF-ER model is observed in the fuel lean range. The maximum $\tilde{Z}$ value in the physical space is yet up to 0.015, and the effect of vaporization is mainly up to a similar range. As a result, the fuel amount in the RIF-ER model becomes larger, reflecting the effect of vaporization in the physical space. The difference in fuel distribution in the physical space shown in Figure 4.9 can be understood by the change in fuel mass fraction in the reaction space.

Fuel Distribution After Ignition: t=2.443ms

Similar plots to Figure 4.11 is shown in Figure 4.11. From Figure 4.11(a), it is observed that both the RIF and the RIF-ER models predict high fuel consumption near the nozzle exit near $x = 0$. However, the fuel distribution along the spray is significantly different from the RIF and the RIF-ER models.

At the given time step, predictions on $\tilde{Z}$ field become different from each model. As a result, the fuel amount should be considered along with $\tilde{Z}$ distribution, which is shown in Figure 4.12. From Figure 4.12(a), it is observed that RIF estimates higher $\tilde{Z}$ values than RIF-ER from the nozzle exit up to 4cm in the spray axial distance. Also, there is difference in estimated $\widetilde{Z''^2}$ values. The higher amount of fuel in the RIF result along the axial direction from the nozzle exit up to 4cm downstream is expected to produce

differences in $\tilde{Z}$ and $\widetilde{Z''^2}$ as vaporization effect is accumulated over time.

A more interesting result can be observed in Figure 4.11(b), which shows the radial distribution of fuel mass across the spray. Spatial temperature distributions at this time from the RIF and the RIF-ER models are shown in Figure 4.13.

As observed in Figure 4.13, there exist droplets on the periphery of the spray near the cutline, and vaporization should be occurring near the periphery, where the temperature is close to 2300 K. As observed in Figure 4.11(b), the RIF-ER model predicts higher fuel content in this case, reflecting the effect of fuel droplet vaporization and subsequent fuel addition, while the RIF model only considers the reaction. One interesting observation from Figure 4.13 is that the width of the high temperature region is wider in the RIF-ER prediction than that of the RIF prediction as mentioned before, which is more similar to the experimental observation.

The fuel species mass fraction in the reaction space is shown in Figure 4.14, where lean and rich sides are shown separately in Figure 4.14(a) and Figure 4.14(b). It is being observed that the RIF-ER model predicts higher fuel concentration in the lean mixture fraction range, as shown in Figure 4.14(a). An additional plot for the mixture fraction in the rich range is shown in Figure 4.14(b). As mentioned in Section 3.3.3, the effect of vaporization in the rich region is reflected by reducing the fuel amount in the rich region. This trend is well shown in Figure 4.14(b). By comparing Figure 4.14(a) and Figure 4.14(b), different effects of vaporization on the reaction space in the lean and the rich regions are successfully identified and visualized.

Fuel Distribution After EOI: t=4.676ms

Now, we will examine how the accumulated effect of vaporization affects the spatial temperature and pressure field even after the end of fuel injection and droplet vaporization. First, the fuel species mass fraction in the reaction space is shown in Figure 4.15.

It should be noted that the y axis scale has been adjusted to reflect fuel consumption

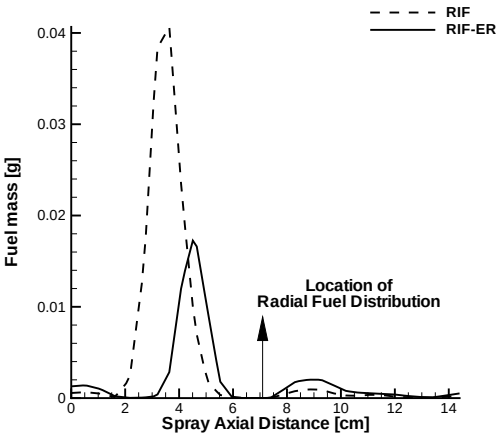

(a) Fuel distribution along the spray

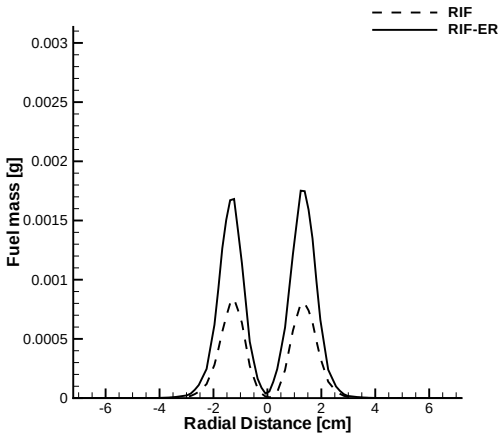

(b) Fuel distribution across the spray

Figure 4.11: Spatial Fuel Distribution at t=2.443ms

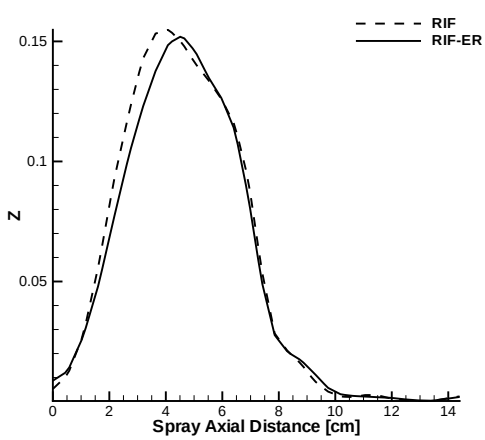

(a) $\tilde{Z}$ distribution along the spray

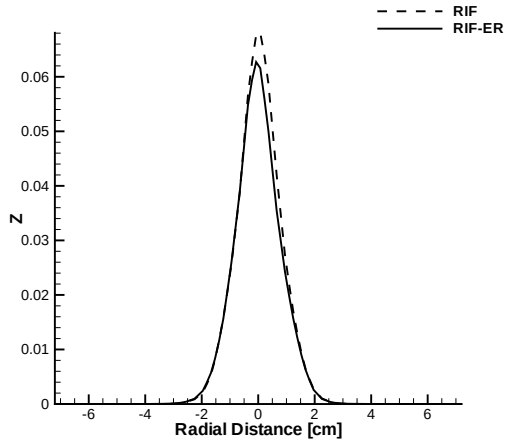

(b) $\tilde{Z}$ distribution across the spray

Figure 4.12: Spatial $\tilde{Z}$ Distribution at t=2.443ms

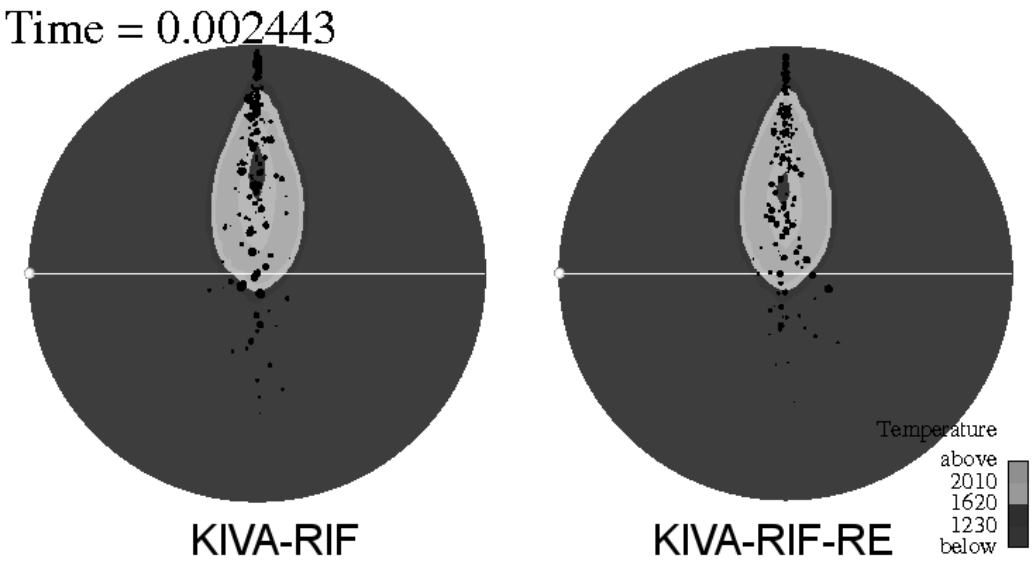

Figure 4.13: Spatial Temperature Distribution at t=2.443ms

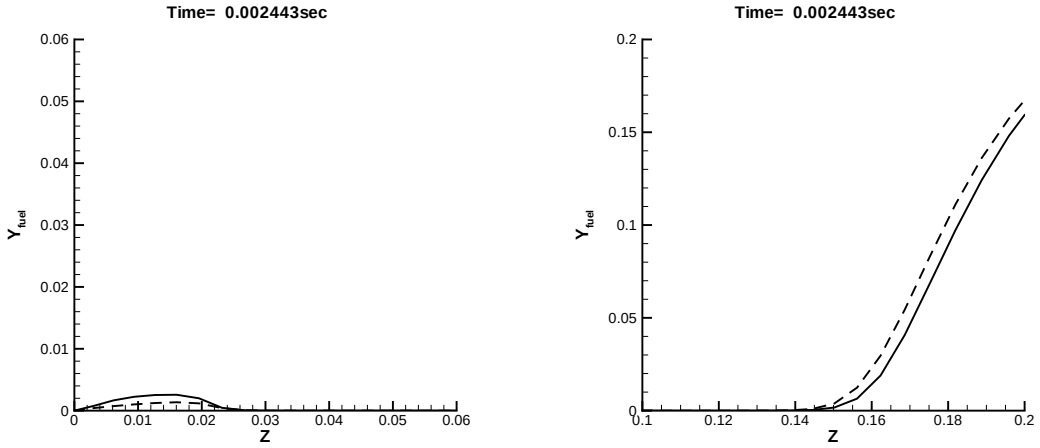

(a) Fuel species profile: lean Z range

(b) Fuel species profile: rich Z range

Figure 4.14: Fuel species profile in the Reaction Space at t=2.443ms

and hence the very small amount of left-over fuel. At this time step, the last droplet has already been vaporized, such that there is no fuel addition occurring at the given time step. However, the effect of previous fuel vaporization is still in effect, such that the radial fuel distribution from the RIF-ER shows still higher fuel concentration on the periphery of the spray where vaporization occurred.

The fuel mass fraction in the reaction space at the current time step is shown in Figure 4.16. At this stage, the high temperature combustion is dominant, such that fuel distributions in high Z range become similar between the two models. At the lower limit, the RIF-ER model still predicts higher fuel concentration at very low Z range.

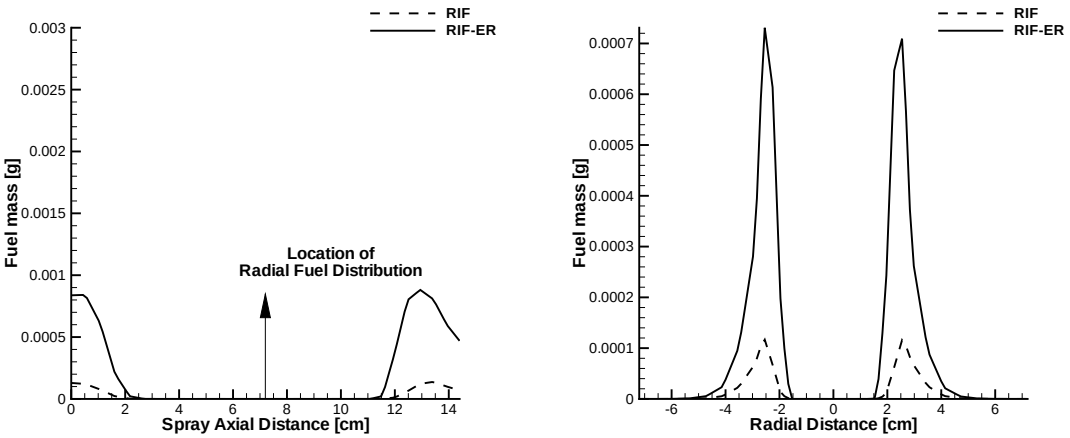

(a) Fuel distribution along the spray (b) Fuel distribution across the spray

Figure 4.15: Spatial Fuel Distribution at t=4.676ms

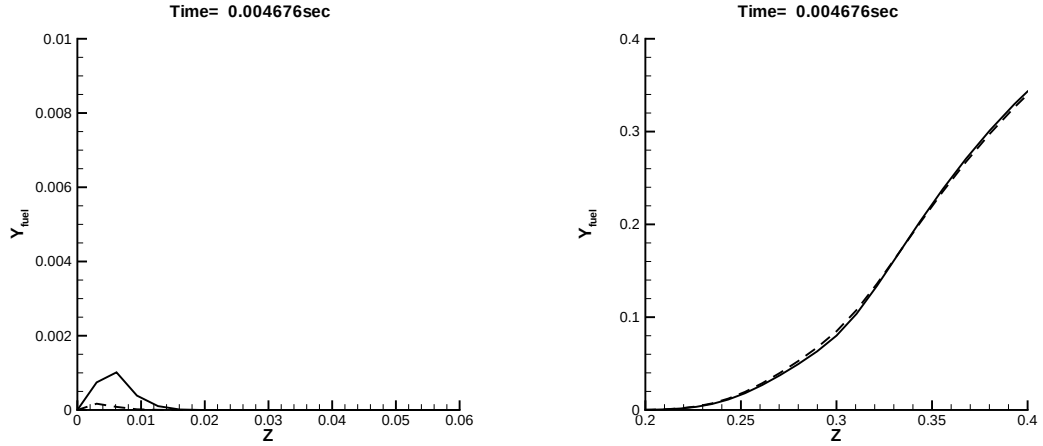

(a) Fuel species profile: lean Z range (b) Fuel species profile: rich Z range

Figure 4.16: Fuel species profile in the Reaction Space at t=4.676ms

4.3 Validation Against Diesel Engine Experiment

In the previous section, a validation study against the RIF-ER model has been tried against the Rapid Compression Machine experiment of Akiyama *et al.* (1998). In this section, a validation study will be tried against a diesel engine experiment, chosen from the EDC model validation study of Hong *et al.* (2008).

4.3.1 Numerical Setup

In Hong *et al.* (2008), the EDC model was validated against diesel engine experiments over a wide range of operating conditions including EGR, equivalence ratio and fuel injection timing. In this study, two cases of Hong *et al.* (2008) were chosen to examine the RIF-ER model performance for different injection timings. The engine geometry and operating conditions are listed in Table 4.2. Two cases with different injection timings with Start of Injection timing (SOI) at -11.1° CA bTDC and -3.4° CA bTDC were examined. The computational mesh is shown in Figure 4.17. A detailed n-heptane reaction mechanism suggested by Liu *et al.* (2004) was used to model the detailed chemistry in conjunction with a detailed NO_x mechanism by Liu *et al.* (2006), which considers prompt NO formation along with thermal NO formation.

Bore	9.5 cm
Stroke	10.5 cm
Squish	0.165 cm
Compression Ratio	18:1

RPM	1500
m_{inj}	30 mg
IVC	-133 aTDC
EVO	122 aTDC

Table 4.2: Engine Geometry and Operating Conditions

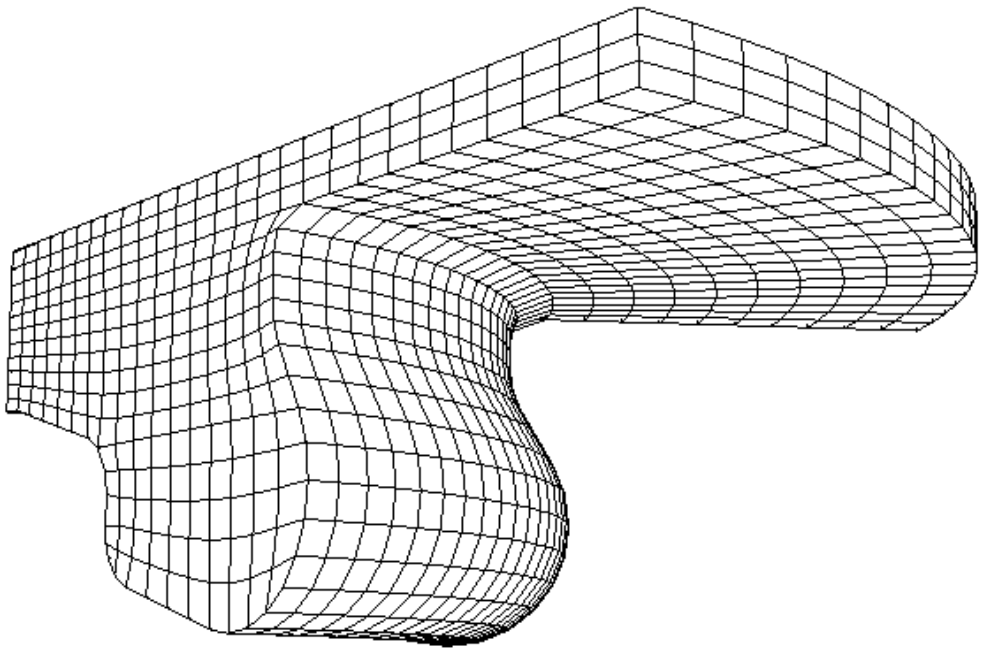

Figure 4.17: Computational Mesh of the Diesel Engine

4.3.2 Results

Case 1: SOI -11.1° CA bTDC

The pressure traces are compared in Figure 4.18 and Figure 4.19. In addition to the RIF and RIF-ER model results, the EDC model prediction will be also considered for the comparison, as well. The EDC model results are plotted with a short dash. It can be shown from Figure 4.19 that the EDC model predicts a gradual pressure increase during ignition. Also ignition is predicted at an earlier crank angle from the EDC model. Such prediction is consistent with the EDC model assumptions, where the transition from ignition to combustion is modeled with a model constant which should be calibrated against experimental data.

Both the RIF and RIF-ER models predict similar pressure traces in Figure 4.18. The results show better prediction than the EDC model, i.e. closer to the experimental results shown with solid lines. In this particular case, the RIF and RIF-ER models do not exhibit

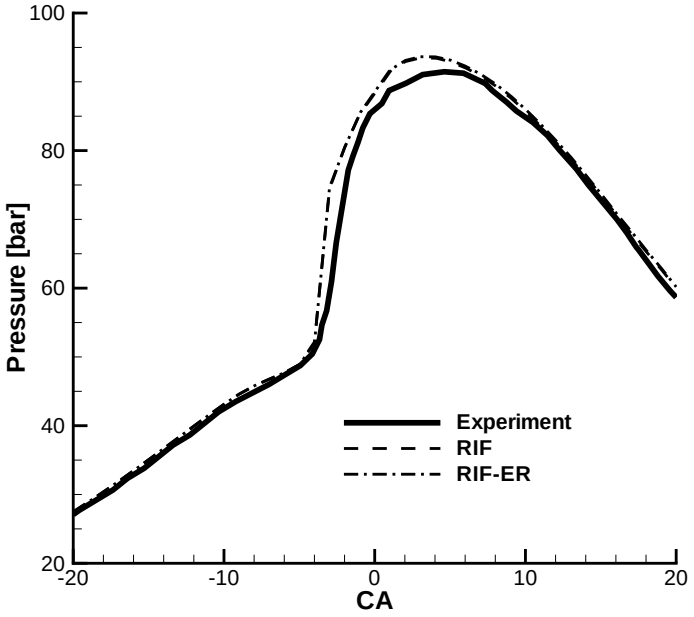

Figure 4.18: Diesel Engine Pressure Comparison with RIF and RIF-ER model: Case 1

significant difference in pressure histories.

A detailed comparison of pressure traces near TDC, shown in Figure 4.20, reveals a similar trend to the RCM experiment in pressure histories. The RIF model predicts higher pressure at combustion than that of the RIF-ER model. Even though the difference in the pressure may not be significant, it would result in a difference in the emissions trends, which are controlled by local temperatures.

The NO predictions are compared in Figure 4.21. The NO results shows that the RIF model predicts more than 200% NO emissions than measurements. It should be noted here that it has been reported that the RIF model provides excellent NO emissions prediction (Hergart & Peters, 2002; Pitsch & Peters, 1998; Pitsch *et al.* , 1996) under diesel engine operating conditions. However, the injection parameters were also calibrated in these cases (Weber & Peters, 2006). In the current case, the injection parameters were not calibrated. Moreover, the detailed mechanisms applied are different between the references and the current study, which may contribute to the increased NO formation from the RIF modeling

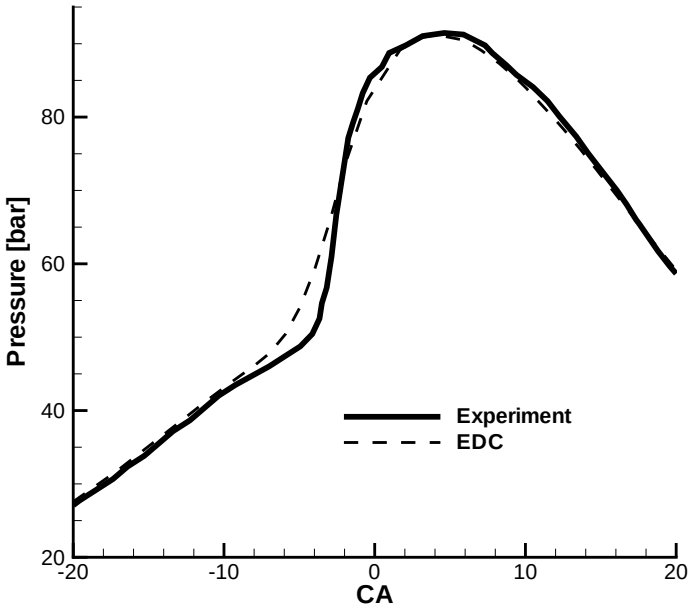

Figure 4.19: Diesel Engine Pressure Comparison with EDC model: Case 1

as shown in Figure 4.21.

In the current study, the RIF-ER model predicts an NO level which is similar to the NO level determined from the experiment. The decreased NO level from the RIF-ER model can be interpreted to be a result of the slower reaction progress estimated in the RIF-ER model than the RIF model. The NO esitmate from the EDC model, which is known to underpredict NO as reported in Hong *et al.* (2008), is also shown in Figure 4.21 for comparison. A pressure trace comparison between the EDC result and the experimental result is shown in Figure 4.22. The EDC model predicts a gradual pressure rise during ignition. Such gradual pressure rise can be attributed to the calibrated transition parameter used in the EDC model which determines the transition from ignition to combustion.

Case 2: SOI -3.4° CA bTDC

The pressure traces are compared for the SOI -3.4° CA bTDC case in Figure 4.23. The RIF predicts higher pressure than that of the RIF-ER model. This can be interpreted as the

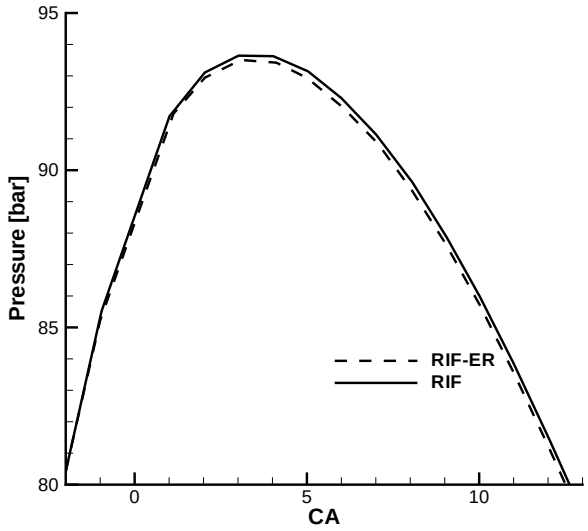

Figure 4.20: Diesel Engine Pressure Comparison with RIF and RIF-ER models: Case 1

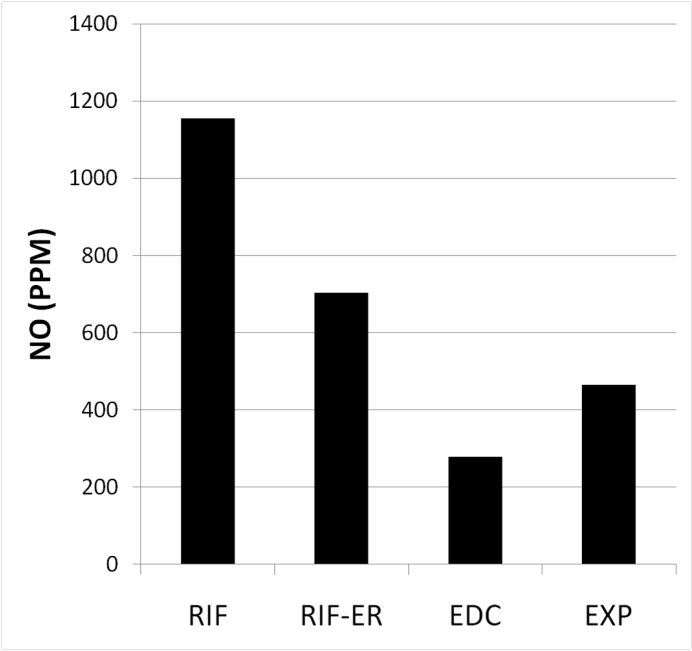

Figure 4.21: NO emissions comparison: Case 1

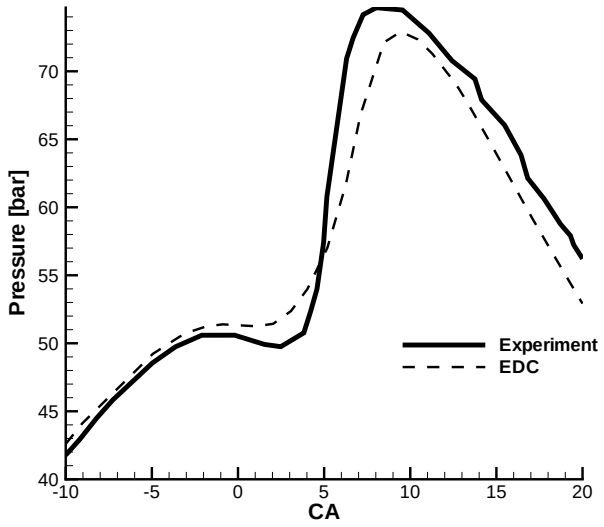

Figure 4.22: Diesel Engine Pressure Comparison with EDC model: Case 2

effect of droplet vaporization ,which is correctly represented in the reaction space by the RIF-ER model. As a result, the progress in reaction is retarded compared to the RIF model to result in smaller pressure at combustion.

The NO emission comparison is shown in Figure 4.24. A similar trend with Figure 4.21 is observed, such that the NO emission is heavily overpredicted by the RIF model, while the RIF-ER model prediction is closer to the experimental result. Comparison with the EDC model, also shown in the same figure, indicates that it underpredicts the NO emission in the -11.1° CA case.

4.4 Summary

The proposed numerical mode RIF-ER, has been validated in this Chapter.

A validation against spray combustion was first performed using the RCM experiment by Akiyama *et al.* (1998). The results showed that the RIF model itself produces satisfactory results. At the same time, the suggested model was able to improve predictions to better match the experimental data. Detailed analysis on the fuel distribution in both the

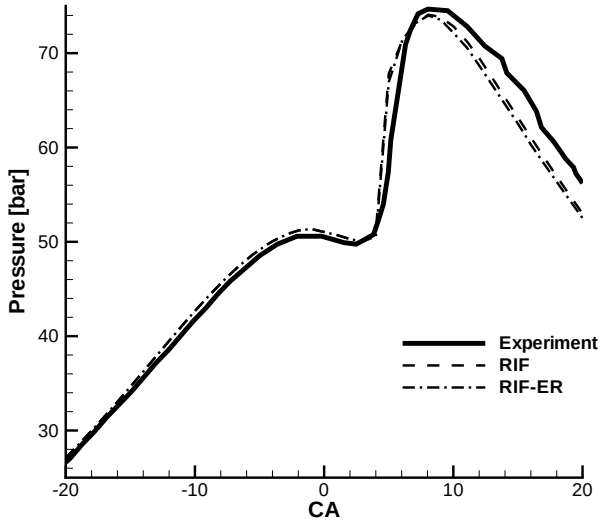

Figure 4.23: Diesel Engine Pressure Comparison with RIF and RIF-ER models: Case 2

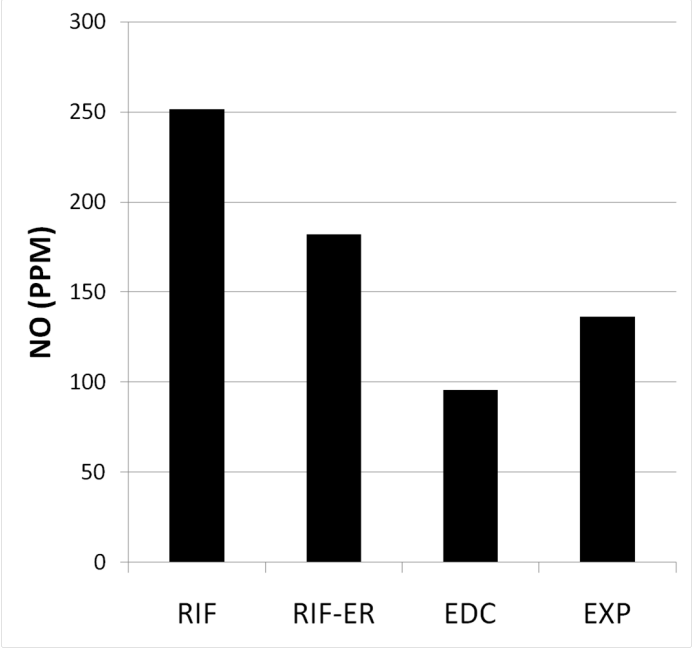

Figure 4.24: NO emissions comparison: Case 2

reaction and the physical spaces were carried out to examine differences between the RIF and the RIF-ER model results. It was found that in general, the RIF-ER model predicts larger fuel concentrations by considering the effect of vaporization. This can be interpreted as a reduction in the reaction progress, which will result in lower temperature and pressure in the physical space than the RIF model prediction.

The RIF-ER model has been also validated against conventional diesel engine experimental data. It was found that the RIF-ER model prediction is in a very good agreement with the experiment, mainly due to the solid physics modeling of the flamelet-based approach. Comparison between the RIF and RIF-ER model showed that the RIF-ER model predicts slightly lower pressure and temperature than the RIF model. This is in good agreement with the previous observation made in the validation using the rapid compression machine. Comparison of NO emission between the RIF and the RIF-ER models revealed that the RIF-ER model prediction is in good agreement with the experimental observation, while the RIF model predicts higher amount of NO. This can be explained by the reduction in the reaction progress in the reaction space predicted by the RIF-ER model, which will lower local pressure and temperature and hence lower NO formation.

Along with comparison between the RIF and the RIF-ER models, the EDC model was also considered in the diesel engine modeling. It was found that the EDC model predicts gradual pressure rise during ignition, which is different from the experimental observation. Also, the EDC model predicts lower NO formation than the models based on the flamelet approach.

Regarding computing resources, the EDC model required 71 hours on a 2.4GHz Opteron processor. In contrast, both models based on the flamelet approach (RIF and RIF-ER) required only 6 to 8 hours of computing time, which is a significant reduction in computing resources.

Chapter 5

Application of RIF-ER model to PPCI Combustion

5.1 Introduction to HCCI/PPCI Combustion

Homogeneous charge compression ignition (HCCI) engines have been studied extensively as an alternative combustion concept (Thring, 1989; Najt & Foster, 1983). In HCCI engines, a lean mixture of fuel and air enters the combustion chamber to auto-ignite as in conventional diesel engines. Due to its low equivalence ratio, the combustion temperature is relatively low, which results in low NOx emissions. Simultaneously, soot is reduced compared to diesel combustion due to the lean homogeneous mixture. Such reduction in major emission species makes the HCCI concept attractive with the advent of more stringent emissions standards.

Despite these advantages, however, HCCI engines have a few challenges to overcome for practical implementation. First, combustion in HCCI engines relies solely on the auto-ignition of the in-cylinder mixture, such that limited control measures are available. Consequently, the range of operating conditions is limited: at high load condition, most of the in-cylinder mixture burns simultaneously, causing an excessively rapid pressure rise which is commonly referred to as knock. At low load conditions, on the other hand, HCCI engines suffer from misfire as the mixture becomes too lean to auto-ignite. A typical HCCI operating range in terms of engine speed and load conditions is shown in Figure 5.1 (Zhao *et al.* , 2002).

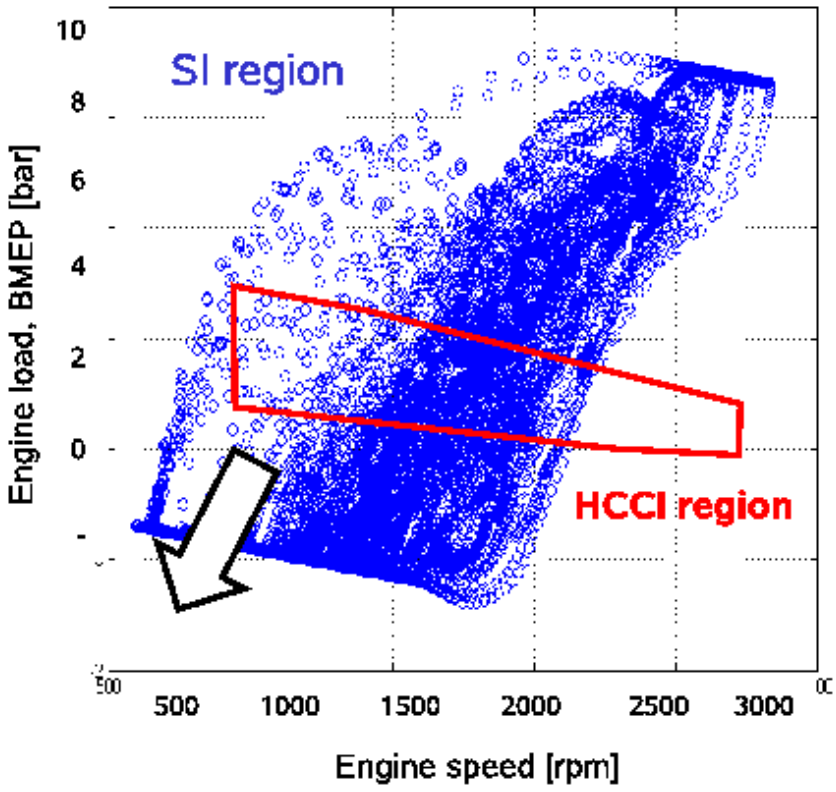

Figure 5.1: HCCI operating range (Zhao *et al.* , 2002)

Attempts have been made to extend the operating range of HCCI engines. One of the most common methods for the low-load operating range extension is a stratification strategy (Brewster *et al.* , 2008; Dec & Sjöberg, 2003; Hwang *et al.* , 2007). At the low-load limit, stratification of the in-cylinder mixture allows locally rich region where the mixture is ignitable, while maintaining low overall equivalence ratio. To implement such stratification, a direct injection strategy is typically applied at an early stage before combustion. An early injection should be controlled so as to provide sufficient time for the fuel to vaporize and mix with the air, but without reaching complete homogeneity before combustion. This type of early injection strategy allows stable combustion at low-load conditions by ignition at locally rich region (Dec & Sjöberg, 2003). This combustion mode is referred to as the partially premixed compression ignition (PPCI). Extensive experimental work can be found

on the stratification effect in the PPCI mode of combustion (Berntsson & Denbratt, 2007; Brewster *et al.* , 2008; Hwang *et al.* , 2007).

5.2 Numerical Modeling of HCCI/PPCI Combustion

In HCCI combustion, the fuel and the oxidizer are well mixed before significant reaction occurs. Combustion is initiated by auto-ignition by compression, which occurs simultaneously in different *hot zones* in the combustion chamber. As a result, it has been assumed that HCCI combustion is more like combustion in a Perfectly Stirred Reactor, where no visible flame exists to conclude that HCCI combustion is purely chemistry controlled as suggested by Najt & Foster (1983). This assumption has been a fundamental basis on developing combustion models for HCCI combustion.

The simplest modeling approach is zero-dimensional as reported by Christensen *et al.* (1999); Dec (2002). The zero-dimensional model is capable of reporting quantitative estimate of engine operations. Also it is very cheap in terms of computational resources. However, it lacks consideration on detailed engine geometry, stratification, wall heat transfer and gas exchange process to result in shortcomings in the heat release rate and emissions predictions.

Numerical efforts have been made to model HCCI combustion using multi-dimensional CFD codes. Since separation of chemistry and turbulence is assumed, implementation of HCCI combustion model usually does not require a chemistry-turbulence model. As a result, no sub-grid turbulent combustion model has been used, such that the chemistry can be evaluated at each cell by purely chemical consideration. However, this approach is still computationally expensive when a large number of reactant species is used. To reduce the amount of computational time required for evaluating chemistry at each computational cell, a multi-zone model has been suggested by Aceves *et al.* (2000). In the multi-zone model, species information in computational cells are grouped into a number of bins parameterized

by a single parameter. The reaction is considered in each bin, instead of computational cells. The total number of bins is usually much smaller than the number of computational cells, such that a huge reduction in the computational resource is possible while maintaining good accuracy. The model has been improved by Flowers *et al.* (2003) to consider the mixing effect in the multi-zone model. Babajimopoulos *et al.* (2005) further improved the KIVA modeling framework by fully-coupling detailed chemistry in multiple zones with the fluid solver successfully model HCCI combustion.

Application of the flamelet approach to the HCCI combustion modeling has been also researched by a number of researchers. Cook & Peters (2005) suggested a novel approach for applying the flamelet approach to HCCI combustion. In an HCCI engine, the mixture is close to its homogeneous limit. As a result, $\tilde{Z}$ is almost constant, and may not require to represent thermal stratification in the physical space. Instead, enthalpy was suggested as a conserved scalar variable to capture the effect of thermal inhomogeneity in HCCI engine and combustion. Most recently, Hergart & Peters (2002) and Hergart *et al.* (2005) suggested application of the conventional RIF approach to model HCCI/PPCI combustion. In their papers, similarities between the RIF model and the multi-zone model were identified such that both models should result in similar predictions of HCCI engine combustion.

In contrast, relatively limited efforts have been made on PPCI modeling, although CFD simulation may provide detailed information about the in-cylinder process and the effect of stratification. This is mainly due to the difficulties in describing the combustion characteristics in PPCI engines as compared to those in HCCI engines.

In PPCI engines, however, the presence of in-cylinder fuel injection makes it difficult to justify the validity of the multizone type homogeneous reactor model, requiring more accurate description of the effects of turbulent transport on combustion. This has been successfully achieved by the flamelet approach (Peters, 2000), which postulates that chemical reactions take place in flame-like conditions such that they can be described in a reduced-dimension reactive space, commonly using a conserved scalar variable such as the mixture

fraction (Z).

The existing form of the flamelet approach, specifically the RIF model, has limitations when applied to PPCI combustion problems. In particular, the effect of the additional fuel vapor due to droplet evaporation has not been properly taken into account in the reactive space. The present study proposes an improved combustion model based on the RIF model, which accounts for the spray evaporation in both physical and mixture fraction spaces. The model is then applied to test simulations and validated against experimental data. Details of combustion characteristics are also examined by the spatial distribution of key solution variables for various injection timings.

5.3 RIF-ER model under HCCI conditions: Comparison with KMZ model

The RIF-ER model has been successfully validated in direct injection cases in Section 4.2. In this section, performance of the suggested model under close to HCCI conditions will be examined by comparing the result against the well-known and widely used KIVA-Multi Zone model of Babajimopoulos *et al.* (2005). The KIVA-Multi Zone model, or KMZ model, has been suggested by (Babajimopoulos *et al.* , 2005) as an extension of the multi-zone model of Aceves *et al.* (2000). The KMZ model utilizes two thermodynamic properties, temperature (T) and global equivalence ratio (Φ), to identify and group computational cells with similar reaction history. Then these cells are grouped into a number of bins based on T and Φ. Chemistry is solved for each bin, rather than each computational cell. As a result, it is capable to reduce the computational cost related to the evaluation of chemistry source terms. The model has been successfully validated and used extensively in a number of HCCI related research studies(Hessel *et al.* , 2008; Flowers *et al.* , 2006; Babajimopoulos *et al.* , 2005, 2002). In this section, a very early injection case in a gasoline HCCI engine will be simulated by both the RIF-ER model and the KMZ model. The results will

be compared to examine the performance of the RIF-ER model under near-homogenous conditions.

Similarities between multi-zone based models and the flamelet approach have been discussed by Hergart *et al.* (2005). To facilitate discussion, the governing equations in the reaction space from both models are shown below. For simplicity, the conventional reaction equation without vaporization source terms is shown from the RIF model.

$$\text{Multi-zone} \qquad \frac{\partial \rho_i}{\partial t} = \dot{\omega} \tag{5.1}$$

$$\text{Flamelet approach} \qquad \frac{\partial \rho_i}{\partial t} = \rho \frac{\chi}{2} \frac{\partial^2 Y_i}{\partial t^2} + \dot{\omega} \tag{5.2}$$

The similarities between (5.1) and (5.2) are obvious. The only difference is the existence of second order derivative in (5.2), which is multiplied by χ. From its definition, χ is proportional to the gradient of Z. Near the homogeneous limit, Z becomes homogeneous such that ∇Z becomes negligible. At this limit, the effect of the second order derivative term becomes negligible, and one may expect a similar result in (5.1) and (5.2).

However, there are several factors which may result in different predictions by these two models. First, the initialization and reaction history treatments are different. In KMZ, the reaction space is initialized at *each time step* based on CFD results. However, the reaction space in RIF and RIF-ER models carry their own reaction history over the time once initialized. The other difference between the two models is the *zoning principle*, which utilizes both temperature and global equivalence ratio Φ in KMZ, while RIF-ER utilizes only Z.

5.3.1 Numerical Setup

The early injection case of Dec & Sjöberg (2003) was chosen for comparison between the two models. In Dec & Sjöberg (2003), a thorough investigation on the effect of various parameters, including SOI timing, on the combustion was carried out. These results will

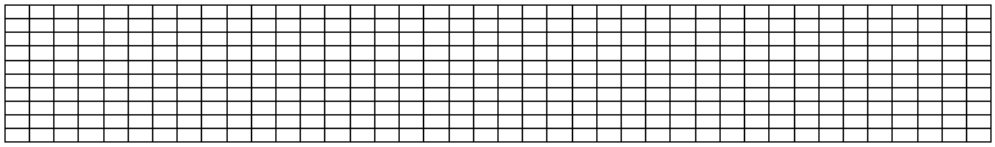

Figure 5.2: Computational mesh for preliminary comparison between RIF-ER model and KMZ model

be discussed in Section 5.4 and the RIF-ER model will be applied to reproduce some of important findings from Dec & Sjöberg (2003). Details of experimental and numerical setup will be visited in Section 5.4. In this section an early injection case of SOI 120° CA will be chosen and examined using two different models.

As a preliminary test, a highly simplified two dimensional mesh has been prepared for comparison purpose as shown in Figure 5.2. Details of engine geometry data will be discussed in the actual parametric study in Table 5.1 of Section 5.4.1. The fuel species used in the numerical experiment was iso-octane, modeled by a reaction mechanism suggested by Tanaka *et al.* (2003).

5.3.2 Results

The pressure and temperature history for the given case of SOI 120° CA is shown in Figure 5.3. The RIF-ER model results are plotted in solid lines, while the KMZ results are plotted in dashed lines. From Figure 5.3, it is clearly observed that the RIF-ER model prediction matches well with the KMZ model. Comparison of spatial temperature evolution over different crank angles near TDC is shown in Figure 5.4. Three crank angle degrees of 340, 360 (TDC) and 370° were chosen to compare the spatial temperature field evolution predicted by two models. From Figure 5.4, it is clearly shown that both the RIF-ER and KMZ predict similar temperature distribution near TDC.

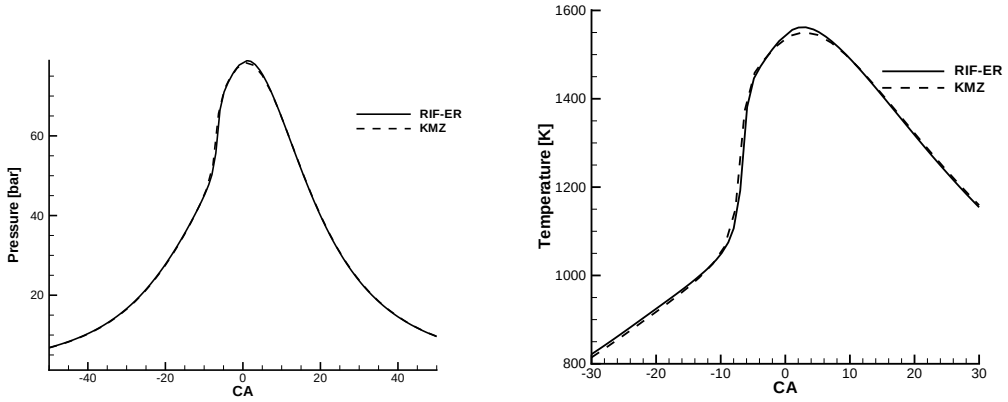

(a) Pressure Comparison (b) Temperature Comparison

Figure 5.3: Comparison of RIF-ER and KMZ models at Near-HCCI Condition of SOI 120° Case.

Before reaching TDC, at 340° CA, both KMZ and RIF-ER predict almost identical temperature distribution, as shown in Figure 5.4(a). As ignition and combustion occurs at TDC as shown in Figure 5.4(b), KMZ predicts two ignition regions, one near the cylinder axis and the other located at an outer radius. The RIF-ER model prediction is similar with small difference near the cylinder axis. Similar trend is carried until after the TDC as shown in Figure 5.4(c). The difference between the RIF-ER and the KMZ model can be attributed to different *zoning* principle. While KMZ utilizes both temperature and global equivalence ratio Φ to consider reaction in the reaction space, the RIF-ER only utilizes Z, which is equivalent to Φ, to consider reaction in the reaction space. As a result, the RIF-ER model has coarser resolution which results in differences in the local temperature near TDC as shown in Figure 5.4.

5.3.3 Discussion

Performance of the RIF-ER model under close to HCCI condition was examined and compared to the widely used KMZ model in this section. It was found that KMZ and RIF-ER predict almost identical pressure and temperature histories under a very early injection

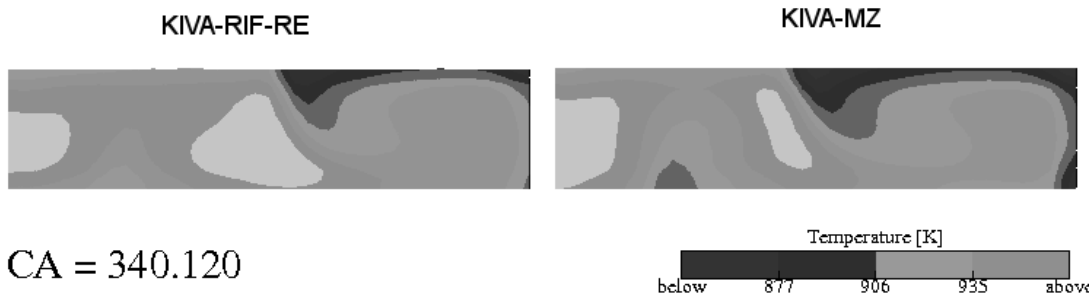

(a) Spatial Temperature Distribution at 340° CA

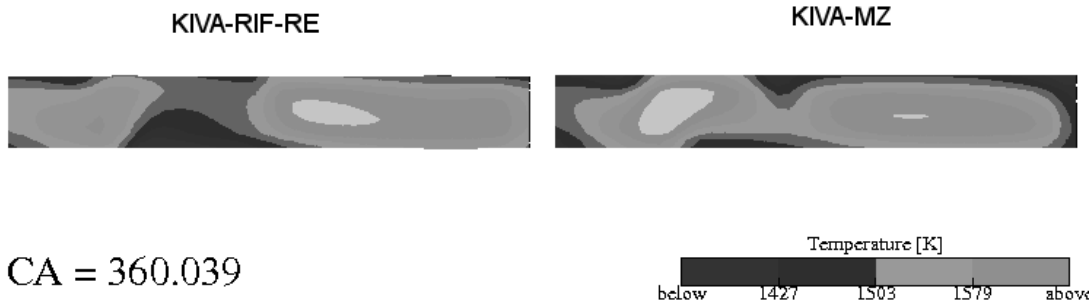

(b) Spatial Temperature Distribution at 360° CA

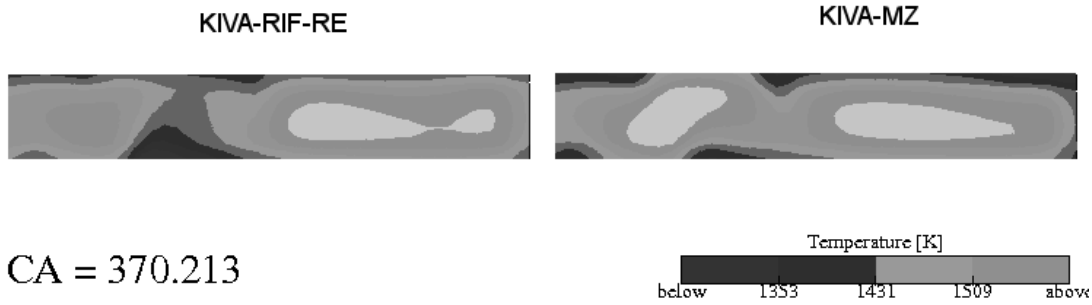

(c) Spatial Temperature Distribution at 370° CA

Figure 5.4: Comparison of RIF-ER and KMZ models in Spatial Evolution of Temperature Field Near TDC

case. Spatial temperature distributions near TDC were compared between the RIF-ER and the KMZ model results. It was found that there exists slight differences between the RIF-ER and KMZ predictions in spatial temperature. However, such difference may not affect the overall results as shown in Figure 5.3.

It can be concluded that the RIF-ER model predicts almost identical result to the KMZ model under close to HCCI combustion case, where the scalar dissipation rate is close to zero. Based on this observation, the RIF-ER model will be utilized in subsequent sections to simulate and analyze the effect of spray injection on PPCI combustion.

One thing should be noted is that in this case, the injection event and the combustion events are occurring at different times. In other words, the injection event occurs very early in the compression stroke, while the reaction does not proceed in significant amount until around 10° bTDC. As a result, the effect of spray vaporization in the reaction space becomes minimal, where the temperature is still too low and $Y_i(Z)$ are mostly at their mixing limit. As a result, in this case the RIF and the RIF-ER model are expected to produce results which are close to each other.

The KMZ model was expected to be able to model the PPCI combustion study in Section 5.4. However, it was found that the KMZ model is not able to treat higher equivalence ratio region, which occurs during injection period. The main purpose of KMZ code is to investigate HCCI combustion with thermal and/or species stratification (Babajimopoulos *et al.* , 2005). Local computational cells with equivalence ratio larger than unity were not considered during the model development.

5.4 Parametric Study on the Effect of Stratification on PPCI Combustion using RIF-ER Model

5.4.1 Experimental Setup

In this research, emphasis is made on more practical engine situations, and an experimental stratification study of Dec & Sjöberg (2003) was chosen as the reference case. In Dec & Sjöberg (2003), the effect of stratification on combustion efficiency and emissions was examined by a parametric study on SOI. A schematic diagram of the engine used in the experiment is shown in Figure 5.5.

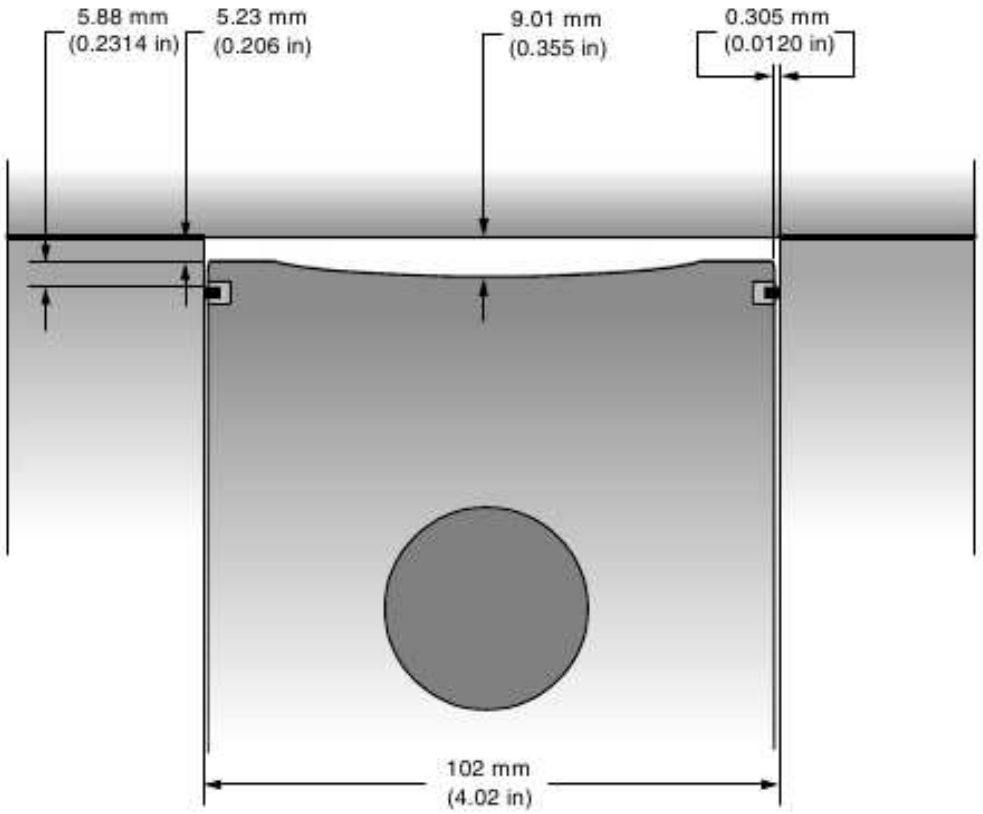

Figure 5.5: Experimental Setup

In the experiment, different levels of stratification were attained by varying SOI. Early injection was used to prepare a mixture with less stratification (more homogeneous) by providing ample amount time for the fuel and air to mix. Then stratification level was

Table 5.1: Engine and Injector Specifications

Displacement (Single Cylinder)	0.981 liter
Bore	102 mm
Stroke	120mm
Compression Ratio	18:1
IVC	205 ° CA
EVO	480 ° CA
Injector type	Hollow cone
Cone Angle	44 °
Fuel	Iso-octane
SOI Range	15-315° CA bTDC intake

increased by retarding SOI, such that the time for mixing before combustion is reduced. In the experiment, SOI was varied from early intake stroke (13° CA, measured from TDC at intake stroke) to late compression stroke (315° CA) for two different equivalence ratios of 0.1 and 0.2. These equivalence ratios were chosen to represent stable combustion ($\Phi = 0.2$) and low-load limit ($\Phi = 0.1$), respectively. The engine and injector specifications are shown in Table 5.1.

5.4.2 Numerical Setup

A computational mesh has been prepared with piston bowl and crevice volume as shown in Figure 5.6 at TDC, with axis boundary on the left hand side of the Figure. A parametric study similar to Dec & Sjöberg (2003) on the effect of SOI was conducted using the current numerical model implemented in KIVA3v. The operating condition simulated is shown in Table 5.2.

Table 5.2: Operating conditions

Equivalence ratio	0.1
DOI	0.26 ms
RPM	1200
SOI Range	230-320° CA bTDC intake
Fuel injection amount	0.012 g

Each simulation was conducted from IVC to EVO. Due to the limitation of a two-

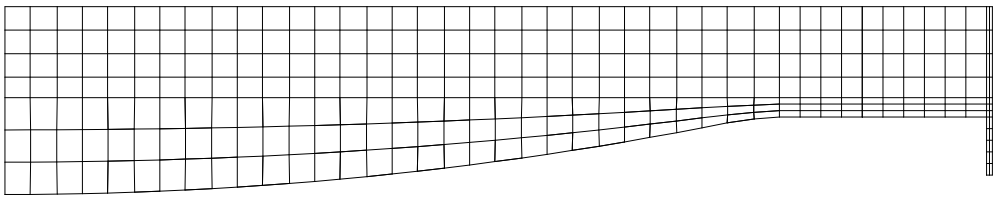

Figure 5.6: Computational mesh at TDC

dimensional mesh, SOI was varied only within the closed part of the cycle in numerical simulations from 240 CA to 315 CA. The fueling was kept constant for all SOI's as in Dec & Sjöberg (2003). The fuel used in the experiment was iso-octane, and a reaction mechanism by Tanaka *et al.* (2003) was used for reaction modeling in simulation.

5.4.3 Results and Discussion

At low equivalence ratio, combustion suffers mainly from incomplete bulk-gas reaction, particularly CO-to-CO_2 reaction due to low combustion temperatures (Dec & Sjöberg, 2003). The bulk-gas reaction can be enhanced by creating locally higher equivalence ratio zones, where the combustion temperature becomes higher. In this research, the case of low equivalence ratio (0.1), which was found to benefit from stratification, was reproduced by our numerical simulation.

Combustion efficiency and carbon monoxide mass at EVO are chosen as comparison variables to examine the effect of stratification on combustion. First, the trend of fuel efficiency against SOI is shown in Figure 5.7. Numerical results plotted in dashed line show good agreement in trend with the experimental data plotted in solid line. In overall SOI range, the numerical simulation predicted slightly higher combustion efficiency than the experiment. Both the experiment and simulation predicted about 30% increase in fuel efficiency by retarding SOI from 240°CA to 320°. The difference in absolute values may be attributed to different methods to determine fuel efficiency, and use of simple reaction

mechanism. In this paper, the fuel efficiency was determined by the following formula.

$$\eta_{\text{comb}} = \left| \frac{(\sum_i h_i Y_i)_{\text{EVO}} - (\sum_i h_i Y_i)_{\text{U,ref}}}{(\sum_i h_i Y_i)_{\text{EQ}} - (\sum_i h_i Y_i)_{\text{U,ref}}} \right| \tag{5.3}$$

where subscript (U,ref) denotes unreacted state at reference temperature of 400K.

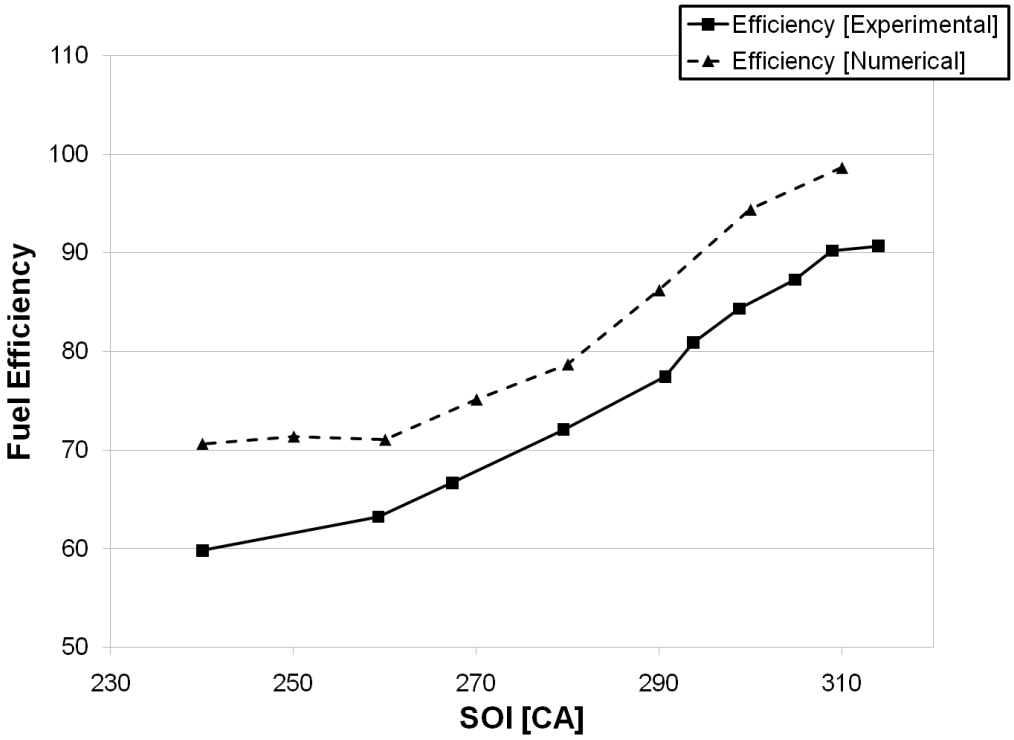

Figure 5.7: Efficiency comparison

The trend of CO emissions at EVO against SOI is shown in Figure 5.8. It has been reported in [6] that the rate of change in CO emissions becomes rapid as SOI becomes further retarded beyond 270° CA, as shown in Figure 5.8 with two trend lines. This specific change in trend is well captured by numerical simulation.

To examine the effect of different SOI on combustion, analysis on spatial equivalence ratio distribution at TDC was carried out for four different SOI (240, 270, 300 and 320 ° CA) which are marked by circles in Figure 5.8.

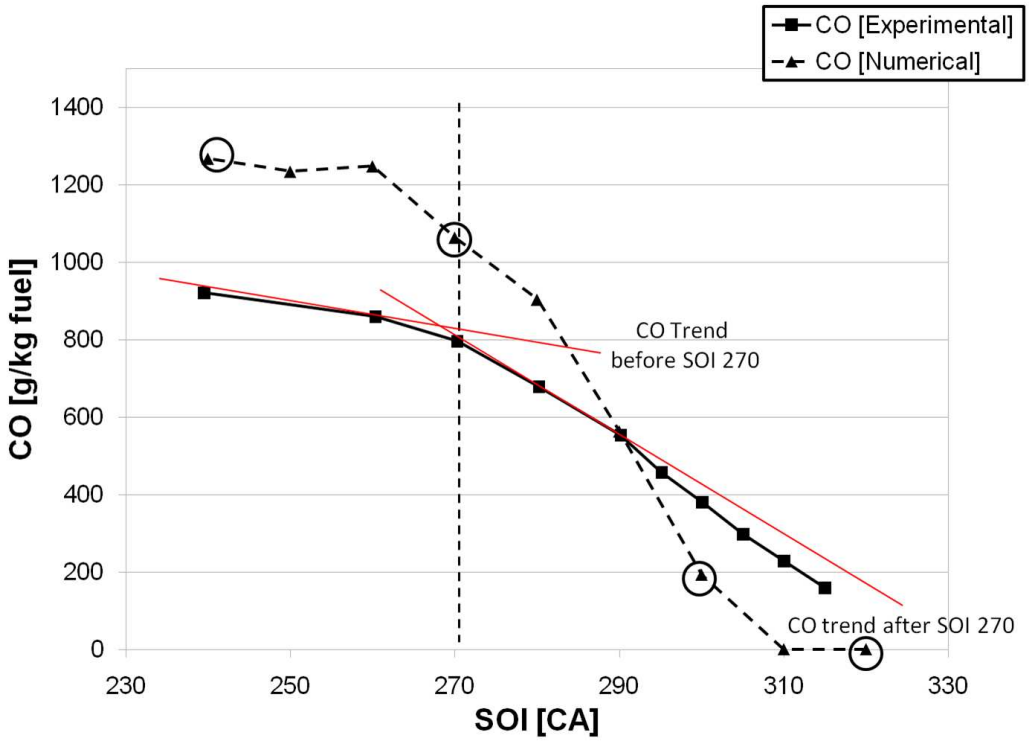

Figure 5.8: CO comparison

SOI 240° CA

First, an early injection case of SOI 240° CA is examined in Figure 5.9. Spatial equivalence ratio and temperature distributions are shown in Figure 5.9(a) and Figure 5.9(b), respectively. From Figure 5.9(a), most fuel is located at cylinder wall, with some fuel concentrated at midpoint from cylinder wall to piston center. Such distribution of fuel species is due to interaction between the spray and piston motion. Velocity and equivalence ratio distributions at 270° CA (30° CA after injection) are shown in Figure 5.10.

It was observed that fuel droplets are fully vaporized before they reach the piston surface. A secondary flow is developed by the interaction between spray momentum and piston motion to create two recirculation zones around the spray periphery. These two recirculating zones push the gaseous fuel into both directions, to the axis and to the cylinder wall. Further mixing in the late part of compression stroke results in fuel distribution at TDC as shown in Figure 5.9(a), with a small region close to the piston surface with high

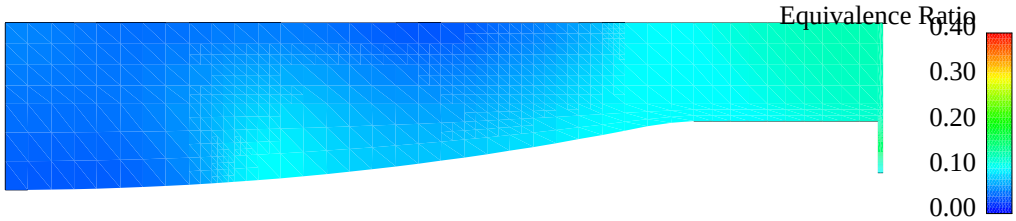

(a) Φ distribution

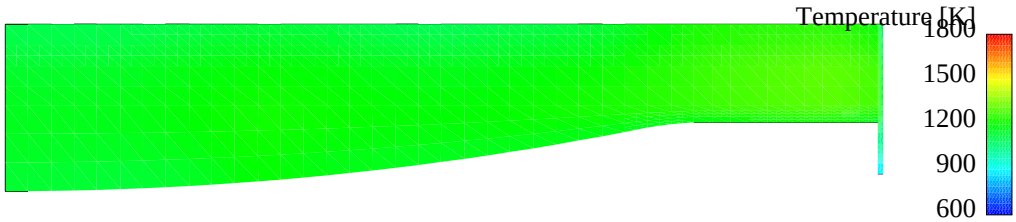

(b) Temperature distribution

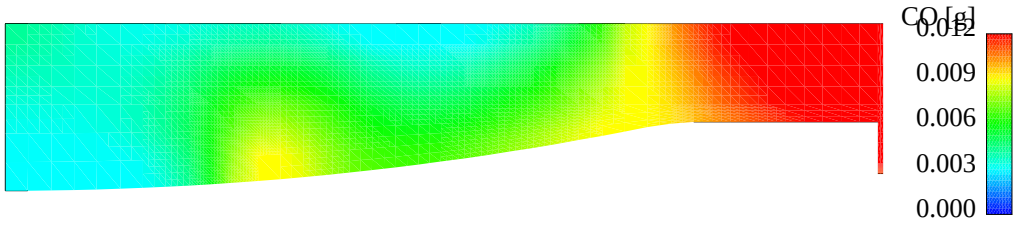

(c) CO distribution

Figure 5.9: Fuel, Temperature, and CO distribution at TDC, SOI= 240° CA

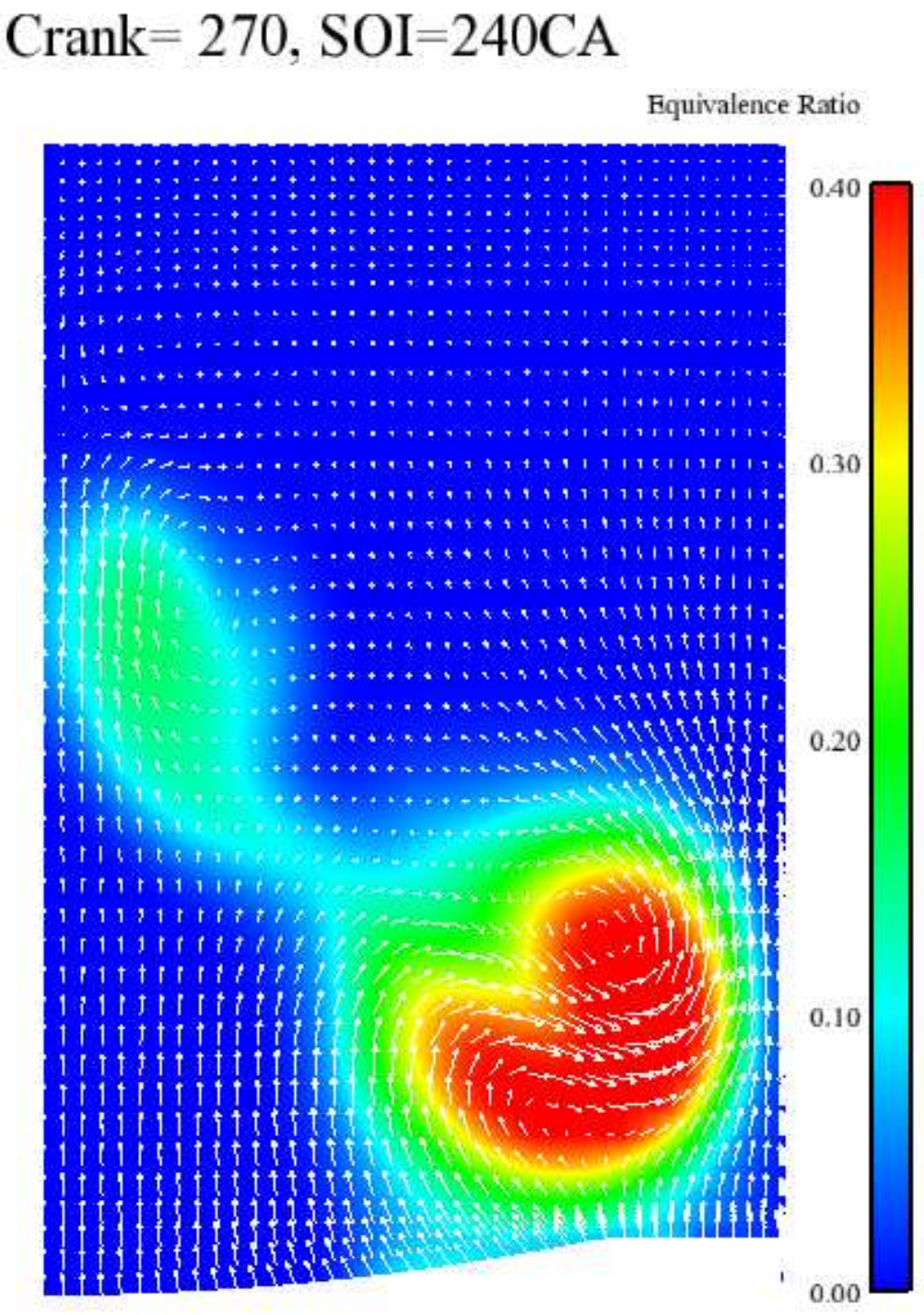

Figure 5.10: Velocity and fuel distribution at 270°, SOI=240° CA

concentration of fuel, while most of fuel is located near the cylinder wall.

The temperature distribution shown in Figure 5.9(b) is very homogeneous, indicating that it is mainly determined by thermodynamic compression. Very little contribution to the temperature field is made from chemical reaction, which results in low bulk-gas temperature. Subsequently, reaction cannot reach completion, and large amount of CO is produced as shown in Figure 5.9(c). Carbon monoxide is mostly located near the cylinder wall, where heat transfer to the wall results in lower temperature, preventing reaction completion.

SOI 270° CA

Similar plots for equivalence ratio, temperature and CO distributions for SOI 270° are shown in Figure 5.11.These distributions are similar to the earlier injection case of SOI 240°, shown in Figure 5.11. It is observed that as injection timing gets retarded, more fuel is being pushed to the center of the cylinder, as shown in Figure 5.11(a). In the previous case of SOI 240 CA, very small amount of fuel was be observed close to the cylinder axis, as shown in Figure 5.9(a). The temperature field shows more stratification than that of SOI 240° case. The high equivalence zone coincides with the high temperature zone in Figure 5.11(b). By comparing Figure 5.9 and Figure 5.11, it was found that the spatial distributions of equivalence and temperature do not significantly vary until SOI reaches 270° CA. Retarding SOI increases stratification level while not affecting the major flow structures. Reduction in CO is experienced with retarded SOI due to increased stratification and local high temperature area.

SOI 300° CA

Equivalence ratio, temperature and CO distributions with SOI 300° CA are shown in Figure 5.12(a). Two clearly separated regions exist for high equivalence ratio, resulting in significantly different equivalence ratio distribution compared to the earlier injection cases shown in Figure 5.9(a) and 5.11(a). This case shows higher concentration of fuel species

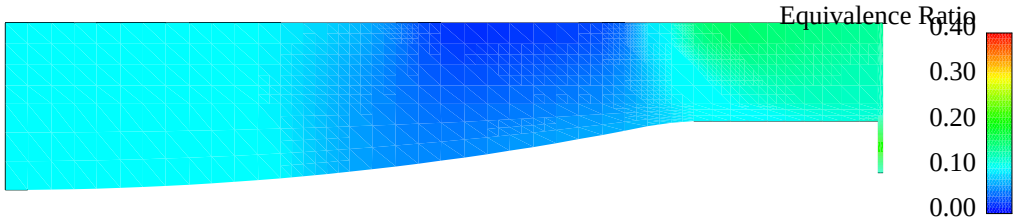

(a) Φ distribution

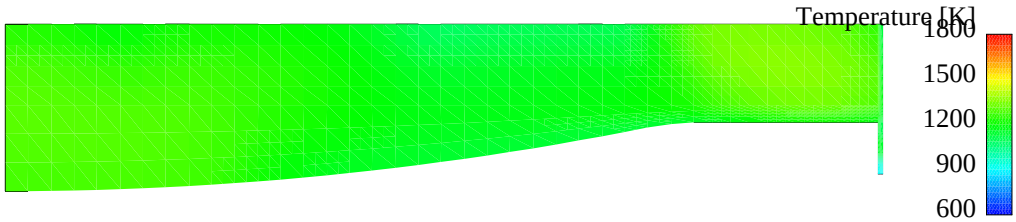

(b) Temperature distribution

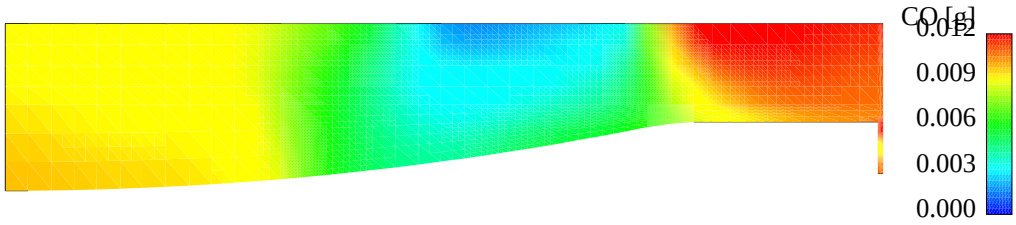

(c) CO distribution

Figure 5.11: Fuel, Temperature, and CO distribution at TDC, SOI= 270° CA

in two small regions, implying poor mixing due to shortened time for mixing with retarded SOI as well as spray-piston motion interaction.

Flow field and equivalence ratio distributions similar to Figure 5.10 are shown in Figure 5.13 at 10°CA after injection. With SOI being further retarded, droplets begin to hit the piston surface before being fully vaporized with higher velocity. This results in recirculation zones with faster velocity to push vaporized fuel into both directions faster. As a result,injected fuel rapidly creates two separated zones. The time for mixing has been reduced by retarded SOI. As a result, fuel species are found at two separated regions with higher equivalence ratio than global equivalence ratio, as shown in Figure 5.12(a).

Due to the higher local equivalence ratios, higher temperature regions are developed as shown in Figure 5.12(b). The CO levels shown in Figure 5.12(c) appear to be higher than those of the earlier injection cases. However, CO produced at this stage reacts further to CO_2 in the late part of cycle by high temperature. This results in reduction in CO at EVO as SOI gets retarded further than 270° CA as mentioned in Figure 5.8.

SOI 320° CA

An equivalence ratio distribution with SOI 320° CA is shown in Figure 5.14(a). In this case, most of the droplets hit the piston surface before vaporization to travel along the piston surface. As a result, the fuel distribution significantly differs from previous cases with earlier injection, to result in a single region with very high concentration of fuel. Due to the heavy stratification, a large portion of the in-cylinder region does not experience fuel-air mixing.

CO creation is confined to a relatively smaller portion of the cylinder as shown in Figure 5.14(c). It should be noticed that the high temperature region coincides with the high CO region in Figure 5.14. This high temperature allows the reaction to reach completion as time proceeds. Therefore, the final CO level is further reduced at EVO, compared to the level shown at TDC in Figure 5.14(c).

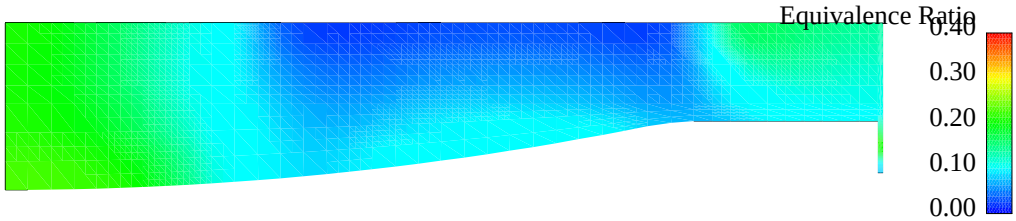

(a) Φ distribution

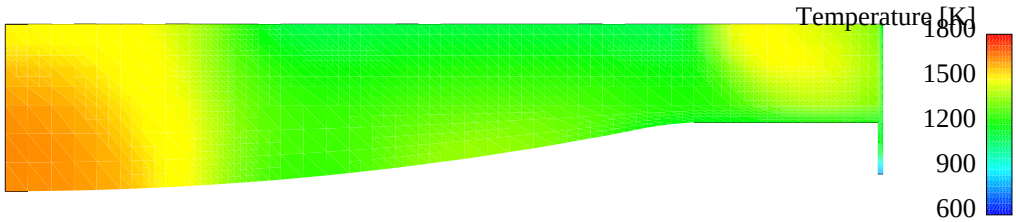

(b) Temperature distribution

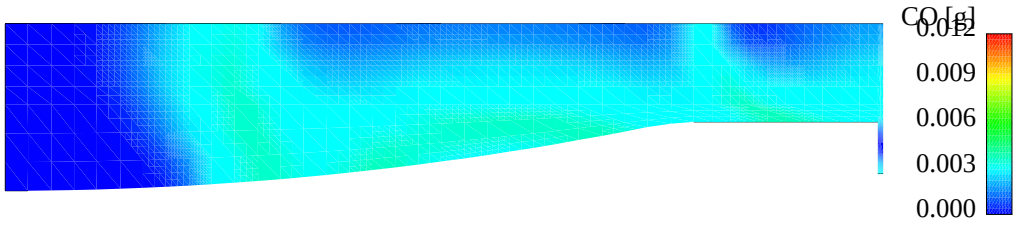

(c) CO distribution

Figure 5.12: Fuel, Temperature, and CO distribution at TDC, SOI= 300° CA

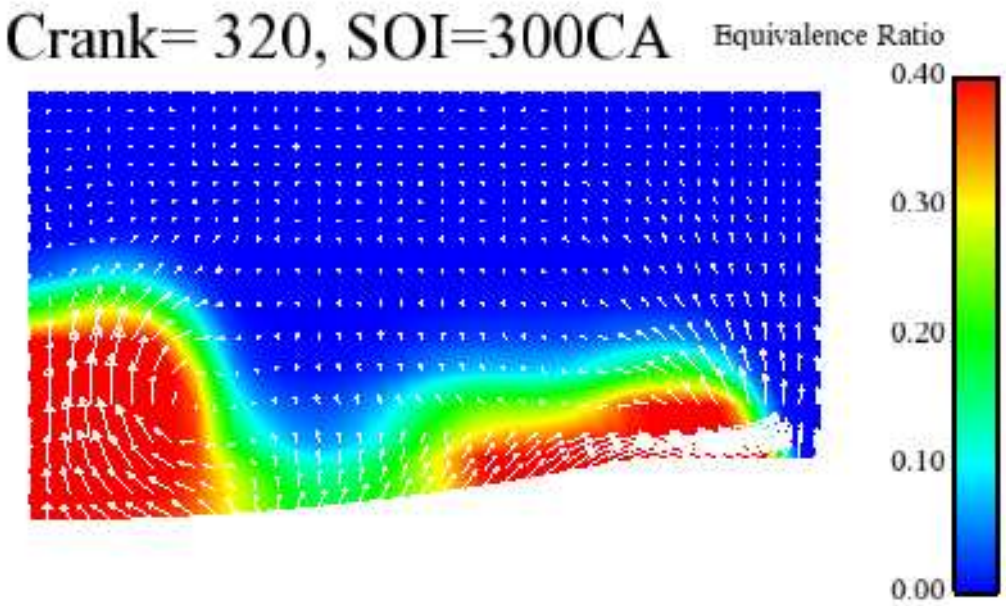

Figure 5.13: Velocity and fuel distribution at 310° CA, SOI=300° CA

5.5 Summary and Discussion

The RIF-ER model has been used in a parametric study of the effect of stratification on PPCI combustion. More specifically, the effect of different SOI on spatial distribution of fuel, temperature and CO level has been examined. It has been found that SOI before 270° produces nearly homogeneous mixture distribution at TDC, and the flow structure is not heavily affected by changes in SOI. Changes in the flow structure are observed when SOI becomes retarded further than 270°. The mixture at TDC becomes more stratified due to the interaction between the spray and flow field to create local hot region which promotes reaction.

The numerical results were in good agreement with experimental data, though some differences are observed. The differences between measured and modeled fuel efficiency may be attributed to the simplified reaction mechanism used. Nevertheless, the RIF-ER has shown promise in modeling PPCI combustion by reproducing the effect of stratification well.

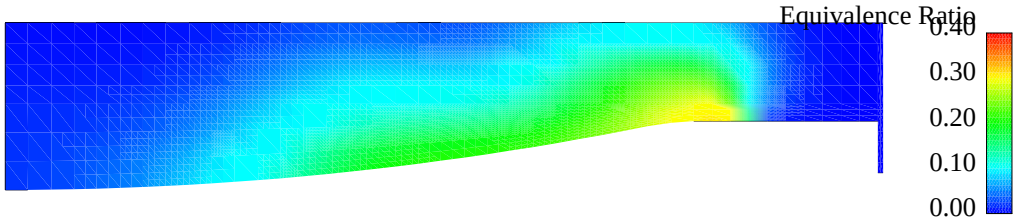

(a) Φ distribution

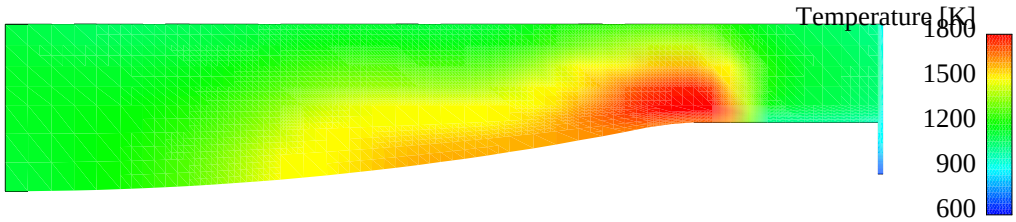

(b) Temperature distribution

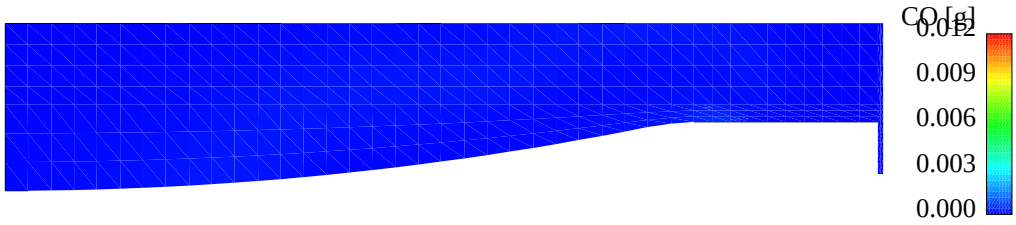

(c) CO distribution

Figure 5.14: Fuel, Temperature, and CO distribution at TDC, SOI= 320° CA

Chapter 6
Conclusions

6.1 Conclusions and Contributions

6.1.1 Summary

The RIF model has been extended to account for the effect of vaporization in the reaction space for use in DI turbulent combustion.

Lack of vaporization treatment in the conventional flamelet approach has been identified. A modified flamelet equation has been derived in Chapter 3 by rigorous mathematical derivation. A model for vaporization source terms in the reaction space is also suggested in Section 3.5.3. Detailed discussion on the effect of vaporization terms have been carried out in Section 3.3.4 to understand how these source terms affect the reaction space and account for the vaporization history.

The proposed model, RIF-ER, has been validated using data from both a fundamental experiment and engine experiments. First, the effect of vaporization terms was examined by considering an idealized control volume without any boundary mass transfer. The effect of vaporization, or equivalently, fuel addition at different stages in the reaction space evolution has been examined using the idealized control volume as discussed in Section 3.4. Such setup enabled separate consideration of fuel addition on the reaction space and lead to the conclusion it produces different results from the RIF model. The result has been analyzed to reveal that consideration of fuel addition terms is necessary in spray combustion modeling.

Then, validation of the suggested model was carried out based on a spray combustion

experiment by Akiyama *et al.* (1998), which was designed to resemble combustion in a diesel engine. In Akiyama *et al.* (1998), a rapid compression machine with direct injection was used to investigate the spray combustion phenomenon. Results from both the RIF and the RIF-ER models showed good agreement with the experiments, while the RIF-ER model prediction showed a better agreement in the pressure history. Spatial distributions of unreacted fuel species at various phases in combustion have been analyzed. It was concluded that the suggested model is well capturing the effect of fuel vaporization in the reaction space, leading to more accurate prediction in pressure and local species distribution.

6.1.2 Conclusions

6.1.3 Improved RIF model Accounting for Evaporation in the Reaction Space

Consideration of the vaporization effect is important to properly model the spray combustion using the flamelet approach. The effect of droplet vaporization in the reaction space can either increase or decrease the fuel mass fraction, based on the relative amount of $\frac{\partial Y_i}{\partial Z}$ and $\frac{1-Y_{\text{fuel}}}{1-Z}$. The effect of droplet vaporization is realized by moderation of the reaction progress. Without proper consideration of these droplet vaporization terms, the reaction may progress faster or slower than reality. Such effect may result in increased pressure and temperature during combustion, which can result in larger values of NO emissions. Consequently, the effect of vaporization should be considered in the reaction space to correct such prediction.

The effect of vaporization in the reaction space should be considered in cases where reaction occurs during the injection period, which occurs in most of DICI engine operating conditions. The effect of vaporization terms on the fuel species in the reaction space should be significant especially at late injection cases, which exhibit longer ignition delay. Evaporation and partial reaction occurs at the same time during the ignition delay. Accurate

prediction of fuel content and progress in reaction with the vaporization effect is important for combustion modeling at such cases.

PPCI combustion with high rate of EGR and DI also should consider the effect of vaporization. The increased turbulence from DI requires a turbulence-chemistry closure model. Conventional KIVA-Chemkin or KIVA-MZ model, which are based on the separation of chemistry and turbulence, may not be appropriate such conditions. The RIF-ER model provides a solid turbulence-chemistry closure based on the RIF model.

Even if the separation of chemistry from the turbulence is assumed in PPCI, the KIVA-Chemkin model would require large computational time when applied to PPCI engine modeling with detailed chemistry. Such large amount of computing resource would make KIVA-Chemkin model hardly justifiable for practical application. The KIVA-MZ model should provide better computational efficiency, by taking advantage of the multi-zone approach. However, the KIVA-MZ model is not capable of modeling rich region during the injection. The KIVA-RIF-ER model is free of such restrictions. Moreover, the KIVA-RIF-ER model is capable of modeling HCCI based on the similarities in the reaction governing equation with the multi-zone. It can be said that the proposed KIVA-RIF-ER model is the most reasonable computational model for modeling DI/PPCI engines, which can provide both reduction in computational resources and satisfactory results.

6.1.4 Computing Performance by Parallelization

Partial parallelization has been implemented for efficient use of computational resources. Parallelization of the reaction solver and the numerical integration subroutine can provide up to 30% decrease in computational time, based on the CFD overhead. It was found that speedup by parallelization heavily depends on the CFD solver overhead, since the CFD solver has not been parallelized yet. To obtain further reduction in computational resources, further parallelization in the CFD solver is required.

6.2 Future Work

The RIF model has been widely applied to modeling non-premixed combustion. However, a few issues should be addressed to improve the current spray modeling approach for application to DI/PPCI engines First, future work regarding spray combustion will be suggested. Then suggestions for future work regarding the general flamelet approach will be proposed.

6.2.1 Spray modeling based on flamelet approach

As discussed in the current research, the flamelet model requires consideration of vaporization terms in the reaction space to be applied to spray combustion. The suggested model in this paper has shown promise in modeling spray combustion. Obviously, there is still room for improvements regarding the spray combustion modeling, as discussed below.

1. Multiple Flamelets Approach

   The current results are based on a single flamelet approach. The main reason for utilizing single flamelet is to prevent the effect of droplet vaporization being obscured by multiple flamelets. The current study should be expanded to utilize the multiple flamelets to properly account for spatially varying scalar dissipation rate and vaporization.

   Two different approach for multiple flamelets approach is suggested. The first approach, which requires further contemplation in its application, addresses the issue of non-homogeneous vaporization. For example, we can safely assume two different locations $\vec{x}_1, \vec{x}_e$ in the physical space, which share the same Z value Z at $t + \Delta t$. The physical space is governed by a single flamelet $Y_i(t, Z)$. Let us further assume that at the last time step, vaporization has occurred at $\vec{x}_e$ but not at $\vec{x}_1$, such that the vaporization effect has been updated into the reaction space to result in $Y_i^e(t + \Delta t, Z)$. As $\vec{x}_e$ has experienced the vaporization,it is reasonable to use Y_i^e to determine the local species concentration at $\vec{x}_e$. However, $\vec{x}_1$ has not undergone vaporization, which

makes application of Y^e for all computational cells regardless of vaporization in the physical space. A simple remedy is creation of new flamelets based on whether vaporization has occurred at given time and location or not. However, in this case it becomes hard to determine a tracker such as an Eulerian Particle. Also, in worst case, at each time step the total number of flamelets may double up. This will increase the computational cost to make the flamelet approach hardly justifiable. Further consideration on the effect of non-homogeneous vaporization should be followed after the current research.

Instead, one may follow a multiple flamelets approach suggested by (Barths *et al.* , 2000) as in Eulerian Particle Flamelet Model. The droplet source term can be identified for each flamelet as following.

$$\dot{\rho}_l(Z) = \int_V \dot{\rho} P_{c,l}(\zeta|Z)\mathrm{d}V \tag{6.1}$$

$$P_{c,l}(\zeta|Z) = \frac{\int_V \tilde{I}_l \dot{\rho}\,\delta(\zeta - Z)\mathrm{d}V}{\int_V \dot{\rho}\,\mathrm{d}V} \tag{6.2}$$

In other words, the effect of vaporization is distributed to different flamelets denoted by l, based on the Eulerian Particle $\tilde{I}_l$. This approach still carries the issue of non-homogeneous spatial vaporization unaddressed. However, this may still be a feasible and meaningful option to investigate.

2. Effect of spray on the variance equations.

   As discussed in Section 3.1, the effect of spray on flamelet-based models are twofold. First, it increases the turbulence from the interaction between high-velocity droplets and ambient gas. Also it affects the reaction space, which has been properly accounted for by the current research.

   The effect of spray on the variance equation is still an active research topic. It is generally understood that the injection of spray will increase $\widetilde{Z''^2}$ to result in higher

$\tilde{\chi}_{st}$. Also the PDF will have to be properly redefined. If a beta function PDF is to be used, its minimum and maximum values should be properly defined to clip the beta PDF within a realizable region.

6.2.2 General Improvement of flamelet apporach - Heat Transfer

One of the most important issues to be addressed in the flamelet approach is accounting for heat transfer. Since all local cells are mapped into one single flamelet, the computational cells having the same Z values will share similar thermodynamic properties, regardless of its physical location or different level of local heat transfer.

This issue has been successfully addressed by Hergart & Peters (2002). Also, there are efforts being made to incorporate both the mixture fraction and the total enthalpy as conserved scalars. In this approach, local variation in heat transfer can be captured by a conserved scalar defined by the total enthalpy. However, the final governing equations will have a number of unclosed terms regarding dissipation rates, such as $\frac{\partial Y_i}{\partial Z}\frac{\partial Y_i}{\partial H}, \frac{\partial Y_i^2}{\partial^2 H}$. Proper modeling based on physics is required to account for these terms.

Appendices

Appendix A

Relationships between $\dot{\rho}_i$ and $\dot{\rho}_Z$

Vaporization and increase in density is considered in CFD code KIVA3v (Amsden *et al.* , 1991). An Adaptive Lagrangian-Eulerian scheme is used in KIVA3v, and vaporization is considered in Lagrangian phase with change in volume.

$$\frac{\partial \rho_i}{\partial t} = \dot{\rho}_i \tag{A.1}$$

$$\frac{\partial (\rho Z)}{\partial t} = \dot{\rho}_Z \tag{A.2}$$

If we discretize (A.2) with a time step Δt,

$$\frac{\rho^{t+\Delta t} Z^{t+\delta t} - \rho^t Z^t}{\Delta t} = \dot{\rho}_Z \tag{A.3}$$

Then, from the definition of Z in (2.2),

$$\dot{\rho}_Z = \frac{1}{\Delta t} \times \left[\rho^{t+\Delta t} \sum_i Y_i^{t+\Delta t} \zeta_i' - \rho^t \sum_i Y_i^t \zeta_i' \right] \tag{A.4}$$

$$\dot{\rho}_Z = \frac{1}{\Delta t} \times \left[\frac{m+\Delta m}{V} \sum_i \frac{m_i + \Delta m_i}{m+\Delta m} \zeta_i' - \frac{m}{V} \sum_i \frac{m_i}{m} \zeta_i' \right] \tag{A.5}$$

where m is the mass at t and Δm is increase in mass during Δt. ζ' denotes normalized species carbon element mass fraction, $\zeta' = \zeta_i / \zeta_{\text{Fuel}}$. If only one single species, namely a fuel species, is considered for vaporization, $\Delta m_i = 0$ for all species except fuel species.

$$\begin{aligned}
\dot{\rho}_Z &= \frac{1}{\Delta t} \times \left[\frac{\cancel{m + \Delta m}}{V} \sum_i \frac{m_i + \Delta m_i}{\cancel{m + \Delta m}} \zeta_i' \right. \\
&\quad \left. - \frac{\cancel{m}}{V} \sum_i \frac{m_i}{\cancel{m}} \zeta_i' \right] && \text{(A.6)} \\
&= \frac{1}{\Delta t} \times \left[\sum_i \frac{\cancel{m_i} + \Delta m_i - \cancel{m_i}}{V} \zeta_i' \right] && \text{(A.7)} \\
&= \sum_i \dot{\rho}_i \zeta_i' && \text{(A.8)}
\end{aligned}$$

Since we are interested in injection with single fuel species,

$$\begin{aligned}
\dot{\rho}_Z &= \sum_i \dot{\rho}_i \zeta_i' && \text{(A.9)} \\
&= \dot{\rho}_{\text{Fuel}} \frac{\cancel{\zeta_{\text{Fuel}}}}{\cancel{\zeta_{\text{Fuel}}}} && \text{(A.10)} \\
\text{Therefore,} \quad \dot{\rho}_Z &= \dot{\rho}_{\text{Fuel}} && \text{(A.11)}
\end{aligned}$$

for a single fuel species injection.

Appendix B

Summary of Governing Equations in Combustion Models Based on Flamelet Approach Applied to Spray Combustion Modeling

Table B.1: Comparison of Governing Equations in Spray Combustion with Laminar Flamelet Model

	Spray	$\tilde{Z}$ conservation	$\widetilde{Z''^2}$ conservation	Reaction Equation
Peters (1984)	No	$\bar{\rho}\frac{\partial \tilde{Z}}{\partial t}+\bar{\rho}\tilde{\vec{u}}\cdot\nabla\tilde{Z}=\nabla\cdot(\bar{\rho}D\nabla\tilde{Z})$	$\bar{\rho}\frac{\partial\widetilde{Z''^2}}{t}+\bar{\rho}\tilde{\vec{u}}\cdot\nabla\widetilde{Z''^2}=$ $\nabla\cdot\left(\bar{\rho}D\nabla\widetilde{Z''^2}\right)+2\bar{\rho}D_t(\nabla\tilde{Z})^2-\bar{\rho}\tilde{\chi}$	$\rho\frac{\partial Y_i}{\partial t}=\frac{\rho}{Le}\frac{\tilde{\chi}_Z}{2}\frac{\partial^2 Y_i}{\partial Z^2}+\omega_i$
Barths *et al.* (1998)	Yes	$\bar{\rho}\frac{\partial \tilde{Z}}{\partial t}+\bar{\rho}\tilde{\vec{u}}\cdot\nabla\tilde{Z}=\nabla\cdot(\bar{\rho}D\nabla\tilde{Z})+\dot{\bar{\rho}}_Z$	$\bar{\rho}\frac{\partial\widetilde{Z''^2}}{t}+\bar{\rho}\tilde{\vec{u}}\cdot\nabla\widetilde{Z''^2}=$ $\nabla\cdot\left(\bar{\rho}D\nabla\widetilde{Z''^2}\right)+2\bar{\rho}D_t(\nabla\tilde{Z})^2-\bar{\rho}\tilde{\chi}$	$\rho\frac{\partial Y_i}{\partial t}=\frac{\rho}{Le}\frac{\tilde{\chi}_Z}{2}\frac{\partial^2 Y_i}{\partial Z^2}+\omega_i$
Hergart & Peters (2002)	Yes	$\bar{\rho}\frac{\partial \tilde{Z}}{\partial t}+\bar{\rho}\tilde{\vec{u}}\cdot\nabla\tilde{Z}=\nabla\cdot(\bar{\rho}D\nabla\tilde{Z})+\dot{\bar{\rho}}_Z$	$\bar{\rho}\frac{\partial\widetilde{Z''^2}}{t}+\bar{\rho}\tilde{\vec{u}}\cdot\nabla\widetilde{Z''^2}=$ $\nabla\cdot\left(\bar{\rho}D\nabla\widetilde{Z''^2}\right)+2\bar{\rho}D_t(\nabla\tilde{Z})^2-\bar{\rho}\tilde{\chi}$	$\rho\frac{\partial Y_i}{\partial t}=\frac{\rho}{Le}\frac{\tilde{\chi}_Z}{2}\frac{\partial^2 Y_i}{\partial Z^2}+\omega_i$
Kim *et al.* (2004)	Yes	$\bar{\rho}\frac{\partial \tilde{Z}}{\partial t}+\bar{\rho}\tilde{\vec{u}}\cdot\nabla\tilde{Z}=\nabla\cdot(\bar{\rho}D\nabla\tilde{Z})+\dot{\bar{\rho}}_Z$	$\bar{\rho}\frac{\partial\widetilde{Z''^2}}{t}+\bar{\rho}\tilde{\vec{u}}\cdot\nabla\widetilde{Z''^2}=$ $\nabla\cdot\left(\bar{\rho}D\nabla\widetilde{Z''^2}\right)+2\bar{\rho}D_t(\nabla\tilde{Z})^2-\bar{\rho}\tilde{\chi}$ $+2\left(\bar{\rho}\widetilde{Z\omega_v}-\bar{\rho}\tilde{Z}\tilde{\omega}_v\right)+\bar{\rho}\tilde{Z}^2\tilde{\omega}_v-\bar{\rho}\widetilde{Z^2\omega_v}$	$\rho\frac{\partial Y_i}{\partial t}=\frac{\rho}{Le}\frac{\tilde{\chi}_Z}{2}\frac{\partial^2 Y_i}{\partial Z^2}+\omega_i$
(Weber *et al.* , 2007)	Yes	$\bar{\rho}\frac{\partial \tilde{Z}}{\partial t}+\bar{\rho}\tilde{\vec{u}}\cdot\nabla\tilde{Z}=\nabla\cdot(\bar{\rho}D\nabla\tilde{Z})+\dot{\bar{\rho}}_Z$	$\bar{\rho}\frac{\partial\widetilde{Z''^2}}{t}+\bar{\rho}\tilde{\vec{u}}\cdot\nabla\widetilde{Z''^2}=$ $\nabla\cdot\left(\bar{\rho}D\nabla\widetilde{Z''^2}\right)+2\bar{\rho}D_t(\nabla\tilde{Z})^2-\bar{\rho}\tilde{\chi}$	$\rho\frac{\partial Y_i}{\partial t}=\frac{\rho}{Le}\frac{\tilde{\chi}_Z}{2}\frac{\partial^2 Y_i}{\partial Z^2}+\omega_i$
Current Model	Yes	$\bar{\rho}\frac{\partial \tilde{Z}}{\partial t}+\bar{\rho}\tilde{\vec{u}}\cdot\nabla\tilde{Z}=\nabla\cdot(\bar{\rho}D\nabla\tilde{Z})+\dot{\bar{\rho}}_Z$	$\bar{\rho}\frac{\partial\widetilde{Z''^2}}{t}+\bar{\rho}\tilde{\vec{u}}\cdot\nabla\widetilde{Z''^2}$ $=\nabla\cdot\left(\bar{\rho}D\nabla\widetilde{Z''^2}\right)+2\bar{\rho}D_t(\nabla\tilde{Z})^2-\bar{\rho}\tilde{\chi}$	$\rho\frac{\partial Y_i}{\partial t}+\dot{\rho}_Z\frac{\partial Y_i}{\partial Z}=$ $\frac{\rho}{Le}\frac{\tilde{\chi}_Z}{2}\frac{\partial^2 Y_i}{\partial Z^2}+\omega_i+\dot{\rho}_i$

Bibliography

Aceves, S. M., Flowers, D. L., Westbrook, C. K., Smith, J. R., Pitz, W. J., Christensen, M., & Johansson, B. 2000. A multi-zone model for prediction of hcci combustion and emissions. *Sae technical paper series 2000-01-0327*.

Akiyama, H., Nishimura, H., Ibaraki, Y., & Iida, N. 1998. Study of diesel spray combustion and ignition using high-pressure fuel injection and a micro-hole nozzle with a rapid compression machine: Improvement of combustion using low cetane number fuel. *Jsae review*, **19**(4), 319 – 327.

Amsden, A. 1997. A block-structured kiva program for engines with vertical or canted valves. *La-13313-ms*.

Amsden, A. A., O'Rourke, P. J., & Butler, T. D. 1991. KIVA-3: An unstructured KIVA program for complex geometries. *Los alamos national laboratory document la-ur-91-138*.

Babajimopoulos, A., Assanis, D. N., & Fiveland, S. B. 2002. An approach for modeling the effects of gas exchange processes on hcci combustion and its application in evaluating variable valve timing control strategies. *Sae technical paper series 2002-01-2829*.

Babajimopoulos, A., Assanis, D.N., Flowers, D.L., Aceves, S.M., & Hessel, R.P. 2005. A fully coupled computational fluid dynamics and multi-zone model with detailed chemical kinetics for the simulation of premixed charge compression ignition engines. *International journal of engine research*, **6**(5), 497 – 512.

Barths, H., Antoni, C., & Peters, N. 1998. Three-dimensional simulation of pollutant formation in a di diesel engine using multiple interactive flamelets. *Sae technical paper series 982459*.

Barths, H., Hasse, C., Bikas, G., & Peters, N. 2000. Simulation of combustion in direct injection diesel engines using a eulerian particle flamelet model. *Symposium (international) on combustion*, **28**(1), 1161 – 1167.

Berntsson, A. W., & Denbratt, I. 2007. Optical study of hcci combustion using nvo and an si stratified charge. *Sae paper 2007-24-0012*.

Blakeman, P., Chiffey, A., Phillips, P., Twigg, M., & Walker, A. 2003. Developments in diesel emission aftertreament technology. *Brasil society of automotive engineers conference paper paper number 2003-01-3753 e. 2003*.

Brewster, S., Cathcart, G., & Zavier, C. 2008. The potential of enhanced hcci/cai control through the application of spray-guided direct injection. *Sae paper 2008-01-0035*.

Chen, Gung, & Gomez, Alessandro. 1992. Counterflow diffusion flames of quasi-monodisperse electrostatic sprays. *Symposium (international) on combustion*, 1531 – 1539.

Chen, J.-Y., Chen, Yi-Hann, & Choi, Young. 2008. Development and validation of isooctane skeletal mechanisms based on llnl detailed mechanism. *International journal of vehicle design*, **46**(1), 128 – 38.

Cheng, Wai K. 2007. Personal conversation. *at ltc bi-annual meeting*.

Christensen, M., Hultqvist, A., & Johansson, B. 1999. Demonstrating the multi-fuel capability of a homogeneous charge compression ignition engines with variable compression ratio. *Sae technical paper series 1999-01-3679*.

Cook, D. J., & Peters, N. 2005. Enthalpy-based flamelet model for hcci applied to a rapid compression machine. *Sae technical paper series 2005-01-3735*.

Dec, J. E., & Sjöberg, M. 2003. A parametric study of HCCI combustion the sources of emissions at low loads and the effects of GDI fuel injection. *Sae paper 2003-01-0752*.

Dec, J.E. 2002. A computational study of the effects of low fuel loading and egr on heat release rates and combustion limits in hcci engines. *Sae technical paper series 2002-01-1309*.

Demoulin, F. X., & Borghi, R. 2002. Modeling of turbulent spray combustion with application to diesel like experiment. *Combustion and flame*, **129**(3), 281 – 293.

Dukowicz, John K. 1980. A particle-fluid numerical model for liquid sprays. *Journal of computational physics*, **35**(2), 229 – 253.

Flowers, D., Aceves, S., J., Martinez-Friasm, Hessel, R., , & Dibble, R. 2003. Effect of mixing on hydrocarbon and carbon monoxide emissions prediction for isooctane hcci engine combustion using a multi-zone detailed kinetics solver. *Sae paper 2003-01-1821*.

Flowers, D. L., Aceves, S. M., & Babajimopoulos, A. 2006. Effect of charge non–uniformity on heat release and emissions in pcci engine combustion. *Sae technical paper series 2006-01-1363*.

Ge, Hai-Wen, & Gutheil, Eva. 2008. Simulation of a turbulent spray flame using coupled pdf gas phase and spray flamelet modeling. *Combustion and flame*, **153**(1-2), 173 – 185.

Goix, P.J., Edwards, C.F., Cessou, A., Dunsky, C.M., & Stepowski, D. 1994. Structure of a methanol/air coaxial reacting spray near the stabilization region. *Combustion and flame*, **98**(3), 205 – 219.

Hamosfakidis, V. 2006. *A two conserved scalar model for hcci and ppci engine applications*. Ph.D. thesis, The University of Michigan.

Hasse, C., & Peters, N. 2005. A two mixture fraction flamelet model applied to split injections in a di diesel engine. *Proceedings of the combustion institute*, **30 II**, 2755 – 2762.

Haworth, D. C. 2005. A review of turbulent combustion modeling for multidimensional in-cylinder cfd. *Sae technical paper series 2005-01-0993*.

Hergart, C., & Peters, N. 2002. Applying the representative interactive flamelet model to evaluate the potential effect of wall heat transfer on soot emissions in a small-bore direct-injection diesel engine. *Journal of engineering for gas turbines and power*, **124**(4), 1042 – 1052.

Hergart, C. A. 2001. *Modeling combustion and soot emissions*. Ph.D. thesis, RWTH Achen.

Hergart, C. A., Barths, H., & Siewert, R. M. 2005. Modelling approaches for premixed charge compression ignition combustion. *Sae paper 2005-01-0218*.

Hessel, R. P., Foster, D. E., Aceves, S. M., Davisson, M. L., Espinosa-Loza, F., Flowers, D. L., Pitz, W. J., Dec, J. E, Sjöberg, M., & Babajimopoulos, A. 2008. Modelling iso-octane HCCI using CFD with multi-zone detailed chemistry; comparison to detailed speciation data over a range of lean equivalence ratios. *Sae paper 2008-01-0047*.

Hindmarsh, A. C. 1983. Odepack, a systematized collection of ode solvers. *Scientific computing*, **1**, 55–64.

Hirt, C.W., Amsden, A.A., & Cook, J.L. 1974. An arbitrary lagrangian-eulerian computing method for all flow speeds. *Journal of computational physics*, **14**(3), 227 – 53.

Hollmann, C., & Gutheil, E. 1996. Modeling of turbulent spray diffusion flames including detailed chemistry. *Symposium (international) on combustion*, **1**, 1731 – 1738.

Hollmann, C., & Gutheil, E. 1998. Flamelet-modeling of turbulent spray diffusion flames based on a laminar spray flame library. *Combustion science and technology*, **135**(1-6), 175 – 192.

Hong, S., Wooldridge, M. S., Im, H. G., Assanis, D. N., & Kurtz, E. 2008. Modeling of diesel combustion, soot and NO emissions based on a modified eddy dissipation concept. *Combustion science and technology*, **180**(8), 1421 – 1448.

Hwang, W., Dec, J. E., & Sjörberg, M. 2007. Fuel stratification for low-load hcci combustion: Performance and fuel-plif measurements. *Sae paper 2007-01-4130*.

Kee, R.J., Rupley, F.M., & Miller, J.A. 1989a. Chemkin-ii: A fortran chemical kinetics package for the anlysis of gas-phase chemical kinetics. *Sand89-8009*.

Kee, R.J., Rupley, F.M., & Miller, J.A. 1989b. *Chemkin-iii : a fortran chemical kinetics package for the analysis of gas-phase chemical and plasma kinetics.* Sand96-8216.

Kim, H., Heo, N., Kim, Y. M., Lee, J. H., & Lee, J. K. 2004. Numerical study of combustion processes and pollutant formation in HSDI diesel engines. *Sae paper 2004-01-0126*.

Klimenko, A.Y., & Bilger, R.W. 1999. Conditional moment closure for turbulent combustion. *Progress in energy and combustion science*, **25**(6), 595 – 687.

Lechner, G., Jacobs, T., Chryssakis, C., Assanis, D., & Siewert, R. 2005. Evaluation of a narrow spray cone angle, advanced injection timing strategy to achieve partially premixed compression ignition combustion in a diesel engine. *Sae technical paper series2005-01-0167*.

Liu, S., Hewson, J. C., Chen, J. H., & Pitsch, H. 2004. Effects of strain rate on high-pressure nonpremixed n-heptane autoignition in counterflow. *Combustion and flame*, **137**(3), 320 – 39.

Liu, S., Hewson, J. C., & Chen, J. H. 2006. Nonpremixed n-heptane autoignition in unsteady counterflow. *Combustion and flame*, **145**(4), 730 – 739.

Magnussen, B. F., & Hjertager, B. H. 1976. On mathematical modeling of turbulent combustion with special emphasis on soot formation and combustion. *Proceedings of the combustion institute*, 719 – 729.

McDonell, V. G., & Samuelsen, G.S. 1995. An experimental data base for the computational fluid dynamics of reactiong and nonreacting methanol sprays. *Journal of fluids engineering*, **117**, 145.

McKeeman, William M. 1962. Algorithm 145: Adaptive numerical integration by simpson's rule. *Commun. acm*, **5**, 604.

Najt, P. M., & Foster, D. E. 1983. Compression-ignited homogeneous charge combustion. *Sae technical paper series 830264*.

O'Rouke, P. J., & Amsden, A. A. 1987. The tab method for numerical calculation of spray droplet breakup. *Sae technical paper series 872089*.

Patankar, S. V. 1980. *Numerical heat transfer and fluid flow*. Hemisphere Publishing Corporation.

Patterson, M. A., Kong, S. C., Hampson, G.J., & Reitz, R. D. 1994. Modeling the effects of fuel injection characteristics on diesel engine soot and nox emissions. *Sae technical paper series 940523*.

Peters, N. 1984. Laminar diffusion flamelet models in non-premixed turbulent combustion. *Progress in energy and combustion science*, **10**, 319–339.

Peters, N. 2000. *Turbulent combustion*. Cambridge University Press.

Piessens, R., deDoncker Kapenga, E., Uberhuber, C., & Kahaner, D. 1983. Quadpack: a subroutine package for automatic integration. *Series in computational mathematics*, **1**.

Pitsch, H., & Peters, N. 1998. A consistent flamelet formulation for non-premixed combustion considering differential diffusion effects. *Combustion and flame*, **114**.

Pitsch, H., Barths, H., & Peters, N. 1996. Three-diemnsional modeling of no, and soot formation in di-diesel engines using detailed chemistry vased on the interactive flamelet approach. *Sae technical paper series 960257*.

Pitsch, H., Chen, M., & Peters, N. 1998. Unsteady flamelet modeling of turbulent hydrogen-air diffusion flames. *Symposium (international) on combustion*, **1**, 1057 – 1064.

Poinsot, T., & Trouve, A. 1994. Using direct numerical simulation to understand turbulent combustion. *Proceedings of the 6th joint eps-aps international conference on physics computing*, 55 – 61.

Pope, S. B. 1985. Pdf methods for turbulent reactive flows. *Progress in energy and combustion science*, **11**(2), 119 – 192.

Pracht, W.E. 1975. Calculating three-dimensional fluid flows at all speeds with an eulerian-lagrangian computing mesh. *Journal of computational physics*, **17**(2), 132 – 59.

Press, William H., Teukolsky, Saul A., Vetterling, William T., & Flannery, Brian P. 2007. *Numerical recipes 3rd edition: The art of scientific computing*. Cambridge University Press.

Radhakrishnan, K., & Hindmarsh, A. C. 1993. Description and use of lsode, the livermore solver for ordinary differential equations. *Llnl report ucrl-id-113855*.

Reitz, R. D. 1978. *Atomization and other breakup regimes of a liquid jet*. Ph.D. thesis, Princeton University.

Reitz, R. D. 1987. Modeling atomization processes in high-pressure vaporizing sprays. *Atomization and spray technology*, **3**, 390–337.

Reveillon, J., & Vervisch, L. 2000. Spray vaporization in nonpremixed turbulent combustion modeling: a single droplet model. *Combustion and flame*, **121**(1-2), 75 – 90.

Riesmeier, E., Honnet, S., & Peters, N. 2004. Flamelet modeling of pollutant formation in a gas turbine combustion chamber using detailed chemistry for a kerosene model fuel. *Journal of engineering for gas turbines and power*, **126**(4), 899 – 905.

Spalding, D. Brian. 1976. Development of the eddy-break-up model of turbulent combustion. *Proceedings of the combustion institute*, 1657 – 1663.

Steisch, G. 2003. *Modeling engine spray and combustion processes*. Springer–Verlag.

Takeda, Y., & Keiichi, N. 1996. Emission characteristics of premixed lean diesel combustion with extremely early staged fuel injection. *Sae technical paper series 961163*.

Tanaka, S., Ayala, F., & Keck, J. C. 2003. A reduced chemical kinetic model for HCCI combustion of primary reference fuels in a rapid compression machine. *Combustion and flame*, **133**(4), 467 – 481.

Thring, R. H. 1989. Compression-ignited homogeneous charge combustion engines. *Sae technical paper series 892068*.

Venkatesh, G., & Abraham, J. 2002. A comparison of mixing-controlled and flamelet models for diesel combustion. *Sae technical paper series 2002-01-1116*.

Vogel, S., Hasse, C., Gronki, J., Andersson, S., andJ. Wolfrum, N. Peters, & Schulz, C. 2005. Numerical simulation and laser-based imaging of mixture formation, ignition, and soot formation in a diesel spray. *Proceedings of the combustion institute*, **30 II**, 2029 – 2036.

Weber, J., & Peters, N. 2006. Calibration of spray model constants for CFD-simulations of DI diesel engines using the representative interactive flamelet (RIF) model. *International journal of vehicle design*, **41**(1-4), 143 – 64.

Weber, J., Peters, N., Diwakar, R., Siewert, R. M., & Lippert, A. 2007. Simulation of the low-temperature combustion in a heavy-duty diesel engine. *Sae technical paper series 2007-01-0904*.

Wooldridge, M. S., Hong, S., Im, H. G., Assanis, D. N., & Pitsch, H. 2005. Development and application of a comprehensive soot model for 3D CFD reacting flow studies in a diesel engine. *Combustion and flame*, **143**(1-2), 11 – 26.

Zhao, H., Li, J., Ma, T., & Ladommatos, N. 2002. Performance and analysis of a 4-stroke multi-cylinder gasoline engine with CAI combustion. *Sae paper 2002-01-0420*.